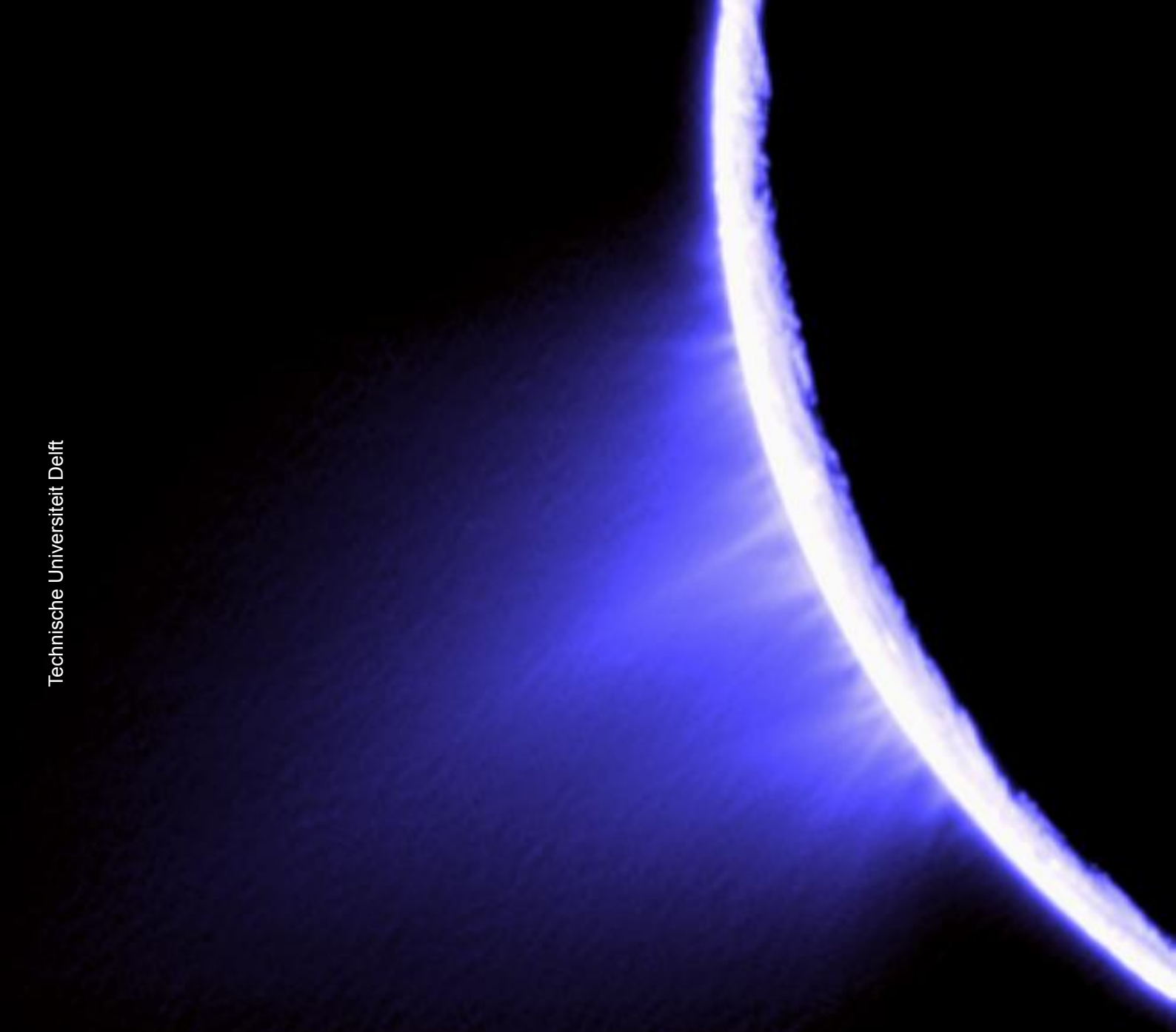

Technische Universiteit Delft

Linking Enceladus' plume characteristics to the crevasse properties

N.J. van der Hijden

TU Delft

Linking Enceladus' plume characteristics to the crevasse properties

by

N.J. van der Hijden

Student number: 4486102
Project duration: March 1, 2020 – December 20, 2020
Supervisors: F. F. J. Schrijer TU Delft
S. M. Cazaux TU Delft

Front cover image credits: NASA/JPL/Space Science Institute.
About the object: Processed image of the jets spurting ice particles and water vapor, taken by the Cassini spacecraft.

TU Delft

Preface

This report puts an end to my journey as a TU Delft student and to a year of hard work. It also allows me, to continue my journey as an Aerospace Engineer. I couldn't have fullfilled this journey without the continuous support of all those who are close to me. I would like to thank Stéphanie Cazaux and Ferry Schrijer, my thesis supervisors. They introduced me to the fascinating topic of the plumes of Enceladus and helped me learn and grow. Every week started with a meeting on Monday morning, which began with some small talk about the weekend but got very serious within minutes. That is what I appreciate most of our work, that is was always combined with fun. Thank you, for all the discussions and support. I also want to thank Tara Bründl and Stavros Sklavenitis, members of our so-called plume team. With their ongoing enthousiasm in the wind tunnel they managed to recreate the plume on small scale, which I then simulated using my numerical model. We worked together on a weekly basis and had very useful and interesting discussions on all plume related topics.
Also a special thanks to Aaron Bakx, Niels Bakx, Stan Spee, Jurrien Vos and Tommy Tran, with whom I have spend many sessions in either the library, Aerospace Faculty or the Fellowship. Thanks for the serious and less serious conversations about either our theses or about every day stuff. Thank you for listening to my rambles about how the plumes of Enceladus generates imaginary numbers.
I want to thank my family, for always supporting me during my thesis. Either by bringing coffee to my room, or just being there for mental support. Thanks to all my friends for making every day a better day. Without all of you, I couldn't have done it.

N.J. van der Hijden
Delft, December 2021

Nomenclature

Nu	Nusselt number
Pr	Prandlt number
Re	Reynolds number
1D	One - Dimensional
CDA	Cosmic Dust Analyser
CIRS	Cassini Infrared Spectrometer
ISS	Imaging Science Subsystem
UVIS	Ultraviolet Imaging Spectrograph
VIMS	Visible and Infrared Mapping Spectrometer
$\dot{m}$	Mass flow [kg/s]
$\dot{Q}$	Heat flow [J/s]
$\dot{q}$	Specific heat flow [J/kgs]
γ	Specific heat ratio [-]
γ_{nuc}	Nucleation rate [$1/m^3 s$]
λ	Mean free path [m]
μ	Viscosity [Ns/m^2]
ρ	Density [kg/m^3]
ρ	Density of the flow [kg/m^3]
σ	Cross-section of a water molecule m^2
τ	Stress [Pa]
A	Cross-section of the channel [m^2]
C	Courant number [-]
c	Circumference of the channel [m]
C_P	Specific heat capacity at constant pressure [$J/(kgK)$]
c_s	Local speed of sound [m/s]
C_V	Specific heat capacity at constant volume [J/(kg K)]
C_x	Viscosity constant [-]
c_{stick}	Sticking coefficient [-]
D	Diameter [m]
dR/dz	Particle growth rate [-]

E	Wall mass flow per unit area [kg/m^2s]
e	Specific internal energy [J]
F	Flux Vector [-]
f	Solid fraction [-]
g	Gravity acceleration [m/s^2]
H	Specific sublimation energy [-]
J	Source Term [-]
k	Thermal conductivity [W/mK]
k_B	Boltzmann constant [$1.380649 \cdot 10^{-23}\ J/K$]
L	Length [m]
L_h	Latent heat of condensation [$2.8 \cdot 10^6\ J/kg$]
M	Mach number [-]
m	Mass [kg]
m_0	Mass of a water molecule [kg]
m_{H_2O}	Molar mass of H_2O [kg/mol]
N_A	Number of Avogadro [$1/mol$]
p	Pressure [Pa]
Q	Discharge [kg/s]
R	Specific gas constant [-]
r	Radius [m]
S	Super-saturation [-]
S_w	Surface area of the walls
T	Temperature [K]
t	Time [s]
T_w	Wall temperature [K]
U	Solution Vector [-]
u	X-component of velocity [m/s]
V	Velocity [m/s]
x	Location [m]
z	Location along the longitudinal axis of the channel

Contents

1

Introduction and research questions

In 2005 the Cassini spacecraft discovered geyser emissions at the south polar region of Enceladus (Porco et al. [23]). These so-called plumes are generated from surface hot spots along parallel elongated crevasses, called the ”tiger stripes”. The Cassini mission was a major milestone in the understanding of the physics of the Saturn system and the icy satellite itself. The source of the plumes may be vaporization of liquid water followed by particle production (Schmidt et al. [26]) and/or vapor sublimation from the walls with subsequent condensation (Kieffer et al. [17]) where grains and vapor are accelerated to the surface by pressure-driven expansion (Matson et al. [19]) through crevasses that reach the surface. Cassini has observed the plumes for over a decade. These observations yielded crucial details of the plumes, such as their compositions, massflows, Mach numbers, emitted power and temperatures (Spencer et al. [28], Porco et al. [23], Kieffer et al. [18]).
The H_2O production, referred to as mass flow, has been thoroughly studied, but no tight constrains are determined to date. It has been determined that a mass flow of $\sim 300\ kg/s$ is required to maintain the observed density of the E-ring around Saturn (Jurac and Richardson [15]). From Ultraviolet Imaging Spectrograph (UVIS) stellar and solar occultation observations the mass flow is estimated in various studies. In Hansen et al. [8], Hansen et al. [9] and Hansen et al. [10] the mass flow is estimated ranging from $\sim 100 - 250\ kg/s$. From Ion and Neutral Mass Spectrometer (INMS) measurements and UVIS observations Burger et al. [4] estimates a mass flow of $300\ kg/s$. From INMS measurements of the $E3$, $E5$ and $E7$ flybys estimates of mass flow ranging from $500 - 1000\ kg/s$ and $200 - 750\ kg/s$ are obtained by Dong et al. [5] and Smith et al. [27], respectively.
These wide ranges of mass flow estimates indicate that the intensity of the jets varies over time, caused by tidally driven expansion and compression of the crevasses (Porco et al. [22]). Temporal variations can occur on time scales in the order of days, caused by Enceladus' orbital frequency (Saur et al. [25]). Whereas the orbital period is only 1.37 days (Ingersoll et al. [14]).
From the mass flow of the plume and the grain production rate, an estimate of the ice-vapor ratio can be generated. This ratio is crucial in characterising the crevasse. Ingersoll and Ewald [12] obtained an ice-vapor ratio of $\sim 0.35 - 0.7$ from the Imaging Science Subsystem (ISS) images. However, this estimate has been corrected for and redetermined at ~ 0.07, considering irregular aggregates formed from spherical monomers, instead of solid spherical particles (Gao et al. [6]). From the column densities of UVIS and Imaging Science Subsystem (ISS) data, and ice-vapor ratio of ~ 0.4 was determined (Porco et al. [23]). However, in a redetermination a lower ratio was found of ~ 0.2 (Kieffer et al. [18]), where a ratio of $0.1 - 0.2$ was suggested to be likely. This ratio is sensitive to the altitude at which is was measured, since some particles might have been doubly counted due to them falling back to the surface, or not counted at all since some particle do not reach the measurement height of $15\ km$.
The particle sizes in the E-ring range from $0.3 - 3\mu m$, however larger grains have longer lifetimes and are therefore more abundant (A. Howett [1]). From the Visible and Infrared Mapping Spectrometer (VIMS) observations, a particle size distribution of particles with radii of $1 - 3\mu m$ is obtained, with the highest number density obtained for $1\mu m$ (Hedman et al. [11]). Larger particle sizes show stronger decreases with altitude and are less likely to escape the gravity field of Enceladus. The larger particles fall back to the surface of Enceladus, with sizes reaching $50 - 75\ \mu m$ (Kempf et al. [16], Guzman et al. [7]).

This emitted ice-vapor mass flow is distributed around Saturn as neutral H_2O gas, plasma trapped in the magnetic field of Saturn and as ice grains in the E-ring. There are estimates of $15-25\%$ of the contribution of the jets to the total mass flow (Hansen et al. [10]). On the other hand it has been estimated that the individual jets along the Tiger Stripes are the dominant source of the total plumes source rate ($>99\%$)(Burger et al. [4]) ($68-77\%$)(Tenishev et al. [31]). Hot spots are detected in the region of these isolated sources, with temperatures that are significantly higher than the nominal surface temperature of Enceladus ($T_S = 70K$) (Spitale and Porco [29], Bland et al. [3]). Estimates for these temperatures, using Cassini Infrared Spectrometer (CIRS) observations, are $\sim 165\ K$ (Spencer et al. [28]). By using UVIS data the vent temperatures are estimated in the range of $\sim 170-210\ K$ (Tenishev et al. [31]). Even higher vent temperatures are determined by considering the walls being in equilibrium with the flow, where $T = 236\ K$ (Nakajima and Ingersoll [20]).
There are several hypothesis to explain what the source of the plumes is. Kieffer et al. [17] suggests that the plume originates from clathrate decomposition, to explain the abundances of volatile gases. Nimmo et al. [21] suggest that sublimation from heated water ice is the main source of the plumes. However, both scenario's can not explain the identification of a sodium rich grain population in the E-ring, of $\sim 0.5-2\%$ in mass (Postberg et al. [24]). This amount of salt can only arise if the plumes originate from liquid water, since the ice layers are deemed to be almost salt-free (Zolotov [35]). Schmidt et al. [26] argues that the gas densities corresponding to sublimation from ice at temperatures below $260\ K$ are too low to support the measured particle fluxes and that a reservoir near triple point is required to obtain the measured particle size and velocity distributions.
The outflow velocities have been investigated in many studies, the results have a wide spreading. Plume velocities of $300-500\ m/s$ are estimated to fit column densities measured by the UVIS (Tian et al. [33]). Higher velocities of $\sim 550-750\ m/s$ have been estimated to fit the INMS neutral H_2O densities of the plumes (Dong et al. [5], Smith et al. [27]). With a combination of UVIS and INMS observations, velocities in the range of $350-950\ m/s$ result in a best fit (Tenishev et al. [31]). Also mixtures of low and high velocity gas emissions have been detected of $>1000m/s$ ($M = 5-10$). However, such velocities tend to over-estimate the observed column densities and just a small fraction of the plume reaches these velocities ($\sim 12\%$), whereas the in-accuracy of this fraction is relatively large ($\pm 30\%$) (Teolis et al. [32]. The most consensus of plume velocity estimates is in the region of $350-950\ m/s$.
In this paper, we follow a similar approach as Schmidt et al. [26] to predict the characteristics of the plume as a function of the crevasse properties, focusing on nucleation and particle production. Also, the interactions with the walls, in terms of accretion, sublimation, convection and friction, are taken into account. The channels behaved as nozzles, where variations in channel width generate the transition to supersonic speeds. This transition occurs near the throat of the channel, where the condensation is locally enhanced. This introduces latent heat which heats up the flow, where the walls are constantly accreting and sublimating water vapor.
The aim of this paper is to determine the characteristics of the crevasses, using the data generated from Cassini observations. We perform a parameter study and consider various shaped channels to better understand how plumes differ from one channel to another. The plume features of interest are the reservoir conditions and the geometry of the crevasse.

1.1. Research questions

From the knowledge gaps presented in the introduction, a research question has been formulated:
How do we link plume characteristics to properties of the crevasse?

This results in four research questions:

1. Can different plume models reproduce the characteristics of the plumes observed by Cassini?
   (a) An isentropic model.
   (b) A multi-phase model.
   (c) A model that accounts for wall interactions.
2. How does the geometry of the crevasse change the plumes' characteristics?
   (a) Length.

   (b) Width.
   (c) Expansion ratio.
   (d) Irregularity.

3. How do wall interactions change the characteristics of the plume?
4. Do plume characteristics provide constrains on the crevasse geometry, ocean properties or other processes?

1.1.1. Report outline

The research and findings of this thesis have been documented in the form of a journal article, included in Chapter 2. The conclusions and recommendations for future work are provided in Chapter 3.

2

Journal article

The research work has been documented in the form of a scientific paper, to be submitted to the publisher Elsevier. The article is provided in this chapter, following the standard Elsevier template and guidelines.

Linking Enceladus' plume characteristics to the crevasse properties

Nick J. van der Hijden[a,*], Ferry F.J. Schrijer[a] and Stéphanie M. Cazaux[a]

[a]*Faculty of Aerospace Engineering, Delft University of Technology, Delft, The Netherlands*

ARTICLE INFO

Keywords:
Enceladus
Plumes
Crevasse
Reservoir conditions
Nucleation
Particle growth
Solid fraction
Particle size
Accretion
Sublimation

ABSTRACT

Supersonic plumes consistent of water vapor and ice particles have been observed by the Cassini spacecraft when flying over the tiger stripes of Enceladus at the south polar terrain of the satellite. Measurements of the salinity of the plumes ($\sim 0.5-2\%$) and the size of the emitted particles, indicate a subsurface liquid ocean beneath the crust of ice. The vent temperature of the plumes were measured to be relatively high ($170-210\ K$) compared to the cold surface temperature of Enceladus. The mass flow, velocity and particle size show a wide range of possible values, whereas the solid fraction is estimated between $7-20\ \%$. Here we demonstrate a fluid dynamics model that accounts for nucleation, particle growth, wall accretion and sublimation and the viscous interaction with the walls. The channels behave as converging-diverging nozzles, which form supersonic plumes due to a pressure difference between the reservoir and the exosphere. The geometry of the channel, the reservoir conditions and wall interactions are studied to reproduce the characteristics of the plumes observed by Cassini. From a parameter study performed on the crevasse properties we find that the velocity and the solid fraction increase with the expansion ratio, whereas the exit temperature is inversely related to the expansion ratio. The interactions with the walls reduce the mass flow in the channel and start condensation earlier in the channel, this increases the solid fraction, particle size and velocity and reduces the exit temperature. The particle size is dominantly dependent on the length of the channel, large particles ($\sim 75\mu m$) must originate from up to a kilometre below the surface, while smaller particles ($\sim 3\mu m$) can originate from $\sim 150\ m$ below the surface. The channel requires an expansion ratio close to $D_{throat}/D_{exit} = 4$, to generate the observed exit temperature $\leq 210\ K$ with velocities up to $950\ m/s$ and a solid fraction ranging from $0.07-0.2$. The minimum width of the channel needs to be in the order of meters to withhold the channel from freezing up within days and a liquid reservoir at a temperature near triple point is most probable to agree with the observed exit temperature and velocity.

1. Introduction

In 2005 the Cassini spacecraft discovered geyser emissions at the south polar region of Enceladus (Porco et al. [37]). These so-called plumes are generated from surface hot spots along parallel elongated crevasses, called the "tiger stripes". The Cassini mission was a major milestone in the understanding of the physics of the Saturn system and the icy satellite itself. The source of the plumes may be vaporization of liquid water followed by particle production (Schmidt et al. [40]) and/or vapor sublimation from the walls with subsequent condensation (Kieffer et al. [26]) where grains and vapor are accelerated to the surface by pressure-driven expansion (Matson et al. [30]) through crevasses that reach the surface. Cassini has observed the plumes for over a decade. These observations yielded crucial details of the plumes, such as their compositions, massflows, Mach numbers, emitted power and temperatures (Spencer et al. [46], Porco et al. [37], Kieffer et al. [27]).

The H_2O production, referred to as mass flow, has been thoroughly studied, but no tight constrains are determined to date. It has been determined that a mass flow of $\sim 300\ kg/s$ is required to maintain the observed density of the E-ring around Saturn (Jurac and Richardson [24]). From Ultraviolet Imaging Spectrograph (UVIS) stellar and solar occultation observations the mass flow is estimated in various studies. In Hansen et al. [17], Hansen et al. [15] and Hansen et al. [16] the mass flow is estimated ranging from $\sim 100-250\ kg/s$. From Ion and Neutral Mass Spectrometer (INMS) measurements and UVIS observations Burger et al. [6] estimates a mass flow of $300\ kg/s$. From INMS measurements of the $E3$, $E5$ and $E7$ flybys estimates of mass flow ranging from $500-1000\ kg/s$ and $200-750\ kg/s$ are obtained by Dong et al. [11] and Smith et al. [42], respectively.

These wide ranges of mass flow estimates indicate that the intensity of the jets varies over time, caused by tidally driven expansion and compression of the crevasses (Porco et al. [36]). Temporal variations can occur on time scales in the order of days, caused by Enceladus' orbital frequency (Saur et al. [39]). Whereas the orbital period is only 1.37 days (Ingersoll et al. [21]).

From the mass flow of the plume and the grain production rate, an estimate of the ice-vapor ratio can be generated. This ratio is crucial in characterising the crevasse. Ingersoll and Ewald [20] obtained an ice-vapor ratio of $\sim 0.35-0.7$ from the Imaging Science Subsystem (ISS) images. However, this estimate has been corrected for and redetermined at ~ 0.07, considering irregular aggregates formed from spherical monomers, instead of solid spherical particles (Gao et al. [12]). From the column densities of UVIS and Imaging Science Subsystem (ISS) data, and ice-vapor ratio of ~ 0.4 was determined (Porco et al. [37]). However, in a redetermination a lower ratio was found of ~ 0.2 (Kieffer et al. [27]), where a ratio of $0.1-0.2$ was suggested to be most likely. This ratio is sensitive to the altitude at which it was measured, since some particles might have been doubly counted

*Corresponding author
n.j.vanderhijden@student.tudelft.nl (N.J.v.d. Hijden)

due to them falling back to the surface, or not counted at all since some particle do not reach the measurement height of 15 km.
The particle sizes in the E-ring range from $0.3 - 3\mu m$, however larger grains have longer lifetimes and are therefore more abundant (A. Howett [1]). From the Visible and Infrared Mapping Spectrometer (VIMS) observations, a particle size distribution of particles with radii of $1 - 3\mu m$ is obtained, with the highest number density obtained for $1\mu m$ (Hedman et al. [19]). Larger particle sizes show stronger decreases with altitude and are less likely to escape the gravity field of Enceladus. The larger particles fall back to the surface of Enceladus, with sizes reaching $50 - 75\ \mu m$ (Kempf et al. [25], Guzman et al. [14]).
This emitted ice-vapor mass flow is distributed around Saturn as neutral H_2O gas, plasma trapped in the magnetic field of Saturn and as ice grains in the E-ring. There are estimates of $15 - 25\%$ of the contribution of the jets to the total mass flow (Hansen et al. [16]). On the other hand it has been estimated that the individual jets along the Tiger Stripes are the dominant source of the total plumes source rate ($> 99\%$)(Burger et al. [6]) ($68 - 77\%$)(Tenishev et al. [49]). Hot spots are detected in the region of these isolated sources, with temperatures that are significantly higher than the nominal surface temperature of Enceladus ($T_S = 70K$) (Spitale and Porco [48], Bland et al. [4]). Estimates for these temperatures, using Cassini Infrared Spectrometer (CIRS) observations, are $\sim 165\ K$ (Spencer et al. [46]). By using UVIS data the vent temperatures are estimated in the range of $\sim 170 - 210\ K$ (Tenishev et al. [49]). Even higher vent temperatures are determined by considering the walls being in equilibrium with the flow, where $T = 236\ K$ (Nakajima and Ingersoll [33]).
There are several hypothesis to explain what the source of the plumes is. Kieffer et al. [26] suggests that the plume originates from clathrate decomposition, to explain the abundances of volatile gases. Nimmo et al. [34] suggest that sublimation from heated water ice is the main source of the plumes. However, both scenario's can not explain the identification of a sodium rich grain population in the E-ring, of $\sim 0.5 - 2\%$ in mass (Postberg et al. [38]). This amount of salt can only arise if the plumes originate from liquid water, since the ice layers are deemed to be almost salt-free (Zolotov [58]). Schmidt et al. [40] argues that the gas densities corresponding to sublimation from ice at temperatures below $260\ K$ are too low to support the measured particle fluxes and that a reservoir near triple point is required to obtain the measured particle size and velocity distributions.
The outflow velocities have been investigated in many studies, the results have a wide spreading. Plume velocities of $300 - 500\ m/s$ are estimated to fit column densities measured by the UVIS (Tian et al. [51]). Higher velocities of $\sim 550-750\ m/s$ have been estimated to fit the INMS neutral H_2O densities of the plumes (Dong et al. [11], Smith et al. [42]). With a combination of UVIS and INMS observations, velocities in the range of $350 - 950\ m/s$ result in a best fit (Tenishev et al. [49]). Also mixtures of low and high velocity gas emissions have been detected of $> 1000m/s$ ($M = 5 - 10$). However, such velocities tend to over-estimate the observed column densities and just a small fraction of the plume reaches these velocities ($\sim 12\%$), whereas the inaccuracy of this fraction is relatively large ($\pm 30\%$) (Teolis et al. [50]. The most consensus of plume velocity estimates is in the region of $350 - 950\ m/s$.
In this paper, we follow a similar approach as Schmidt et al. [40] to predict the characteristics of the plume as a function of the crevasse properties, focusing on nucleation and particle production. Also, the interactions with the walls, in terms of accretion, sublimation, convection and friction, are taken into account. The channels behaved as nozzles, where variations in channel width generate the transition to supersonic speeds. This transition occurs near the throat of the channel, where the condensation is locally enhanced. This introduces latent heat which heats up the flow, where the walls are constantly accreting and sublimating water vapor.
The aim of this paper is to determine the characteristics of the crevasses, using the data generated from Cassini observations. We performed a parameter study and considered various shaped channels to better understand how plumes differ from one channel to another. The plume features of interest are the reservoir conditions and the geometry of the crevasse.
In Section 2 the method used to simulate the plumes is explained, the baseline channel with the different parameters used for the study is explained in Section 3 and in Section 4 the results for the different crevasses and reservoir conditions are shown, these results are discussed in Section 6 and a conclusion is drawn in Section 7.

2. Method

The fluid model is based on the conservation equations for mass, momentum and energy. The channel shape is given as input which generates the initial conditions at the inlet of the channel, in terms of temperature, pressure, density and velocity. The flow is computed along the whole channel and in each iteration the flow is updated using a predictor-corrector scheme in a time-marching fashion. This is done until a steady-state flow is reached and the convergence criteria are met. The model includes particle production from homogeneous nucleation, particle growth, sublimation from the walls and accretion on the walls. Therefore functions for these phenomena are present in the model that numerically determine the effect on the conservation equations. The conservation equations are used in the conservative form and are therefore suitable for shock-capturing (Anderson and Wendt [2]). So in the case that there is a shock present in the channel, the discontinuous shape of the flow parameters is computed accordingly.

2.1. Governing equations

The governing equations are derived from the continuity, momentum and energy equations in their conservative form, given in Sections 2.1.1 to 2.1.3.

2.1.1. Continuity

The continuity equation in its conservative differential form, suitable for quasi-one-dimensional flow, accounts for mass flow into the walls, generated due to sublimation and accretion. This is done by a sink or source term on the right-hand side of the equation, $\dot{m}_w$ $[kg/s]$. t is time $[s]$, z is the vertical distance measured from the reservoir $[m]$, ρ is the vapor density $[kg/m^3]$, V is the velocity $[m/s]$ and A is the cross-sectional area of the channel $[m^2]$.

$$\frac{d(\rho AV)}{dz} = -\frac{\dot{m}_w}{dz} \tag{1}$$

2.1.2. Momentum

The momentum equation in the z-direction, for viscous flow with no body forces, is given by Equation 2, where p denotes the pressure $[N/m^2]$, $\dot{m}_a$ is the mass rate of accretion into the walls $[kg/s]$ and S_w is the surface area of the walls. The second term on the right-hand side accounts for the loss of momentum due to the wall interactions and the third for friction with the walls, where τ is friction $(= 1/2 f \rho V^2)$ and f is the friction coefficient. This equation is written in conservation form for quasi-one-dimensional flow:

$$\frac{d\left(\rho V^2 A\right)}{dz} = -A\frac{\partial p}{dz} - \frac{\dot{m}_a V}{dz} - \frac{\tau S_w}{dz} \tag{2}$$

2.1.3. Energy

The energy equation in its conservative differential form, suitable for quasi-one-dimensional, that accounts for latent heat from condensation and evaporation in the flow and energy loss to the walls, is written in Equation 3. In this equation e is specific internal energy of the flow at temperature T and e_w is the specific energy of the vapor sublimation from the walls at the temperature of the walls T_w $[J/kg]$, e is written as $C_v T$ with $C_v = 1384.21\ J/(kgK)$ (Peeters et al. [35]), f is the solid fraction of the mass flow, L_h is the latent heat release for condensation of the gas $(2.8 \cdot 10^6 J/kg)$, $\dot{m}_a$ is the mass flow into the walls by accretion, $\dot{m}_s$ is the mass flow from the walls by sublimation, q is the convective heat coefficient, $p_{eq}^{s.g.}$ and $\rho_{eq}^{s.g.}$ are the saturated vapor pressure and density at the solid-gas equilibrium and S_w is the surface area of the walls.

$$\begin{aligned} \frac{d\left[\rho\left(e+\frac{V^2}{2}\right)AV + pAV\right]}{dz} &= \frac{d\left(\rho V f A\right)}{dz} L_h \\ -\frac{\dot{m}_a\left(e+\frac{V^2}{2}+\frac{p}{\rho}\right)}{dz} &+ \frac{\dot{m}_s\left(e_w + \frac{p_{eq}^{s.g.}}{\rho_{eq}^{s.g.}}\right)}{dz} - \frac{q(T-T_w)S}{dz} \end{aligned} \tag{3}$$

The first term in Eq. (3) is the net flow of energy across surface A and the second term is the work on the fluid by pressure force. The first term on the right-side is the addition of heat to the flow, in the form of latent heat, the second term is the loss of energy due to accretion onto the walls and the third term is energy gain by sublimation from the walls. When mass flow is accreting on the wall e, V, p and ρ are at the level of the flow, in the case of sublimation, $e = C_v T_w$, $V = 0$ and p and ρ are that of the saturated vapor at the solid-gas equilibrium at T_w (Nakajima and Ingersoll [33]). The fourth term accounts for the heat convection from or to the walls, where heat flows to the region at lower temperature.

In Eq. (4) $\dot{Q}$ is the heat flow $[J/s]$ and $\dot{q}$ is the specific heat flow $[J/kgs]$, this equation is used to derive the terms on the right-side of Equation 3. The first term is volumetric heating and the second term is the heat flux from conduction, obtained from gasdynamics relations (Zierep [57]). The latent heat that is released due to condensation of the ice depends on the net mass flux of ice, i.e. the difference between the mass fraction of ice entering and exiting the control volume. The ice generation within the system has a cross-sectional surface A contribution and the loss of energy due to wall interactions has a wall surface S_w contribution. Therefore Eq. (4) reduces to Eq. (5), where E is the mass flow into the walls per unit area $[kg/m^2 s]$.

$$\dot{Q} = \iiint_{\mathscr{V}} \rho c dV - \iint_S \bar{q} \cdot \bar{n} dS_w \tag{4}$$

$$\dot{Q} = \iint_A (\rho V f L_h \mathbf{V}) \cdot \mathbf{dA} - \iint_S E\left(e + \frac{V^2}{2} + \frac{p}{\rho}\right) d\mathbf{S_w} \tag{5}$$

These two terms are integrated and the limit it taken where x approaches zero, which results in the first and second term on the right-side of Equation 3, respectively.

2.2. MacCormack solver

The MacCormack method solves the flow that obeys the three conservation equations with a predictor-corrector scheme based on forward and rearward differences. A time-marching approach is used in which the flow variables are updated in each iteration (Anderson and Wendt [2]).

2.2.1. Generic form of conservation equations

The governing partial differential equations are written in a generic form. In these equations the dependent variables are the flux vectors $(p+\rho u, \rho(e+\frac{V^2}{2}, etc.)$, which lead to stable solutions. This system of equations is iteratively solved. The iterative procedure starts with an initial distribution for the flow state along z in the channel, this state is then updated in each iteration, according to the conservation equations. This is done with a time-marching approach to converge to a stable solution. For which Eq. (8) is used, where the first term presents the time derivative, the second term the spatial derivative and the J is a source term. The change in the solution vectors per iteration is computed with an average of the forward and rearward difference scheme (Anderson and Wendt [2]). From the conservation equations the entire system of governing equations is presented by Equation 6.

In this system U is the solution vector, F contains the flux terms and J is the source term.

$$\frac{\partial U}{\partial t} + \frac{\partial F}{\partial z} = J \tag{6}$$

In this system of equations, all the variables are made non-dimensional, indicated with a prime symbol. Resulting in the following elements of U, F and J.

$$\begin{aligned}
U_1 &= \rho' A' \\
U_2 &= \rho' A' V' \\
U_3 &= \rho' \left(\frac{e'}{\gamma - 1} + \frac{\gamma}{2} V'^2 \right) A' \\
F_1 &= \rho' A' V' \\
F_2 &= \rho' A' V'^2 + \frac{1}{\gamma} p' A' \\
F_3 &= \rho' \left(\frac{e'}{\gamma - 1} + \frac{\gamma}{2} V'^2 \right) V' A' + p' A' V' \\
J_1 &= -\frac{\dot{m}'_w}{dz'} \\
J_2 &= \frac{1}{\gamma} p' \frac{dA'}{\partial z'} - \frac{\dot{m}'_w V'}{dz'} - \frac{\tau' S}{dz} \\
J_3 &= \frac{d\left(\rho' V' f A'\right)}{dz'} \cdot L'_h - \frac{\dot{m}'_a \left(\frac{e'}{\gamma - 1} + \frac{\gamma}{2} V'^2 + \frac{p'}{\rho'} \right)}{dz'} \\
&\quad + \frac{\dot{m}'_s \left(\frac{e'_w}{\gamma - 1} + \frac{p_{eq}^{s.g.\prime}}{\rho_{eq}^{s.g.\prime}} \right)}{dz'} - \frac{q' \left(T' - T'_w \right) S'}{dz'}
\end{aligned} \tag{7}$$

With these elements, the conservation equations can be written as follows.

$$\frac{\partial U_n}{\partial t'} = -\frac{\partial F_n}{\partial z'} + J_n \tag{8}$$

2.3. Initial conditions

Initial conditions $T(z = 0)$ and $\rho(z = 0)$ are computed from the total conditions in the reservoir and the initial velocity $V(z = 0)$. This is done by using the energy equation, adiabatic equation of state and the ideal gas law.

$$p = \rho R T \tag{9}$$

The numerical procedure starts at $z = 0$, where $V \neq 0$, therefore the initial conditions are different than the total conditions in the reservoir. In literature the reservoir conditions are estimated at triple point ($T_{res} = 273.16\ K$, $\rho_{res} = 0.00485 kg/m^3$, $p_{res} = 611.2\ Pa$) (Porco et al. [37],Schmidt et al. [40]).

2.4. Phase change

The vapor that is generated in the reservoir flows into the channel, near the throat of the channel the conditions become such that a phase change can occur, i.e. water vapor condensates into ice. This enhanced condensation is caused by a strong temperature gradient, which causes super-saturation to increase. As a result nucleation is enhanced and a phase change is instigated. When a particle is larger than the critical radius r^*, it will continue to grow and contribute to the solid fraction of the mass flow. This entire process is explained in Sections 2.4.1 to 2.4.3.

2.4.1. Nucleation

In this model we use a temperature corrected empirical function for the homogeneous nucleation rates γ_{nuc} of D_2O and H_2O (Wölk et al. [56]). The empirical relation is extensively tested with nucleation data (Wölk and Strey [55],Viisanen et al. [53]). The study of Schmidt et al. [40] used the data that was available prior to this study, namely the study of Viisanen et al. [53]. However, in their erratum, it is mentioned that the calibration of the pressure had to be corrected for. This has been corrected for in the study of Wölk and Strey [55]. This served as a foundation for the empirical nucleation function, which is more accurate and valid for an extended temperature range. The empirical nucleation function for H_2O is valid for the range of nucleation rates $1 < \gamma_{nuc}/cm^{-3}s^{-1} < 10^{20}$, temperatures between $200 < K < 310$ and super-saturation levels between $5 < S < 200$.
This empirical function is based on from the classical nucleation theory. The Becker-Döring nucleation rate $\gamma_{nuc,BD}$ is given by Eq. (10)(Wölk et al. [56]).

$$\gamma_{nuc,\mathrm{BD}} = \sqrt{\frac{2\sigma}{\pi m}} v_m \left(\frac{p_v}{kT} \right)^2 e^{\left(\frac{-16\pi v_m^2 \sigma^3}{3(kT)^3 (\ln S)^2} \right)} \tag{10}$$

In Eq. (10), p_e and p_v are the equilibrium and the actual vapor pressures, $S = p_v/p_e$ is the supersaturation, T is the temperature, k is the Boltzmann constant and m, v_m and σ are the mass of the water molecule, the molecular volume and the surface tension of the critical cluster, respectively. In Eq. (11) the correction factor is stated, which makes the function more accurate for the described range of nucleation, temperature and super-saturation (Wölk and Strey [55]). The fit of the empirical function to nucleation data is given in Appendix A.2.

$$\gamma_{nuc,\mathrm{H_2O}} = J_{\mathrm{BD}} \exp\left(-27.56 + \frac{6.5 \times 10^3}{T} \right) \tag{11}$$

The nucleation rate γ_{nuc} equation is dominantly dependent on the super-saturation level S of the flow and the temperature T. S is calculated with Eq. (12), where $\rho_{\mathrm{eq}}^{(l.g.)}$ is the saturated vapor density for the liquid-gas equillibirum, at T_{gas}. $\rho_{\mathrm{eq}}^{(l.g.)}$ is used since the nuclei at these conditions only contain 20-30 water molecules, which is too small to be treated as crystalline (Schmidt et al. [40]).

$$S = \frac{\rho_{\mathrm{gas}}}{\rho_{\mathrm{eq}}^{(l.g.)} \left(T_{\mathrm{gas}} \right)} \tag{12}$$

$\rho_{\mathrm{eq}}^{(l.g.)}$ is determined by an empirical relation for pressure and the ideal gas law (Eq. (9), Eq. (13)). Therefore, $\rho_{\mathrm{eq}}^{(l.g.)}$ decreases rapidly with temperature, resulting in high levels of

super-saturation when density doesn't decrease proportionally (Peeters et al. [35]).

$$p_{\mathrm{eq}}^{(\mathrm{l.g.})}\left(T_{\mathrm{gas}}\right) = 610.8 \exp\left[-5.1421 \ln\left(T_{\mathrm{gas}}/273.15\right)\right. \\ \left. -6828.77\left(1/T_{\mathrm{gas}} - 1/273.15\right)\right. \tag{13}$$

With a high super-saturation level there is an large amount of collisions in the flow with many vapor particle hot spots as a result. This as a result generates the production of particles and instigates a phase change.

2.4.2. Particle growth

Nucleation is the first step in a phase transition, which forms particles that are larger than the critical radius r^* (Wölk and Strey [55]). Subsequently, the particles start to grow. The growth is caused by interaction with the surrounding gas; i.e. the water molecules hit the grains' surface and adsorb on it.

The growth rate of the grains is computed with Eq. (14), based on the calculation of the collision rate of water molecules with icy grains (Schmidt et al. [40]). In this equation β is the condensation coefficient, which gives the fraction of adsorbed molecules, of those which hit the grain, $c_s(z)$ is the local speed of sound and u_{gas} is the velocity of the gas $[m/s]$. β is set at 0.2 by comparison of numerically modelling and observations of Cassini (Schmidt et al. [40]). The term between square brackets accounts for the evaporation of molecules from the surface of the grains, which decreases the radius of the grains. This happens when the density of the vapor ρ_{gas} is smaller than that of the saturated vapor $\rho_{eq}^{(s.g.)}$ at temperature T_{gas}. Here it is assumed that the grains have the same temperature as the gas. In this equation the grains are treated as crystalline, since they are formed above 160 K (McLennan et al. [31].

$$\frac{dR}{dz} = \frac{\beta}{\sqrt{2\pi\gamma}\rho_{\mathrm{grain}}}\left[\rho_{\mathrm{gas}}(z) - \rho_{\mathrm{eq}}^{(s.g.)}\left(T_{\mathrm{gas}}(z)\right)\right]\frac{c_{\mathrm{s}}(z)}{u_{\mathrm{gas}}(z)} \tag{14}$$

The growth rate depends on the difference between ρ_{gas} and $\rho_{eq}^{(s.g.)}$, the grains stop growing when ρ_{gas} equals $\rho_{eq}^{(s.g.)}$. Both densities are relate to the expansion rate, since a fast expansion generally results in low temperatures. As a result of the low temperature $\rho_{eq}^{(s.g.)}$ decreases according to Eq. (15) and the ideal gas law (Schmidt et al. [40]).

$$p_{\mathrm{eq}}^{(s.g.)}\left(T_{\mathrm{gas}}\right) = e^{\left[\left(-2663.5/T_{\mathrm{gas}}+12.537\right)\ln(10)\right]} \tag{15}$$

Also ρ_{gas} decreases due to expansion, but slower than $\rho_{eq}^{(s.g.)}$. Hence the expansion rate and growth rate of grains are positively correlated.

2.4.3. Solid fraction

$f(z)$ is the solid fraction of the flow. Defined as the mass flow of icy grains divided by the total mass flow. Eq. (16) represents the derivative of the solid fraction $\left(\frac{df}{dz}\right)$ (Schmidt et al. [40]). In this equation ρ_{grain} is the density of the icy grains, set at 920 kg/m^3, Q is the total mass flow, γ_{nuc} is the nucleation rate, R is the maximal radius of the particles, R' is the growth rate of the particles, A is the channel area and Θ_H represents the Heaviside function.

$$f'(z) = \frac{4\pi\rho_{\mathrm{grain}}}{Q}\int_0^z \gamma_{\mathrm{nuc}}\left(z_0\right)\left[R(z) - R\left(z_0\right)\right]^2 \\ R'(z)A\left(z_0\right)\Theta_H\left(R(z) - R\left(z_0\right)\right)dz_0 \tag{16}$$

This equation is used to determine the solid fraction along the whole channel.

2.4.4. Particle size distribution

Nucleation occurs when temperature drops and supersaturation increases, in most cases this is near the channel throat, but this could also be somewhere else in the channel. The region in the channel where nucleation is maximum, is where the majority of the particles are generated. From here the particles grow along the channel accordingly to their growth rate. Therefore, in this zone, the particle size distribution at the outlet is set and doesn't change significantly.

In Equation 17 the subscript "∞" indicates quantities at the outlet of the channel. The size of a particle r at the outlet of the channel, that nucleated at location z_0 in the channel, is found with the integration along z of Equation 14.

$$r\left(z_0\right) = R_\infty - R\left(z_0\right) \tag{17}$$

From the conservation law, Equation 18, the concentration of such particles at the location of their origin $n(z_0)$ is determined. This concentration depends significantly on the amount of particles nucleated in a partial volume of the channel. The left-hand side of Equation 18 gives the amount of particles nucleated in an infinitesimal volume $A(z_0)dz_0$ over an infinitesimal time interval dt. The right-hand side shows the same amount that is removed from this volume by the steady-state gas flow.

$$\gamma_{\mathrm{nuc}}\left(z_0\right)S\left(z_0\right)dz_0dt = n\left(z_0\right)u_{\mathrm{gas}}\left(z_0\right)A\left(z_0\right)dt \tag{18}$$

Equation 19 shows that the concentration of these particles at the outlet, $n(\infty, z_0)$, obeys the continuity equation. The equation relates the amount of particles nucleated at z_0 that are present at the exit $n(\infty, z_0)$ to the concentration of particles nucleated at z_0 $n(z_0)$. In this equation A_∞ is the cross-section near the outlet.

$$n\left(\infty, z_0\right)u_\infty A_\infty = n\left(z_0\right)u_{\mathrm{gas}}\left(z_0\right)A\left(z_0\right) \tag{19}$$

Knowing that $n(\infty, z_0)$ gives the concentration of particles of size $r(z_0)$, combining Equation 18 and Equation 19 and writing the equations as a function of r, by realizing that $z_0(r)$ is the inverse of $r(z_0)$, the size distribution is obtained:

$$P(r)dr = \frac{\gamma_{\mathrm{nuc}}\left(z_0(r)\right)}{u_\infty}\left|\frac{dr}{dz_0}\right|^{-1}\frac{A\left(z_0\right)}{A_\infty}dr \tag{20}$$

2.5. Wall interactions

In this section the interactions with the icy walls are explained, consistent of accretion, sublimation, convection and friction. These are explained in Section 2.5.1, Section 2.5.2, Section 2.5.3 and Section 2.5.4, respectively.

2.5.1. Accretion

Accretion on the walls of the vapor reduces the energy of the flow, since it carries internal and kinetic energy. There is latent heat production when accretion occurs, but this latent heat has a relatively small effect and is assumed to be conducted through the ice (Nakajima and Ingersoll [33]). Accretion is dominant in the more narrow sections of the walls, where the mean free path of the vapor becomes larger relative to the channel diameter.

In the channel the vapor travels at velocity V. Simultaneously, the vapor has a thermal velocity V_{th}, computed with Eq. (21), where k_B is the Boltzmann constant and m is the mass of a H_2O molecule ($2.992 * 10^{-26}\ kg$, Shevkunov [41]). V_{th} is approximately 560 m/s in the $200 - 273\ K$ range and therefore larger than V in the major part of the channel.

$$V_{th} = \sqrt{\frac{8k_BT}{m\pi}} \tag{21}$$

This velocity is random in direction and causes the vapor particles to collide with the walls and with each other. The equation for the mean free path of the vapor is stated in Equation 22, where λ is the mean free path $[m]$, Δt is the time between collisions $[t]$, z is the collision frequency $[s^{-1}]$, k is the Boltzmann constant ($= 1.4806 \cdot 10^{-23} kgm^2/s^2K$), T is temperature $[K]$, σ is the cross-sectional area of a water molecule ($= (3A)^2 = 9 \cdot 10^{-20} m^2$) and p the pressure $[pa]$ (Atkins and de Paula [3]).

$$\lambda = V_{th}\Delta t = V_{th}/z = kT/\sigma \tag{22}$$

From this equation, Δt is derived to be:

$$\Delta t = kT/\sigma V_{th} p \tag{23}$$

The particles can only hit the walls when they are within a distance λ from the walls, since after a collision the velocity is again random and assumed to be straight within Δt. Due to this high thermal velocity the flow is assumed to redistribute after every Δt. The next Δt the vapor again travels a distance λ in a random direction. The possible locations of the particles after Δt can be visualized as the sphere in Fig. 1 with radius λ, being any location on the edge of the sphere. The chance of colliding with the wall decreases as d increases, where d is the distance to the wall.

From this, the probability of a particle hitting the wall within a distance λ, p_λ, can be computed. At a distance further than λ this probability is 0 and at a distance of close to zero from the wall the probability is 0.5. The probability within this distance is computed according to the ratio of the volume of the cap of the sphere that resembles the wall

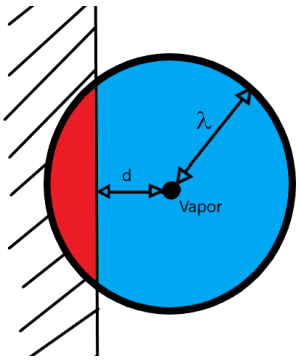

Figure 1: d is the distance to the wall, λ is the mean free path of the vapor and the black dot represents the location of the vapor at time t. When the vapor is at the indicated location at time t, then it can be anywhere at the black circle at $t + \Delta t$. If the vapor reaches a location on the black circle that encloses the red area, then it has hit the wall. This is only possible when the vapor molecule is within a distance λ from the wall and the chance of hitting the wall decreases with increasing d.

to the total volume of the sphere. h is the cap height, i.e. distance into the wall, $h = \lambda - d$, where d is the distance of the particle from the wall. h can be expressed in terms of λ, therefore the expression is independent of λ.

$$p_\lambda = \frac{V_{wall}}{V_{sphere}} = \frac{\pi h^2(\lambda - \frac{h}{3})}{\frac{4}{3}\pi\lambda^3} \tag{24}$$

The probability of a particle hitting the wall versus the distance to the wall is illustrated in Figure 2, where the average probability $p_{\lambda,a} \approx 0.19$. At a distance further than λ from the wall, the probability of vapor hitting the wall is zero.

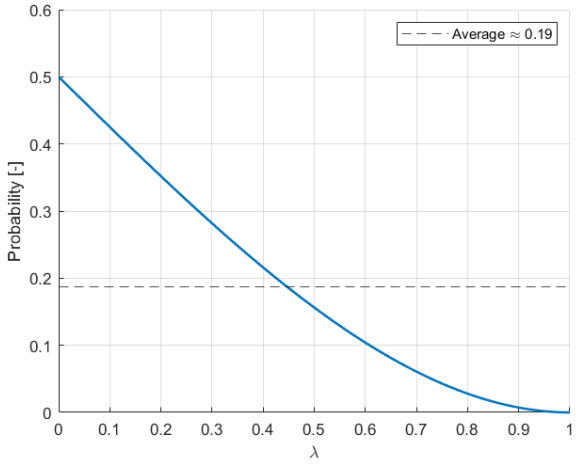

Figure 2: Probability that a vapor particle hits the wall. Close to the wall the probability approaches 0.5 and at a distance $> \lambda$ the probability is zero.

The average probability over the whole diameter of the channel is then determined with Equation 25, where $p_{channel}$ is the average probability of a particle hitting the wall from

anywhere in the channel [-], D is the diameter of the channel and r is the radius of the channel.

$$p_{channel} = p_\lambda \frac{2\lambda}{D} = p_\lambda \frac{\lambda}{r} \tag{25}$$

$p_{channel}$ must be multiplied with the sticking coefficient c_{stick} to determine the probability of a vapor particle actually sticking to the wall, this is called x.

$$x = p_{channel} \cdot c_{stick} = p_\lambda \frac{\lambda c_{stick}}{r} \tag{26}$$

x is then multiplied with total mass flow, resulting in the mass flux into the wall in one time step of Δt, i.e. the time in between collisions. The time that the flow is in one computational cell is:

$$t = \frac{dx}{V} \tag{27}$$

To determine the mass flow into the walls $\dot{m}_a$, this process is repeated $\frac{t}{\Delta t}$ times. The mass flow after Δt is then reduced to $(1-x) \cdot \dot{m}_{flow}$. Repeating this process results in:

$$\dot{m}_a = \sum_{i=1}^{n} x(1-x)^{n-1} \cdot \dot{m}_{flow} \tag{28}$$

Concluding from Eq. (23), Eq. (27) and Eq. (26), it is observed that accretion increases with V_{th}, ρ and c_{stick} and that it decreases with r and V. Therefore, narrow long channels will tend to freeze up faster.
The sticking coefficient of vapor on amorphous ice in the region of $220 - 273$ K varies from $0.02 - 0.4$ (Cuppen et al. [10], Veeraghattam et al. [52], Buch and Zhang [5]). As a baseline the method of Buch and Zhang [5] is used, which is given by Eq. (29).

$$c_{stick} = \left[\left(\frac{T}{102}\right) + 1\right]^{-2} \tag{29}$$

2.5.2. Sublimation

Sublimation of vapor from the walls is expected to increase the mass flow, indirectly affecting the momentum and energy of the flow. There is the cooling effect of evaporation, but this is assumed not to affect the flow, since the magnitude is small compared to the flow energy.
Sublimation is dominantly dependent on the wall temperature (Cuppen et al. [10],Smith et al. [43]). Equation 30 describes the rate of evaporation r $[s^{-1}]$, where υ is the prefactor $[s^{-1}]$, E is the binding energy $[K]$ and T is the temperature $[K]$. From Hasegawa and Herbst we know that $\upsilon = 2.29 \cdot 10^{12}$ s^{-1} and $E = 5600$ K (M. Minissale [29].

$$r = \upsilon e^{\left(-\frac{E}{T}\right)} \tag{30}$$

The area occupied by one molecule H_2O is $(3\text{Å})^2$, therefore the number of molecules per square meter is:

$$n = \frac{1}{(3\text{Å})^2} \tag{31}$$

The rate of molecules evaporating per squared meter is R $[kg/m^2 s]$:

$$R = r \cdot n \tag{32}$$

This number is translated to the mass flow of sublimation $\dot{m}_s$ $[kg/s]$ by using of the wall surface area S_w, the number of Avogadro N_A $(= 6.022 \cdot 10^{23}\ mol^{-1})$ and the molar mass of H_2O, m_{H_2O} $(= 0.018\ gmol^{-1})$, resulting in:

$$\dot{m}_s = R S_w \frac{m_{H2O}}{N_A} \tag{33}$$

The wall temperature gradient is set at 273 K near the reservoir and 200 K near the vent as a baseline (Nakajima and Ingersoll [33], Tenishev et al. [49]). For this reason the sublimation is expected to be dominant in the lower regions of the channel.

2.5.3. Convection

The convective heat transfer with the walls is computed with Eq. (35), where q is the convective heat coefficient . q is determined from a simple power law formula, Eq. (34), dependent on the Nusselt Nu, Reynolds Re and Prandlt Pr number, valid for $Re > 10.000$, where $Re = \rho V L/\mu$, $Nu = qL/k$ and $Pr = C_p \mu/k$, with L being the diameter of the channel, C_p is the specific heat capacity at constant pressure $(C_p = 1850\ J/(kgK)$, μ is the viscosity of water vapor $(= 0.925 \cdot 10^{-5}(T/300)^{1.1}\ kg/ms)$ and k is the thermal conductivity $(= 3\ W/mK)$ (Mills [32], Crifo [9], Peeters et al. [35]).

$$Nu = 0.023 Re^{0.8} Pr^{0.4} \tag{34}$$

Eq. (34) q is determined, which is then used to compute the heat convection in Eq. (35).

$$Q = q \cdot (T - T_w) \cdot S_w \tag{35}$$

Convection causes the flow to transfer heat with the walls, heat flows to the region with the lowest temperature.

2.5.4. Friction

The change in momentum Δp due to friction is computed with Eq. (36), where τ is the stress from the walls and S is the surface of the walls.

$$\Delta p = \tau V S_w \tag{36}$$

In this equation τ is written as Eq. (37). Where f is the friction factor, computed with the relation in Eq. (38) (Mills [32]). Friction accounts for the fact that the velocity near the walls approaches zero, which generates a turbulent flow. Friction generates a dragging effect on the flow and hereby reduces its momentum.

$$\tau = 1/2 f \rho V^2 \tag{37}$$

$$f = (0.790 \ln(Re) - 1.64)^{-2}; \quad 10^4 < Re < 5{\times}10^6 \tag{38}$$

2.6. Channel construction

To construct the channels used in this study, we define the D_{min}/D_{max} ratio, exit diameter D_{min}, channel length L and the correlation length L_0. By superposition of sine curves we find the width of the channel (Schmidt et al. [40]):

$$D(z) = \sum_i A_i \sin\left(k_i z + 2\pi\xi\right) \tag{39}$$

Where ξ is a uniformly distributed random number between $0-1$, A_i are the amplitudes of the modes (Schmidt et al. [40]):

$$A_i = \frac{a}{\sqrt{1+\left(k_i L_0\right)^2}} \tag{40}$$

And the wave numbers k_i are computed by (Schmidt et al. [40]):

$$k_i = \frac{1}{2}\left(\frac{2\pi}{L}\right) i < k_c = \left(\frac{2\pi}{L_0}\right) \tag{41}$$

The subscript i runs from 1 to n while $k_i < k_c$. With the chosen parameters we find a fitting crevasse, the examples are shown in Section 4.

3. Baseline Channel

The baseline channel is generated from the constraints found in the studies of Schmidt et al. [40], Ingersoll and Nakajima [22], Lucchetti et al. [28] and Nimmo et al. [34]. The channel shape is constructed from the superposition of random harmonics, explained in Section 2.6. The baseline channel functions as base for the parameter study, which is performed in Section 4.

3.1. Length

The estimated crustal thickness of Enceladus ranges from 70 km thick to a minimum of 1.5 km thick(Nimmo et al. [34],Lucchetti et al. [28],Čadek et al. [7]). These regions of minimum thickness are of interest, located at the South Polar Terrain (SPT) of Enceladus, since this is where the plumes are located. It is estimated that approximately 90% of the cracks is filled up with water due to the difference in densities of water and ice (Nakajima and Ingersoll [33]). Therefore, the channel length baseline is set at 150 m, based on estimates for the crustal thickness and numerical computations(Schmidt et al. [40]).

3.2. Crevasse exit width

The venting area is assumed to be of an rectangular shape and to run along the Tiger Stripes. From observations and numerical results, the exit width is estimated to be between $0.1-9$ m (Schmidt et al. [40],Goguen et al. [13]). The exit width is set at 9 m for the baseline channel.

3.3. Correlation length

The correlation length of the channel indicates the irregularity, i.e. the changes in the channel diameter. With a channel length of 150 m, the smallest scale length L_0 is set at 60 m for the baseline channel and $L_0 = 15$ m for the irregular channel. This results in Fig. 3 and Fig. 19, respectively. In Section 4.2.6 the effect of the correlation length is studied, to find the effect it has on the flow.

Table 1
Baseline channel properties

L	D_{exit}	D_{throat}	L_0	z^*	Reservoir	Model
150 m	9 m	6.3 m	60 m	111 m	Triple point	Multi-phase

3.4. Expansion rate

The expansion rate depends on the ratio between the exit and throat diameter of the channel $\frac{D_{exit}}{D_{throat}}$. From the study of Schmidt et al. [40] it is determined that a valid range is $1 < \frac{D_{exit}}{D_{throat}} < 3$, this interval shows good correlation with the Cassini High Rate Detector (HRD) data. For the baseline channel $\frac{D_{exit}}{D_{throat}}$ is set at 1.4 and is altered in Section 4.2.2 and Section 4.2.3.

3.5. Throat location

It is expected that the channel has a relatively wide reservoir and a relatively narrow exit (Postberg et al. [38]). Therefore, the throat location is set at $z = 111$ m in the baseline channel, resulting in a reservoir diameter of 12.5 m and an exit diameter of 9 m.

3.6. Overview

In Table 1 the properties of the baseline channel are repeated. Where L is the channel length, L_0 is the smallest scale length, z^* is the throat location, reservoir and model indicate the reservoir conditions and the model that the flow is computed with, respectively. The geometry of the channel is illustrated in Fig. 3.

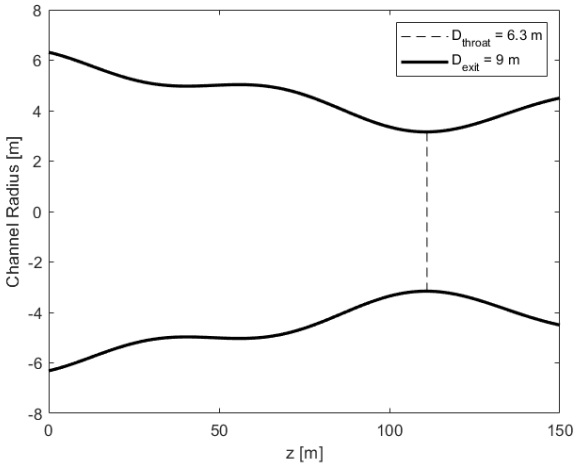

Figure 3: Baseline channel with a D_{min}/D_{exit} ratio of 1.4, the dashed line represents the location of the throat.

Table 2

Parameter study		
n	Test case	Changes compared to baseline, $n = 2$
1	Isentropic	Computed with isentropic model
2	multi-phase	-
3	Throat	Throat location moved upstream
4	$\uparrow D_{exit}/D_{throat}$	Smaller throat diameter
5	$\downarrow D_{exit}/D_{throat}$	Larger throat diameter
6	Width	Channel diameter halved ($D \rightarrow 1/2D$)
7	Length	Channel length doubled ($L \rightarrow 2L$)
8	Irregularity	Irregular channel geometry
9	Reservoir conditions	Reservoir pressure +200 Pa
10	Reservoir conditions	Channel temperature +10 K
11	Wall interactions	Computed with wall interactions model

4. Results

In this section the results of the different channel geometries and settings are presented. In Section 3 the baseline channel is illustrated and all the channel parameters are detailed. First, the analytical results determined by the isentropic model are presented in subsection 4.1. According to these results, and the range in temperature and pressure reached in the flow, the need of a phase change in the model becomes evident. The results of the multi-phase model are shown in subsection 4.2. In subsection 4.3 wall interactions are included in the model.
A parameter study is performed on each of the variable parameters to determine what the dependencies are. The different test cases are presented in Table 2, where n is the number of the case and the second column presents the parameter which is changed with respect to the baseline (Fig. 3).

4.1. Case 1: Isentropic model

The isentropic model yields results for a flow based on a pressure difference between inlet and outlet, generated from a reservoir at triple point conditions, the channel is described in Fig. 3.

In Fig. 4 (a), (b), (c) and (d) the solid lines represent the Mach number M, temperature T, density ρ and super-saturation S of the isentropic model, respectively. The flow reaches $M = 1$ at the throat, which position is highlighted by a dashed line, and expands further to $M = 1.76$ at the exit. As the velocity increases along the z-axis, the temperature of the flow decreases, i.e. internal energy ($C_v T$) is converted to kinetic energy ($1/2V^2$). The pressure decreases isentropically, to match the back pressure, as a result the density of the gas also decreases. The expanding gas, starting at 270 K near the reservoir, reaches a vent temperature of $T = 180$ K. At these low temperatures the super-saturation becomes unrealistically large. A phase change is very likely for such a high super-saturation level (Section 2.4.1). For this reason the possibility of a phase change with particle production and growth is added to the model and presented in Section 4.2.

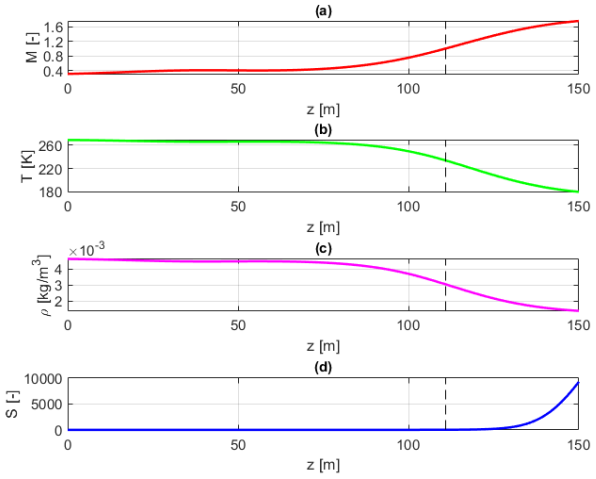

Figure 4: M, T, ρ and S profiles of the plume, the dashed line represent the location of the throat.

4.2. Case 2: Baseline, the multi-phase model

The multi phase model contains nucleation, particle growth and the corresponding solid fraction, reported in Section 2.4.1, Section 2.4.2 and Section 2.4.3, respectively. The flow is computed for the baseline channel illustrated in Figure 3, starting from triple point conditions in the reservoir. The results generated for the baseline channel with the multi-phase model are referred to as the baseline.

In Fig. 5 the solid lines represent the Mach number M, temperature T, density ρ and super-saturation S of the baseline and the dashed lines those of the isentropic model. The flow is very similar to that of the isentropic model up till the throat. At this location the super-saturation level S increases, due to a decrease in temperature T. Near the throat, T increases as a result of the phase change, which is explained with the results displayed in Fig. 6.

In Fig. 6 the solid lines represent the nucleation rate γ_{nuc}, solid fraction f, growth rate dR/dz and difference between flow density and equilibrium density $\rho - \rho_{eq}$ of the baseline and the dashed lines those of the isentropic model. As a result of the increase in S, the nucleation rate γ_{nuc} increases and icy particles are formed. Due to nucleation and particle growth, the solid fraction f increases (Fig. 6 (b)). The growth rate dR/dz is proportional to the difference between the gas density ρ and the equilibrium density ρ_{eq}, presented in Fig. 6 (d). Therefore, the growth rate dR/dz is positive and the particles start to grow. dR/dz is largest near the throat, and rapidly decreases due to the increase in T, since this increases ρ_{eq}. This increase of T is caused by a release latent heat generated from the growing solid fraction f. This increases both the internal and kinetic energy of the flow. The increase in internal energy translates to an increase in T and then according to Eq. (9), also an increase in ρ. In the channel there is a constant rate of mass flow, according to

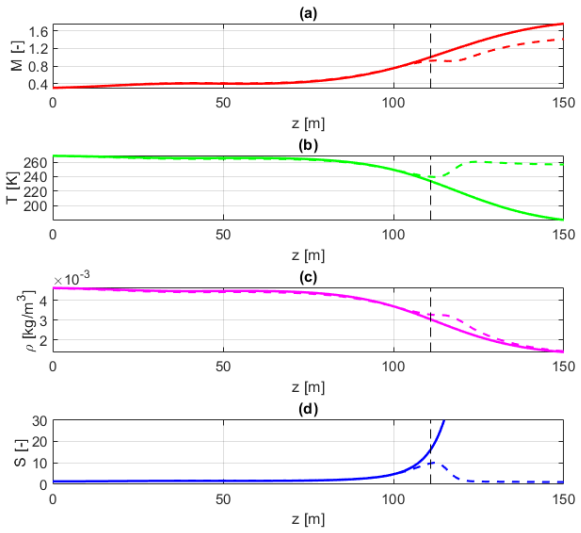

Figure 5: M, T, ρ and S profiles of the baseline channel computed with the multi-phase model (solid lines) and the isentropic model (dashed lines), the vertical dashed line represent the throat of the channel.

the conservation of mass and the principle of choked flow. The flow velocity V is dependent on both the cross-section of the channel A and the density of the flow ρ, according to Eq. (42).

$$\dot{m}_{flow} = \rho A V \tag{42}$$

Therefore, an increase of ρ causes the flow to slow down, since mass flow is constant. Due to the local increase in density near the throat, the Mach number in the throat is slightly lower than 1 (Fig. 5 (a)). After the throat the flow reaches supersonic speeds by the increase of kinetic energy, generated from the release of latent heat. Therefore the transition to sonic speed is not at the throat, but slightly downstream. The main difference between the two cases is that with nucleation, particle growth and the solid fraction, illustrated in Fig. 6 (a), (b) and (c), the temperature increases near the throat as a result of the generated latent heat. After the throat the temperature is close to being constant. The particles generated in the channel grow until they reach the vent, since dR/dz is positive along the entire length of the channel. The particle growth results in particles with a mean particle size of $R = 2.8\ \mu m$ and the solid fraction reaches 4.1% at the end of the channel (Fig. 31 and Fig. 6 (b)).

4.2.1. Case 3: Throat location

In this section the throat location is moved upstream to $z = 71\ m$ to determine the effect on the solid fraction, particle size distribution and flow parameters. The D_{exit}/D_{throat} ratio and the reservoir and exit diameter have not been changed, the channel is presented in Fig. 7.

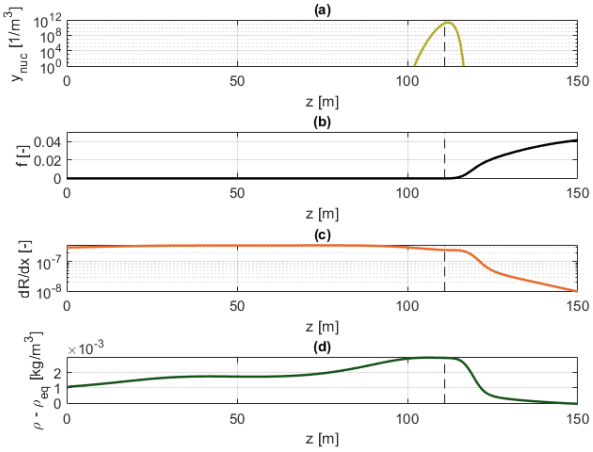

Figure 6: γ_{nuc}, f, dR/dz and $\rho - \rho_{eq}$ profiles of the baseline channel, computed with the multi phase model. The dashed line represents the location of the throat.

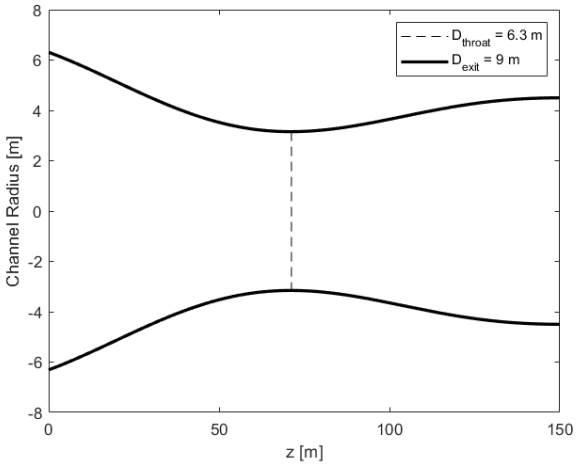

Figure 7: Channel with a D_{exit}/D_{throat} ratio of 1.4 and the throat located at $z = 71\ m$, indicated by the dashed line.

In Fig. 8 the solid lines represent the Mach number M, temperature T, density ρ and super-saturation S of the throat location case and the dashed lines those of the baseline. The peak in super-saturation S occurs again at the throat, caused by the decrease in temperature T. The difference is that the peak in S occurs more upstream compared to the baseline. The expansion ratio is the same for both channels, resulting in similar vent conditions for the Mach number M, temperature T, density ρ and solid fraction f.

In Fig. 9 the solid lines represent the nucleation rate γ_{nuc}, solid fraction f, growth rate dR/dz and difference between flow density and equilibrium density $\rho - \rho_{eq}$ of the throat location case and the dashed lines those of the baseline. The peak in nucleation rate γ_{nuc} is smaller than in the baseline. This can be explained by the shape of the channel, resulting in a lower acceleration when approaching the throat. This re-

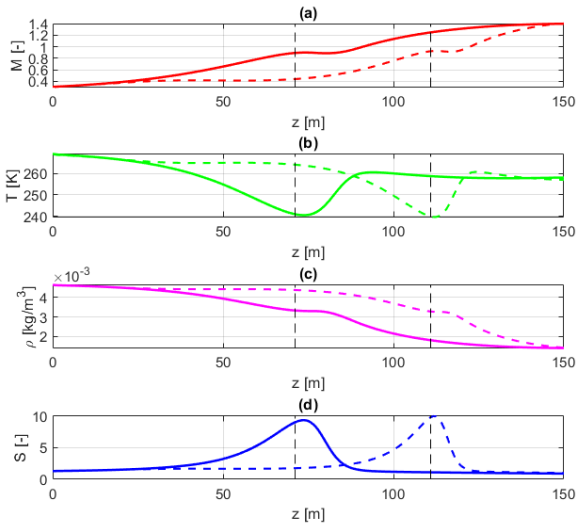

Figure 8: M, T, ρ and S profiles of the baseline channel. The solid lines represent the results for the channel with the new throat location and the dashed lines are the results of the baseline channel, the vertical dashed lines represent the locations of the throats.

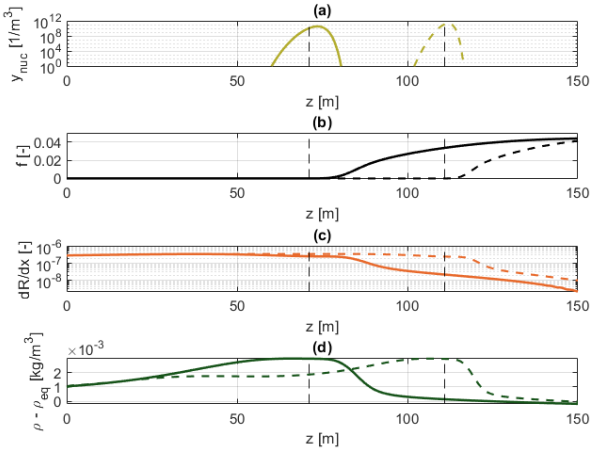

Figure 9: γ_{nuc}, f, dR/dz and $\rho - \rho_{eq}$ profiles. The solid lines are the results for the channel with the new throat location, the dashed lines are the results of the baseline channel, the vertical dashed lines represent the locations of the throats.

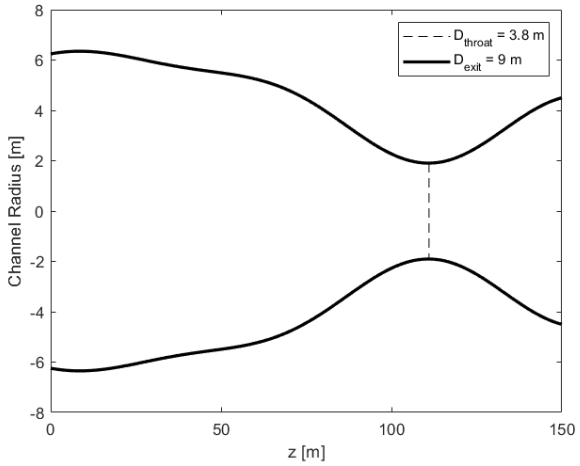

Figure 10: Channel with a D_{exit}/D_{throat} ratio of 2.4 and the throat located at $z = 111$ m, indicated by the dashed line.

sults in more collisions between vapor molecules and therefore a relatively higher T in the throat of the channel. As a result both S and γ_{nuc} decrease compared to the baseline. The peak in γ_{nuc} occurs more upstream, therefore the formed particles can grow over a longer distance, resulting in larger particle sizes. The growth rate dR/dz is proportional to the difference between ρ and ρ_{eq}, which are both positive in the entire channel length. The peak of $\rho - \rho_{eq}$ occurs just after the throat and decreases rapidly, as presented in Fig. 9 (d), this is where the particles experience the fastest growth. As a result the particles at the vent are larger in size compared to the baseline, reaching a mean size of 4.5 μm (Fig. 31). The peak in γ_{nuc} is lower than in the baseline, resulting in a smaller amount of icy particles. f depends both on γ_{nuc} and the growth rate dR/dz, integrated over the longitudinal distance z (Section 2.4.3). Therefore, by moving the throat upstream we marginally increase f, which is 4.4 % at the vent.

4.2.2. Case 4: Smaller throat size

In this section the D_{exit}/D_{throat} ratio is changed from 1.4 to 2.4 to visualise the effect of a faster expansion on the flow parameters.

In Fig. 12 the solid lines represent the Mach number M, temperature T, density ρ and super-saturation S of the smaller throat case and the dashed lines those of the baseline. For the smaller throat case the contraction rate near the throat is higher, causing the flow to accelerate faster. The flow travels faster, resulting in less collisions between vapor molecules in the section just before the throat. As a result, there is less heat generated by condensation, which causes the temperature T to be lower and the super-saturation S to be higher in the throat. The effect that T has on S is illustrated in Fig. 11, i.e., a decrease in T increases S with the given pressure-profile p. The data points for p and T are located to the left of the solid-gas equilibrium line, indicating a super-saturated state of the vapor in the majority of the channel. The increase of S with decreasing T is explained with the equations for the liquid-gas saturation pressure $p_{eq.}^{s.g.}$ and S, Eq. (13) and Eq. (12), respectively. Where $p_{eq.}^{s.g.}$ is shown to decrease faster with T than the flow pressure p, resulting in an increasing S.

At the vent, we observe that the exit Mach number M has increased to 1.75 and T has decreased to 249 K compared to the baseline, which can be explained by a larger D_{exit}/D_{throat} ratio (Anderson and Wendt [2]).

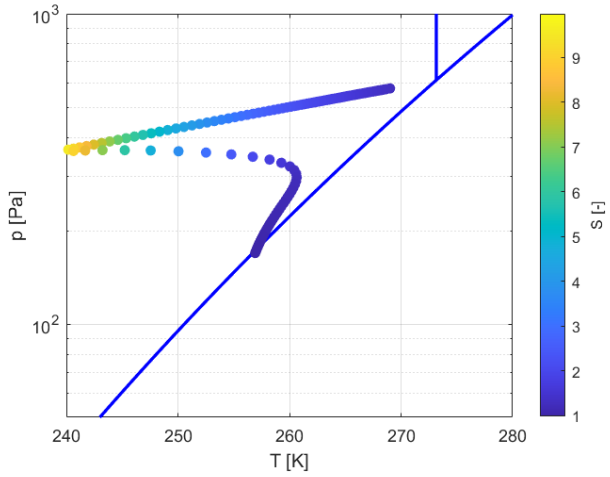

Figure 11: T, p - diagram with S indicated in the color bar. In the throat S is largest and deviates furthest from the thermodynamic equilibrium, the solid blue lines represent the liquid-gas and solid-gas equilibria. In thermodynamic equilibrium left of the solid blue lines corresponds to the solid phase, the right side corresponds to the gas phase and the region in the top-right corner corresponds to the liquid phase. The intersection of the solid blue lines indicates the triple point. $S = 1$ coincides with the blue lines, $S > 1$ lies left of the blue lines.

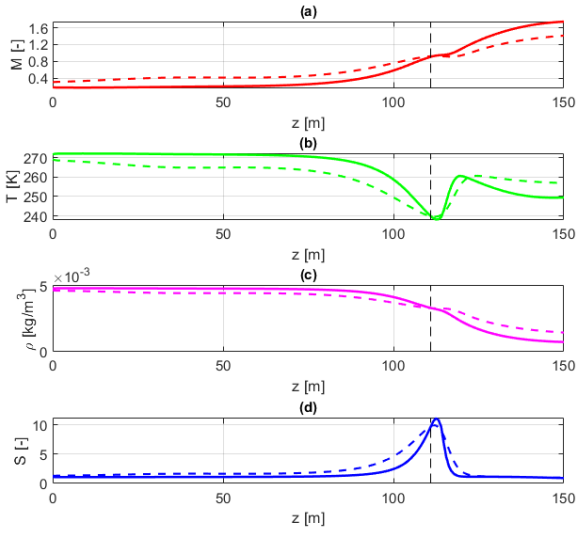

Figure 12: M, T, ρ and S profiles of the channel with a smaller throat (solid lines), compared to the baseline channel (dashed lines), the vertical dashed line represent the throat of the channel.

In Fig. 13 the solid lines represent the nucleation rate γ_{nuc}, solid fraction f, growth rate dR/dz and difference between flow density and equilibrium density $\rho - \rho_{eq}$ of the smaller throat case and the dashed lines those of the baseline. From Eq. (10) we know that a decrease in T and increase in S generates a larger nucleation rate γ_{nuc}. It is observed that the change in T is $+1.5\ K$ and S has increased with 1.25. Physically, this means that with a higher S there are more vapor molecules per unit volume. This results in more collisions between molecules, which leads to particle generation, hence increasing γ_{nuc}. As a result, γ_{nuc} in the throat of the smaller throat case is 18 times larger than for the baseline, therefore more particles are produced near the throat, resulting in a larger solid fraction $f = 6.9\%$. This causes the transition to supersonic speed to occur relatively more upstream and temperature to increases faster just after the throat, since in that region more energy is added to the flow as latent heat. The growth rate dR/dz is smaller compared to the baseline, since it is dependent on the difference between $\rho^{s.g.}_{eq.\ eq}$, which quickly decays after the throat, illustrated in Fig. 16 (d). $\rho^{s.g.}_{eq.}$ is proportional to T, which increases rapidly after the throat, while ρ_{gas} decreases by almost a factor 2. Therefore, dR/dz decreases with a decreasing throat size, resulting in a smaller mean particle size $R = 1.5\ \mu m$ (Fig. 31).

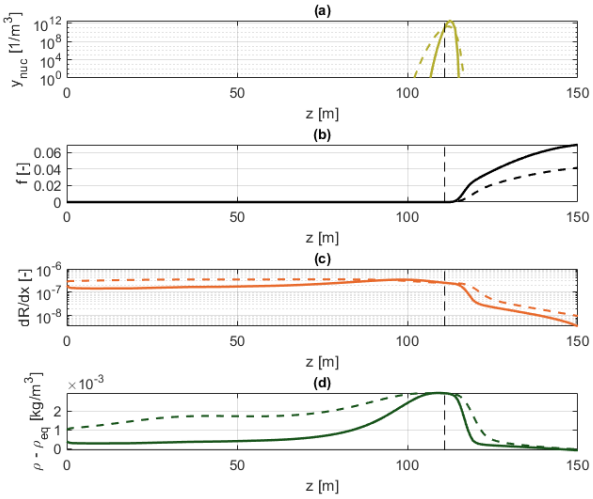

Figure 13: γ_{nuc}, f, dR/dz and $\rho - \rho_{eq}$ profiles of the channel with a smaller throat (solid lines) and the baseline channel (dashed lines), the vertical dashed line represents the location of the throat.

4.2.3. Case 5: Larger throat size

In this section the D_{exit}/D_{throat} ratio is set at 1.2. The channel is illustrated in Fig. 14.

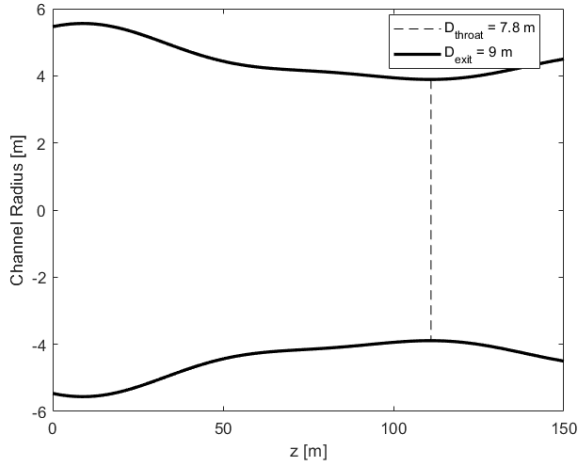

Figure 14: Channel with a D_{exit}/D_{throat} ratio of 1.2 and the throat located at $z = 111$ m, indicated by the dashed line.

In Fig. 15 the solid lines represent the Mach number M, temperature T, density ρ and super-saturation S of the larger throat case and the dashed lines those of the baseline. Near the throat, the conditions are very similar to that of the baseline. The contraction before the throat is slower causing the temperature T to be 1.5 K higher in the throat than in the baseline, as a result the peak in super-saturation S is lower. After the throat, there is less expansion, which results in a lower Mach number M and higher density ρ, illustrated in Fig. 15 (a) and (c). ρ at the exit is almost a factor 2 larger than in the baseline.

In Fig. 16 the solid lines represent the nucleation rate γ_{nuc}, solid fraction f, growth rate dR/dz and difference between flow density and equilibrium density $\rho - \rho_{eq}$ of the channel with a larger throat and the solid lines those of the baseline channel. The lower super-saturation S in the throat causes the nucleation rate γ_{nuc} to decrease with a factor 21. Therefore, less particles are produced and a lower solid fraction f is obtained (Fig. 16 (b)). f increases slowly along the z-axis and therefore there is less heat release, causing T to be lower just after the throat. As a result of the higher ρ and lower T just after the throat, $\rho - \rho_{eq}$ increases compared to the baseline (Fig. 16 (d)). This results in a larger dR/dz and therefore larger particles ($R = 5.5\mu m$). There are less particles generated, therefore the solid fraction is smaller than in the baseline, $f = 3.2\%$ (Fig. 16 (b)).

4.2.4. Case 6: Channel width

In this section the channel width is decreased with a factor 2 and consequently the parameters related to width, D_{exit} and D_{throat}, are also decreased by a factor 2. This is done

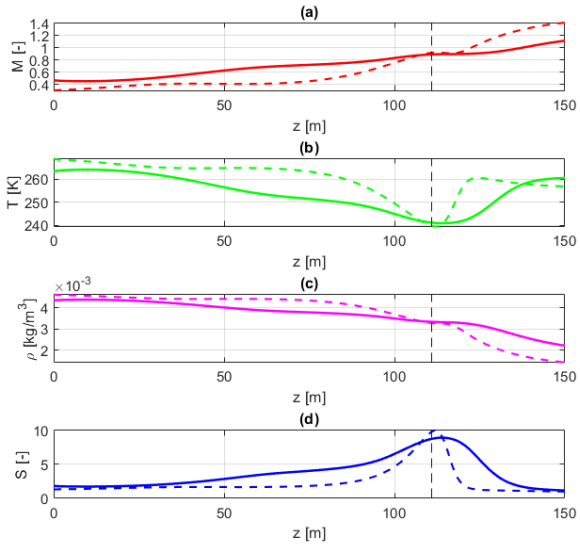

Figure 15: M, T, ρ and S profiles of the channel with a larger throat (solid lines), compared to the baseline channel (dashed lines), the vertical dashed line represent the throat of the channel.

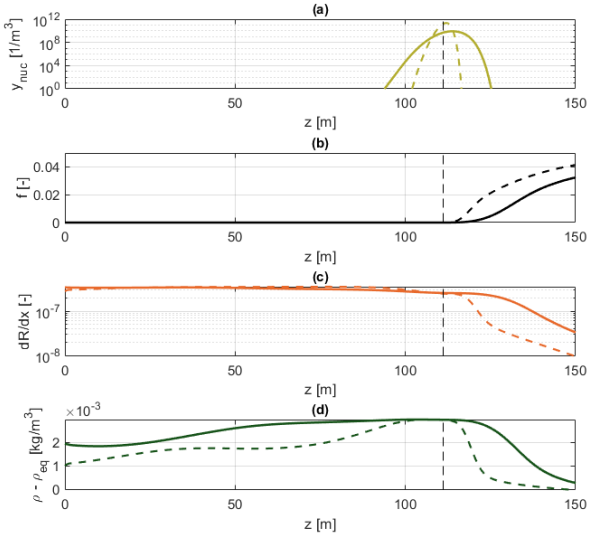

Figure 16: γ_{nuc}, f, dR/dz and $\rho - \rho_{eq}$ profiles of the channel with a larger throat (solid lines) and the baseline channel (dashed lines), the vertical dashed line represents the location of the throat.

to assess the sensitivity of the flow characteristics to such a change. Only the mass flow $\dot{m}$ is affected, it has decreased with a factor 2. The rest of the parameters are insensitive to a change in width, since the equations describing the flow and condensation are invariant under a positive change in width. The flow parameters are identical to those of the baseline channel (Fig. 5).

4.2.5. Case 7: Increased channel length

In Fig. 17 the solid lines represent the Mach number M, temperature T, density ρ and super-saturation S of the increased length case and the dashed lines those of the baseline. The change in length of the channel shows only minor differences compared to the baseline channel, it is observed that the flow parameters are almost identical, since the shape of the channel is the same. However, the peak in super-saturation S at the throat is a fraction smaller than in the baseline. Since the flow has a longer distance to adapt to the contraction, i.e. more collisions between molecules occur resulting in more generated particles and therefore more heat release. This heat release increases the temperature T and as a consequence the peak in S is lower, due to the increase of the liquid-gas saturation vapor density $\rho_{l.g._{eq.}}$.

In Fig. 18 the solid lines represent the nucleation rate γ_{nuc}, solid fraction f, growth rate dR/dz and difference between flow density and equilibrium density $\rho - \rho_{eq}$ of the increased length case and the dashed lines those of the baseline. γ_{nuc} in the throat is significantly lower, as a result of the lower peak in S, illustrated in Fig. 18 (a). However, the reduced peak of γ_{nuc} acts over a longer distance resulting in a similar amount of solid particles. Together with a similar growth rate dR/dz, the solid fraction f is similar as in the baseline. The mean particle size R does show a significant increase. This is as expected since dR/dz is similar, but the distance over which the particles grow is 2 times larger. Increasing the mean particle radius to $R = 5.4\mu m$ (Fig. 31).

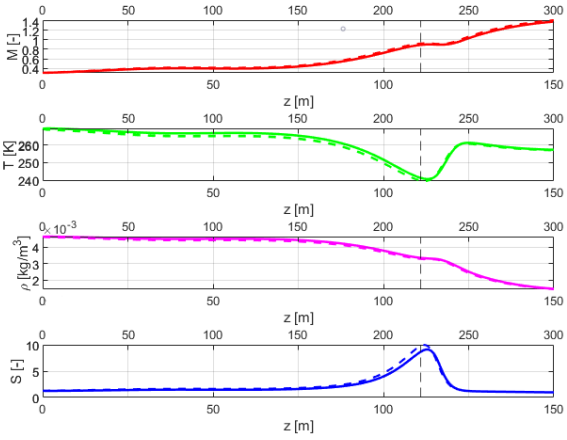

Figure 17: M, T, ρ and S profiles of the channel with a length of 300 m (solid lines and top z-axis), compared to the baseline channel (dashed lines, bottom z-axis).

4.2.6. Case 8: Irregular channel

The irregularity of the channel is governed by the correlation length, discussed in Section 3.3. In the baseline this was set to 60 m and in this case has been reduced to 15 m. The irregular channel is presented in Fig. 19.

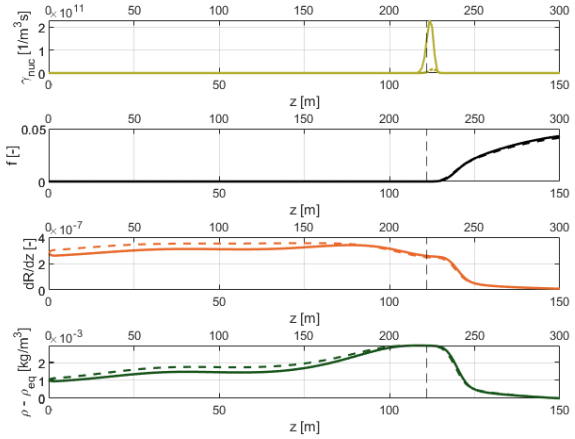

Figure 18: γ_{nuc}, f, dR/dz and $\rho - \rho_{eq}$ profiles of the channel with a length of 300 m (solid lines and top z-axis) and the baseline channel (dashed lines and bottom z-axis), the vertical dashed line represents the location of the throat.

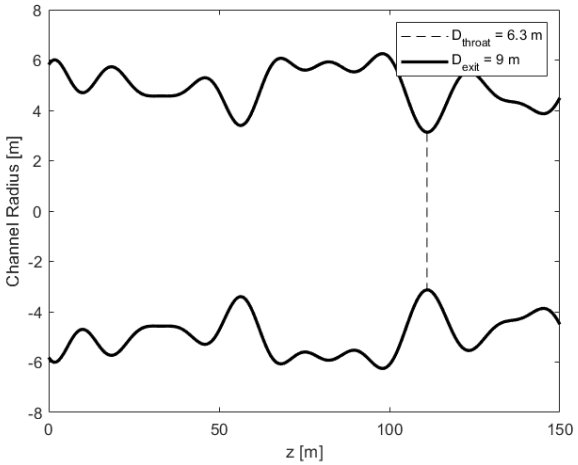

Figure 19: Channel with a D_{exit}/D_{throat} ratio of 1.4 and the throat located at $z = 111$ m, indicated by the dashed line, the correlation length is changed to $L_0 = 15$ m.

In Fig. 20 the solid lines represent the Mach number M, temperature T, density ρ and super-saturation S of the irregular channel and the dashed lines those of the baseline channel. The effect of the irregular shape of the channel is that the Mach M and temperature T profiles fluctuates significantly. The contraction near the throat is very fast, resulting in a lower T and higher super-saturation S. The peak of S is much more narrow than in the baseline, also caused by rapid contraction. The density ρ after the throat is lower than in the baseline, except near the vent where the channel contracts. M at the exit is 0.1 lower than in the baseline. The irregular shape of the channel has damping effect on the flow velocity, i.e. the exit value of M reduces illustrated in Fig. 20 (a). This implies that subsequent contractions and expansions do not cancel out, as M_{exit} is lower than in the baseline.

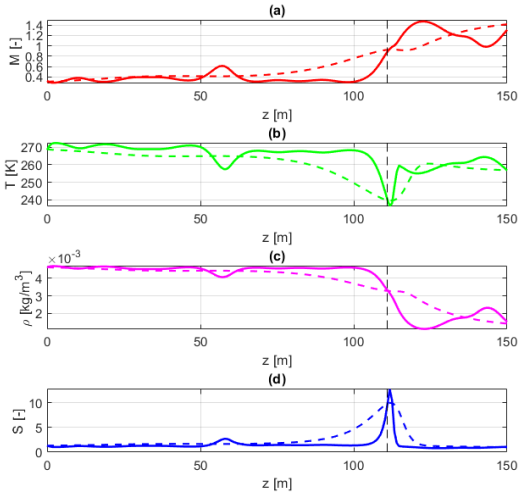

Figure 20: M, T, ρ and S profiles of the irregular channel (solid lines), compared to the baseline channel (dashed lines), the vertical dashed line represent the throat of the channel.

In Fig. 21 the solid lines represent the nucleation rate γ_{nuc}, solid fraction f, growth rate dR/dz and difference between flow density and equilibrium density $\rho - \rho_{eq}$ of the irregular channel case and the dashed lines those of the baseline. As a result of the higher peak in S in the throat, the nucleation rate γ_{nuc} is larger as well. The growth rate dR/dz is much lower after the throat, than in the baseline, caused by a region of contraction where $M > 1$. This causes the flow to decelerate and T to increase, as a result both $\rho - \rho_{eq}$ and dR/dz become negative (Fig. 21 (c)). Therefore, an irregular shaped channel implies that the mean particle size ($R = 0.5\mu m$, Fig. 31) and solid fraction decrease $f = 3.9\%$.

4.2.7. *Case 9: Reservoir with higher pressure* (+200 *Pa*)

Here the effect of changing the reservoir conditions is examined. To date it is unknown what exactly the reservoir conditions are, for the baseline the reservoir conditions are set at triple point (Porco et al. [37], Schmidt et al. [40]). In this section the reservoir conditions are moved along the ice-liquid equilibrium line by adding 200 Pa. This results in a reservoir temperature of 273.15 K and a pressure of 811.2 Pa.

In Fig. 22 the solid lines represent the Mach number M, temperature T, density ρ and super-saturation S of the increased pressure case and the dashed lines those of the baseline. As a result of the increased pressure p, the density ρ is significantly higher, causing the flow to be more dense. Therefore, there are more collisions between the vapor molecules, generating more latent heat and causing the temperature T in the throat to be higher and super-saturation

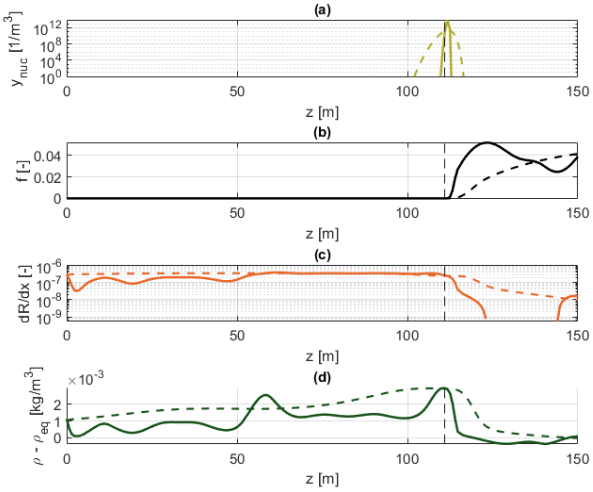

Figure 21: γ_{nuc}, f, dR/dz and $\rho - \rho_{eq}$ profiles of the irregular channel (solid lines) and the baseline channel (dashed lines), the vertical dashed line represents the location of the throat.

S to be lower than in the baseline.

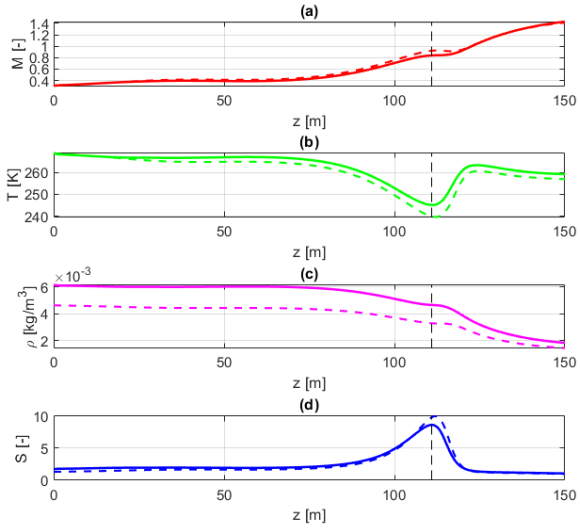

Figure 22: M, T, ρ and S profiles of the irregular channel (solid lines), compared to the baseline channel (dashed lines), the vertical dashed line represent the throat of the channel.

In Fig. 23 the solid lines represent the nucleation rate γ_{nuc}, solid fraction f, growth rate dR/dz and difference between flow density and equilibrium density $\rho - \rho_{eq}$ of the increased pressure case and the dashed lines those of the baseline. The increased T and decreased S in the throat result in a lower nucleation rate γ_{nuc}, according to Eq. (10) and Eq. (11). Due to the increased ρ, the growth rate dR/dz is larger in the majority of the channel, Eq. (14). This increases

the mean particle size to $R = 4.2\ \mu m$ and increases the solid fraction to $f = 4.7\%$.

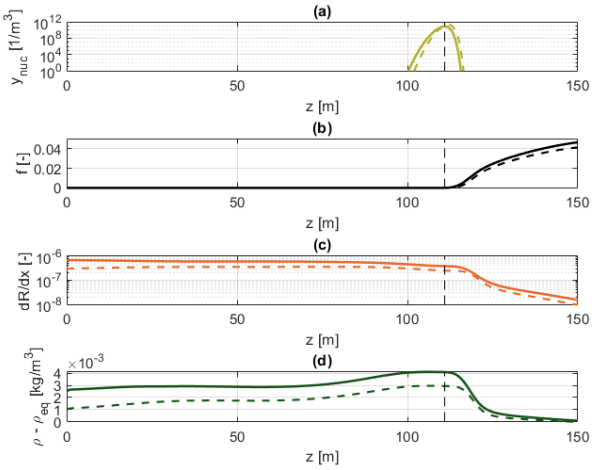

Figure 23: γ_{nuc}, f, dR/dz and $\rho - \rho_{eq}$ profiles of the baseline channel with an increase in p of 200 Pa (solid lines) and the baseline channel (dashed lines), the vertical dashed line represents the location of the throat.

4.2.8. *Case 10: Reservoir with higher temperature (+10 K)*

In this section we change the reservoir conditions by adding 10 K and take the saturated vapor pressure on the vapor-liquid interface. This results in $T = 283.16\ K$, $p = 1228.4\ Pa$ and $\rho = 9.4 \cdot 10^{-3}\ kg/m^3$, according to the ideal gas law, Eq. (9).

In Fig. 24 the solid lines represent the Mach number M, temperature T, density ρ and super-saturation S of the increased temperature case and the dashed lines those of the baseline. The profiles of the flow parameters look similar as in the baseline channel, however the temperature T and density ρ are significantly higher. Due to the increase of T, the super-saturation S in the throat is lower, since $\rho_{eq}^{(l.g.)}$ increases relatively more than ρ_{gas} with temperature.

In Fig. 25 the solid lines represent the nucleation rate γ_{nuc}, solid fraction f, growth rate dR/dz and difference between flow density and equilibrium density $\rho - \rho_{eq}$ of the increased temperature case and the dashed lines those of the baseline. The nucleation rate γ_{nuc} in the throat is similar to that of the baseline since S has decreased, but T has increased. However, the difference between both densities $\rho - \rho_{eq}$ increases, illustrated in Fig. 25. This results in a higher growth rate $\frac{dR}{dz}$, according to Eq. (11) and Eq. (14) and therefore larger particles ($R = 4.7 \mu m$).

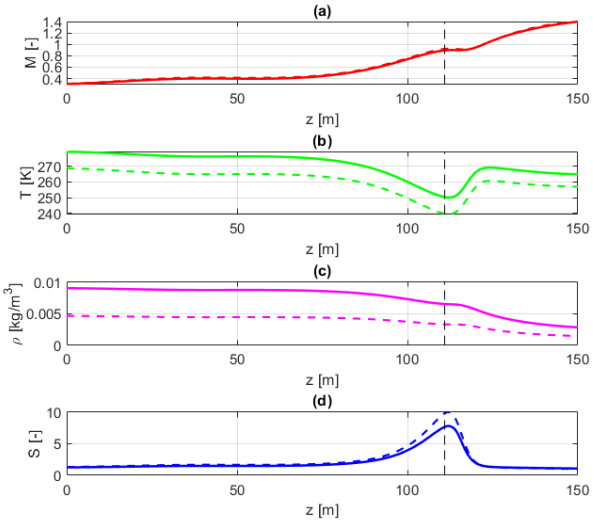

Figure 24: M, T, ρ and S profiles of the baseline channel with an increase in T of 10 K (solid lines), compared to the baseline channel (dashed lines), the vertical dashed line represent the throat of the channel.

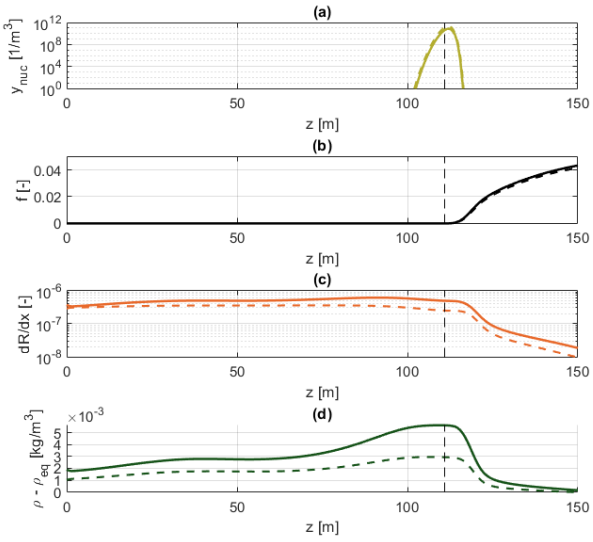

Figure 25: γ_{nuc}, f, dR/dz and $\rho - \rho_{eq}$ profiles of the the baseline channel with an increase in T of 10 K (solid lines) and the baseline channel (dashed lines), the vertical dashed line represents the location of the throat.

4.3. Model with wall interactions

The importance of wall interactions in the model becomes apparent when we consider the mean thermal velocity V_{th} of the flow. V_{th} is approximately 560 m/s in most cases, according to Eq. (21). The velocity of the flow V ranges approximately from $100 - 700\ m/s$. In Fig. 26 V_{th} is plotted versus V, which shows us that the thermal velocity dominates in the majority of the channel. This implies that the

vapor has continuous interactions with the walls, since the thermal velocity has a random direction, in contrast to the flow velocity, which is assumed to be only in longitudinal direction. Due to the magnitude of the mean thermal velocity compared to the flow velocity, the effects of interactions with the walls must be considered, which we model according to the equations in Section 2.5. The results of the incorporation of accretion and sublimation are shown in Section 2.5. The effects of friction and convection are neglected, since their contributions are significantly smaller than those of accretion and sublimation and this allows for better interpretation of the effects of accretion and sublimation on the plume characteristics.

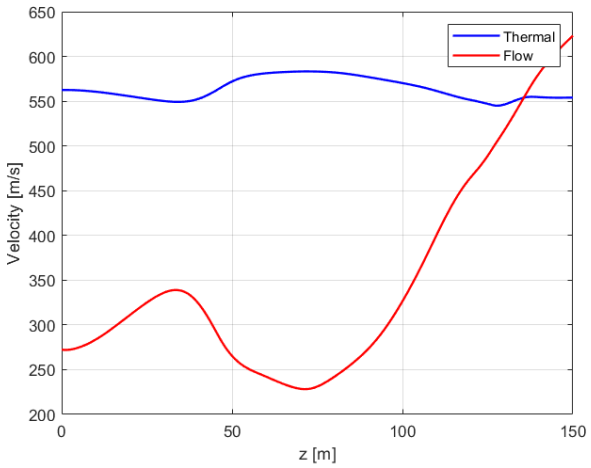

Figure 26: Flow velocity versus thermal velocity.

4.3.1. Case 11: Wall interactions

In this section the wall interactions are added to the multiphase model. The flow of the baseline channel is computed with reservoir conditions set at triple point. In Eq. (42) the mass flow in the channel is presented, where A is the cross-section of the channel. Here it is observed that the mass flow near the reservoir is relatively high, 2652 kg/s,and decreases towards the vent, 1085 kg/s. The mass flow is reduced by accretion to the walls and increased by sublimation from the walls, according to Eq. (28) and Eq. (30), respectively.

From Fig. 28 it is observed that the accretion rate dominates the sublimation rate by a factor 10. This explains the mass flow reducing towards the vent. The dominance of accretion can be explained by the thermal velocity, $V_{th} \approx 560\ m/s$. By comparison to the actual flow velocity V, we observe that V_{th} is larger in magnitude in the majority of the channel (Fig. 26). The thermal velocity is random in direction, which implies that a very high number of vapor molecules collides with the walls, resulting in a significant mass flow rate into the walls ($\dot{m}_w \approx 3.5 - 13\ kg/ms$).

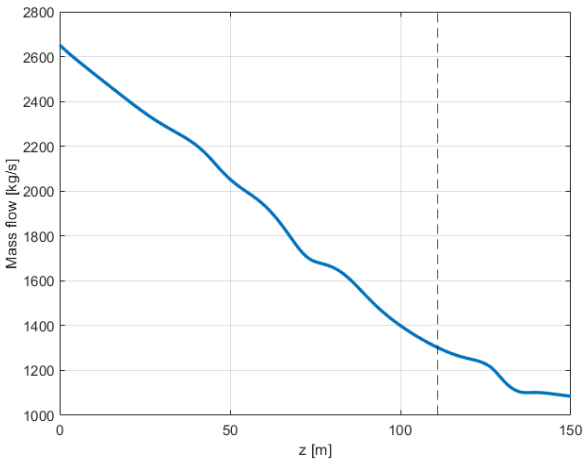

Figure 27: Mass flow in kg/s, along the z-axis for the wall interactions model. $\dot{m}$ is computed with Eq. (42), where A is the cross-section of the channel.

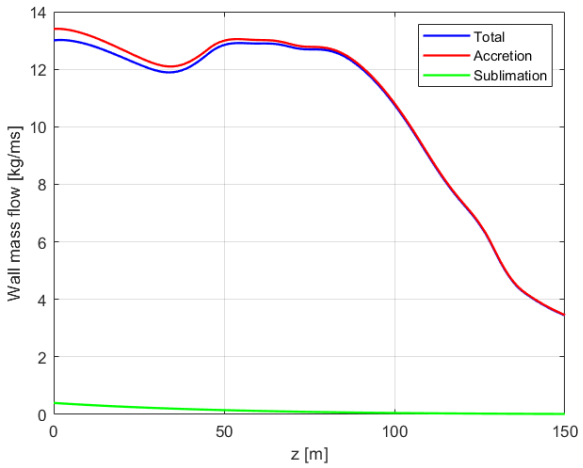

Figure 28: Mass rate of accretion and sublimation in kg/ms.

In Fig. 29 the solid lines represent the Mach number M, temperature T, density ρ and super-saturation S of the wall interactions model and the dashed lines those of the baseline. From the top panel of Fig. 29 it is observed that the initial Mach number M is higher than in the baseline. This is caused by the fact that the flow is choked in the throat and that the mass flow near the reservoir is significantly higher. For this mass flow, a higher Mach number M is required. Due to this increased initial velocity V, the initial density ρ and temperature T both decrease. As the flow accelerates towards the surface, T decreases even further. At $z = 33\ m$, T has dropped to 241 K, which causes a peak in the super-saturation level S, illustrated in Fig. 29 (d).

In Fig. 30 the solid lines represent the nucleation rate γ_{nuc}, solid fraction f, growth rate dR/dz and difference between flow density and equilibrium density $\rho - \rho_{eq}$ of the wall interactions model and the dashed lines those of the base-

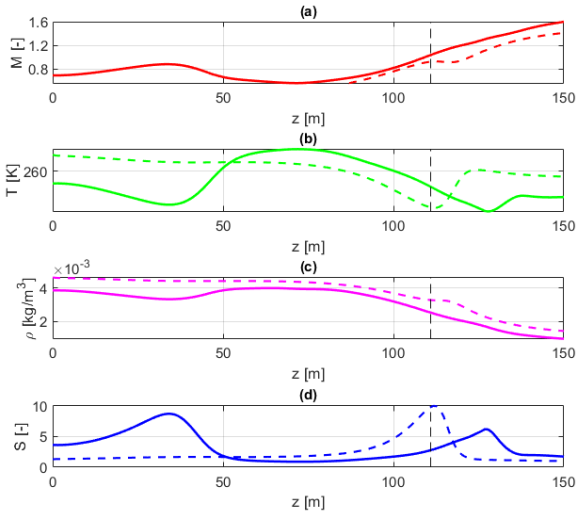

Figure 29: M, T, ρ and S profiles of the baseline channel computed with wall interactions (solid lines), compared to the baseline channel computed with the multi-phase model (dashed lines), the vertical dashed line represents the throat of the channel.

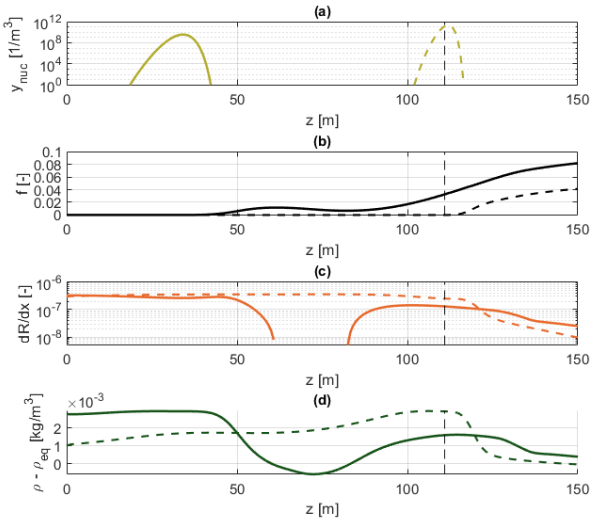

Figure 30: γ_{nuc}, f, dR/dz and $\rho - \rho_{eq}$ profiles of the the baseline channel computed with wall interactions (solid lines) and the baseline channel computed with the multi-phase model (dashed lines), the vertical dashed line represents the location of the throat.

line. As a result of the peak in S at $z = 33\ m$, the nucleation rate γ_{nuc} is locally enhanced. This causes many particles to form that subsequently start to grow, illustrated in Fig. 30 (a) and (c). Since the particles originate earlier in the channel compared to the baseline, they have a longer distance to grow and reach a mean size of $R = 10\mu m$ (Fig. 31). As a result of the increased particle sizes, the solid fraction also increases to $f = 8.2\%$. Therefore, more heat is released as latent heat into the flow, resulting in a temperature increase of $\Delta T = 30K$, Fig. 30. This increase in T causes S, γ_{nuc} and dR/dz to decrease. When dR/dz is positive the particles grow and when it is negative the particles shrink due to evaporation (Eq. (14)), f behaves proportional to dR/dz. Due to the increased f, there is more energy released into the flow as latent heat, causing the flow to accelerate further to $M = 1.6$.

In Fig. 31 the mean particle sizes of the baseline (Multi-phase), throat location, smaller throat, longer channel, irregular channel and wall interactions cases are presented. Table 3 present a summary of the Mach number M, velocity V, solid fraction f, mean particle size R and mass flow $\dot{m}$ of all the simulated cases.

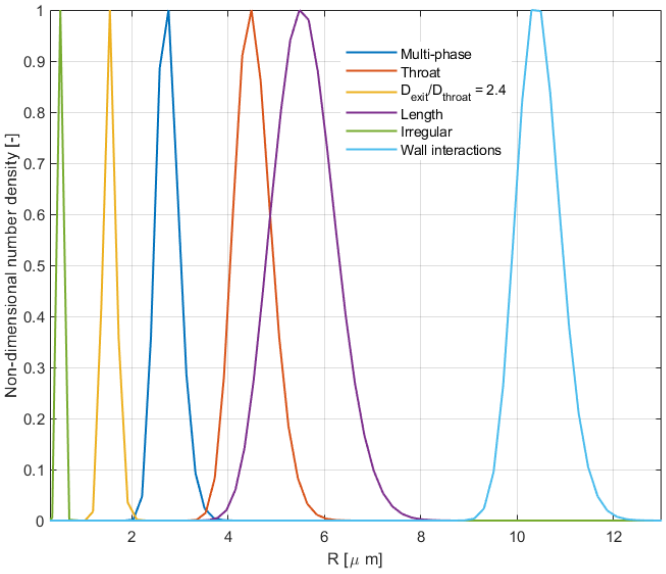

Figure 31: The mean particle sizes R of the cases; baseline (Multi-phase), throat location, smaller throat, longer channel, irregular channel and wall interactions model. The peak in number density of each particle size is made non-dimensional for the sake of comparison. Explanation of the generated particle sizes is given in the text.

Table 3
Numerical results of the different cases.

Isentropic, multi-phase and wall interactions models.							
n	Case	M_{exit}	$V(m/s)$	$f(\%)$	$T_{exit}(K)$	$R(\mu m)$	$\dot{m}(\frac{kg}{s})$
1	Isentropic	1.8	587	-	180	-	1464
2	Multi-phase	1.41	562	4.1	257	2.8	1460
3	Throat	1.41	558	4.4	258	4.5	1435
4	$\uparrow D_{exit}/D_{throat}$	1.75	684	6.9	249	1.5	872
5	$\downarrow D_{exit}/D_{throat}$	1.12	448	3.2	261	5.5	1792
6	Width	1.41	562	4.1	257	2.8	730
7	Length	1.41	550	4.3	257	5.4	1440
8	Irregular	1.31	519	3.9	257	0.5	1390
9	Reservoir +200 Pa	1.43	571	4.7	259	4.2	1910
10	Reservoir +10 K	1.40	566	4.3	265	4.7	2865
11	Wall interactions	1.6	623	8.2	246	10	1085

4.4. Linking plume characteristics and channel properties

From the results of the parameter study of the crevasse properties, some links between the plume characteristics and the channel properties are determined and presented in this section. In Fig. 32 these relations are visualised, note that this figure is not to scale and that some properties are enlarged to emphasise the links between plume characteristics and the crevasse properties.

Some relations were already well-known from literature (Anderson and Wendt [2]), such as that the Mach number M and velocity V increase with the exit diameter D_{exit} over throat diameter D_{throat} ratio: $V \propto D_{exit}/D_{throat}$, illustrated with the blue arrow in Fig. 32.

A channel with a faster acceleration tends to be more out of thermodynamic equilibrium, resulting in a lower temperature T in the throat, therefore also a larger S in the throat. A faster acceleration, and thus higher S, is realised by increasing the expansion ratio D_{exit}/D_{throat} or decreasing the channel length. This is confirmed by the results, where we find that the super-saturation S in the throat is proportional to the D_{exit}/D_{throat} ratio and inversely proportional to the length of the channel L, therefore we find that: $S \propto D_{exit}/D_{throat} \propto 1/L$. This enhances the nucleation rate γ_{nuc} and the formation of particles. Since more particles originate, the solid fraction f also increases with D_{exit}/D_{throat}. We therefore find that: $f \propto D_{exit}/D_{throat}$, illustrated with the red label in Fig. 32.

The growth rate dR/dz decreases with the expansion ratio, caused by a rapid decrease in density ρ due to this expansion. As a result the particle size decreases with the expansion ratio. We therefore find that: $1/R \propto D_{exit}/D_{throat}$. However, we find that the length of the channel and the location of the throat have a much more important effect on the particle size R. Both these effects result in a longer distance for the particles to grow, resulting in larger particle sizes. We therefore find that: $R \propto L$, indicated by the pink label in Fig. 32.

The reservoir conditions have been studied by changing the reservoir from triple point to an ice-liquid mixture (+200 Pa) and a vapor-liquid mixture (+10 K). With increased pressure (+200 Pa), the density increased according to the ideal gas law (Eq. (9)), which increased S at the throat. This resulted in a higher γ_{nuc} and a similar dR/dz, as a result f slightly increased. With higher temperatures (+10 K) in Section 4.2.8) the dR/dz increased and γ_{nuc} decreased, resulting in less particles with a larger size. As a result f remained approximately constant.

The growth rate is dominantly dependent on the difference between gas density ρ_{gas} and the saturated vapor density ρ_{eq}. Where at high temperatures the difference is generally larger, resulting in a larger growth rate (Section 4.2.8). Whereas, expansion reduces ρ_{gas} and results in a lower growth rate. We therefore find that: $dR/dz \propto T_{res} \propto 1/(D_{exit}/D_{throat})$.

The temperature of the flow T seems to stay between $220 - 260$ K and doesn't change much after the throat. This is caused by the balance of expansion, which reduces T and latent heat release, which increases T. However, if the expansion is strong, T will further decrease to lower temperatures ≤ 210 K. We therefore find that: $1/T \propto D_{exit}/D_{throat}$, indicated with the green label.

The interactions with the wall have a significant influence on the mass flow, accretion is the dominant mechanism and reduces the mass flow. As a result of the decreasing mass flow along the $z-axis$ the initial velocity V increases, since near the reservoir the mass flow is higher. Therefore, also the initial temperature T decreases. As the flow accelerates, T decreases further, resulting in an increase of S. This causes γ_{nuc} to increase and particle formation to occur earlier in the channel, before the throat. As a result, the particles have a longer distance to grow and become larger in size. Therefore, not only the distance from the throat to the exit, but rather the entire length of the channel L increases the mean particle size R, therefore we find that: $R \propto L$. The increase in R causes f to increase and generate more latent heat, which further accelerates the flow. Therefore, accretion increases M, f and R and decreases $\dot{m}$.

The overall effect of the wall interactions is that mass is lost into the walls and that nucleation and particle growth starts earlier in the channel. If the channel is longer or narrower, there is more mass accreting onto the walls. Thus when considering wall interactions, a longer, narrower crevasse increases M, f and R and decreases $\dot{m}$.

5. Constraining Enceladus' crevasses properties from Cassini data

In Table 4 the plume characteristics are listed, which are derived from Cassini measurements. We aim to constrain the crevasses' properties with the data derived from Cassini's observations. How the plumes characteristics are obtained is discussed briefly below.

The surface temperature T of the Tiger Stripes fissures is measured by the CIRS to be at least 170 K (Spencer and Waite [45]). The hot spots along the Tiger Stripes are measured to have temperatures of $T = 210$ K, obtained from UVIS and VIMS data (Tenishev et al. [49]).

The solid fraction f is determined with UVIS and ISS data,

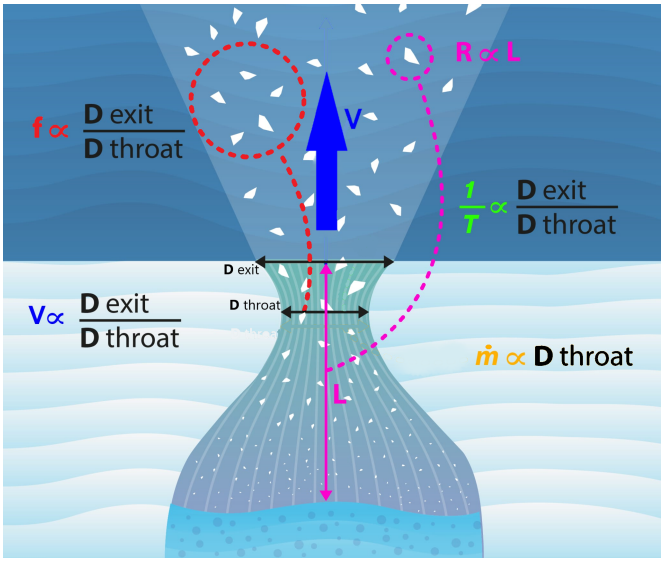

Figure 32: Schematic illustration of the reservoir, crevasse and plume, presented to illustrate the links between plume characteristics and crevasse properties. In this figure there are two black arrows, the top one represents the exit diameter D_{exit} and the bottom one the throat diameter D_{throat}, this ratio is proportional to the velocity V (blue) and the solid fraction f (red), and inversely proportional to the vent temperature T (green). The throat diameter is proportional to the mass flow $\dot{m}$ (orange). The pink arrow represents the length of the channel and is proportional to the particle size R (pink), the icy particles are presented as the white flakes. These flakes grow until they reach the surface, from here they are ejected into space, where large particles tend to fall back on the surface of Enceladus and smaller particles ($R = 0.1 - 3\ \mu m$) feed the E-ring (Kempf et al. [25]). Note that this figure is not to scale.

which gives the molecular abundance of water vapor and water ice grains at $7 - 30\ km$ and $15\ km$ altitude, respectively. By considering different particle size distributions, these are generated with the effective particle size ranging from $0.5-2$ μm and the breadth of the particle size distribution ranging from $0.1 - 0.25$, a solid fraction of $0.1 - 0.2$ is found (Kieffer et al. [27]). Since the water ice grains abundance is measured at $15\ km$ altitude, some grains are not observed, since they don't reach $15\ km$ altitude and some grains are doubly counted as they fall back to the surface. This effect can only be considered if further measurements at lower altitudes in the plume become available Kieffer et al. [27]. Gao et al. [12] estimates a solid fraction of 0.07 considering irregular aggregates formed from spherical monomers. Therefore, we aim to reproduce a solid fraction ranging from $0.07 - 0.2$.
For the particle size distribution, we find the mean size of particles observed with the UVIS and VIMS to be within $0.1 - 3\ \mu m$ (Hedman et al. [19]). However, larger particles (up to $75\ \mu m$) tend to fall back to the surface again and are not observed (Guzman et al. [14]).
The plume velocity is estimated between $350 - 950\ m/s$ by fitting the UVIS and INMS data (Tian et al. [51], Dong et al. [11], Smith et al. [42]). Teolis et al. [50] estimates higher velocities to fit the peak of the CO abundancies in the plume,

Table 4
Plume characteristics from Cassini observations, see text for the references.

Isentropic, multi-phase and wall interactions models.				
$T\ (K)$	$\dot{m}\ (kg/s)$	$V\ (m/s)$	$f\ (-)$	$R\ (\mu m)$
$170-210$	$100-1000$	$350-950$	$0.07-0.2$	$0.1-75$

where 12% of the plume is estimated to have a Mach number of 16. However, this estimate has in inaccuracy of ±30%, these are therefore not taken into account in this study.
The mass flow is estimated between $100 - 1000\ kg/s$ from UVIS stellar and solar occultations. These estimates vary with the flyby number, $E14$, $E17$, $E18$ in the study of Teolis et al. [50] and $E4$ and $E5$ for the studies of Dong et al. [11] and Smith et al. [42] and whether stellar or solar occultations are used (Jurac and Richardson [24], Burger et al. [6]).

A channel that reproduces these observed plume characteristics by Cassini has a length of $150 - 1000\ m$ to generate particles of sizes ranging from $0.1-75\ \mu m$, a large expansion ratio D_{exit}/D_{throat} close to 4 and a reservoir temperature that is probably close to $273.16\ K$. This strong expanding section near the throat is needed to reach sufficiently high velocities (up to $950\ m/s$) near the surface that reduce the exit temperature below $210\ K$ and generate a solid fraction in the range of $0.07 - 0.2$.

6. Discussion

In this section the results are compared to the data of the Cassini mission and the overall outcome of the study is discussed.

6.1. Expansion ratio

The expansion ratio is estimated close to $D_{exit}/D_{throat} = 4$, in order to obtain exit temperatures $\leq 210\ K$. This ratio can be higher or lower, dependent on the shape of the channel. The irregular channel case, implies that irregularity of the channel has a damping effect on the Mach number M and velocity V. This reduces the flow velocity and increases temperature T, therefore the required D_{exit}/D_{throat} ratio for an irregular channel can be higher. In a longer or narrower channel there is more mass accreting on the walls, this results in a lower mass flow and nucleation and particle growth to occur earlier in the channel. This releases more heat in the flow causing the flow to accelerate, this increases V and reduces T, therefore the D_{exit}/D_{throat} ratio can be lower for long and narrow channels. There is a limit to the length and narrowness of the channel, in some extreme cases the mass flow approaches zero or the channel freezes up completely.
The main source of the plumes is expected to be liquid water, to be able to explain the $\sim 0.5 - 2\%$ in mass of sodium salts in the E-ring (Postberg et al. [38]). For the reservoir to be liquid and to be in near equilibrium with the surrounding ice, it must be close to $273\ K$. Such a reservoir temperature is in agreement with our simulations to achieve an exit tempera-

ture $\leq 210\ K$. Higher reservoir temperatures would require a higher D_{exit}/D_{throat} ratio, which then produces velocities that are higher than observed.

6.2. Particle size

From the study of Hedman et al. [19] we find that there is a peak in particle size at 1 μm. However, other studies indicate that particles of 75 μm are also ejected by the plumes, but fall back on to the surface near the vents (Kempf et al. [25]). For particles of $\approx 3\ \mu m$, channels of of 150 m would be sufficient. However, particles of 75 μm would require a much longer channel, up to a kilometre. The large spread of the particle sizes could be explained by a set of channels with the throat at different locations. The channel shape can change over time due to accretion and being cracked open by tidal friction. The closer the throat is to the surface, the smaller the particles will be.

A fraction of the particles could be larger in size, since we consider a steady-state rate of evaporation as the source of the vapor flow. However, it could also be that boiling occurs in the reservoir (Ingersoll and Nakajima [22]). The bubbles that reach the reservoir surface burst and form a mix of vapor and tiny droplets. Generally the vapor near the reservoir is super-saturated, resulting in growth of the new formed droplets. Since these particles originate from the reservoir, they will have a longer distance to grow over and will result in significantly larger particles near the vent.

The obtained solid fraction f by Kieffer et al. [27] and Gao et al. [12] can in reality be higher or lower due to the dynamics of larger particles. Some particles do not reach the altitude at which the measurements were performed and some particles might fall back to the surface from altitudes higher than the measurement altitude, therefore particles can be doubly counted or not counted at all. This could be improved by new measurements at a lower altitude.

6.3. Grain velocity

In the model, the velocity of the grains and vapor is considered to be equal, which is not in agreement with Schmidt et al. [40]. The grains tend to be slower than the gas in the flow, caused by wall collisions and re-acceleration by the gas. The grains and gas are coupled if the gas density is high enough, but when the density decreases they decouple. When the flow is accelerating the grains will be slower, however if the gas is decelerating the grains will be faster. The majority of the grains travels at $2/3$ of the velocity of the gas (Schmidt et al. [40]), and since the solid fraction is quite low ($f \leq 0.2$) this does not have an significant impact on the flow. Implying that the difference in velocities has little effect on the conservation equations and therefore it is neglected.

6.4. Venting length

The venting area is assumed to be rectangular, with a venting length along the Tiger Stripes and a width orthogonal to this the length. The tiger stripes are 500 km long, however the intensity of the plume along these Tiger Stripes is not constant. It has been observed that the majority of the plume mass flow originates from certain hot spots along these tiger stripes (Burger et al. [6], Tenishev et al. [49]). This makes the venting length much shorter than the length of the Tiger Stripes. An venting area of 200 m^2 is estimated in the work of Schmidt et al. [40] and 3750 m^2 in the work of Nakajima and Ingersoll [33]. In this work we have chosen a venting area of 1800 m^2, which is the average of the estimates in the work of Schmidt et al. [40] and Nakajima and Ingersoll [33], as it is unclear what the actual active venting area is. With this venting area, a D_{throat}/D_{exit} ratio close to 4 and $D_{throat} = 2.1\ m$, a mass flow of approximately 200 kg/s is obtained, which is in agreement with the observed mass flow.

6.5. Sublimation and sticking methods

In this study we used the sublimation method of Hasegawa and Herbst (Hasegawa et al. [18]), explained in Section 2.5.2. However, for amorphous and/or crystalline ice there are several methods to compute the sublimation rate (M. Minissale [29], Speedy et al. [44]). The rate of sublimation calculated with the method of Speedy et al. [44] is approximately 1000 times larger than with Hasegawa and Herbst (M. Minissale [29]). This results in completely different evolution of the crevasse, in the bottom part the sublimation would be dominant and in the upper part the accretion would be dominant. The effect of this on the crevasse would be that the bottom is widening and the top is closing, resulting in a bell-shaped crevasse.

For the sticking coefficient there are also different methods. Veeraghattam et al. [52] presents a sticking coefficient of $c_{stick} \approx 0.2$ for a temperature of the gas in the range of $T = 210 - 270\ K$. The sticking coefficient is determined for H atoms, but this is similar for H_2O molecules, since both are weakly bound species (Cazaux et al. [8]). In the work of Cazaux et al. [8] a sticking coefficient of $c_{stick} \approx 0.4$ is obtained. A higher sticking coefficient results in a higher accretion rate, where more mass is deposited into the walls.

6.6. Opening and closing of the crevasses

Our results show that accretion is dominant in the channel and that as an effect, the channel will seal up over time. However, the plumes are measured with similar intensity over time, meaning that the crevasses are opened up again (Goguen et al. [13]). The mechanism for opening the cracks are the diurnal tides experienced by Enceladus (Spencer et al. [47]). We argue that the crevasses are closed by accretion on the walls. The mass flow into the walls for the channel that fits the Cassini observations ranges from $0.002 - 0.07$ $kg/m^2 s$, with a channel diameter ranging from $2.1 - 12\ m$. Translating this to a number of atoms and computing the number of atoms per unit area of the walls, we can determine the layers per second that are added to the walls. This layer being the size of a H_2O atom (3Å). From this we determine the velocity at which the crevasse seals up at $0.2 - 5$ m/day. With the given channel width, it would take $2 - 10$ days for the crevasse to seal up. These timescales are rather short, however the orbital period of Enceladus is also short

(1.5 days). Channels with a smaller vent area produce less mass flow, this implies that the opening and closing of the crevasses is related to observed intensity variations during an orbital period of Enceladus ([21]. As a results of the dynamic geometry of the crevasses, the plume characteristics also change over time and location. In this study we have examined several crevasse types with different shapes and found several channels that could fit the observed data of Cassini. This agrees with the fact that the crevasses have different and changing shapes and produce a range of plume characteristics, of which the observed values are stated in Table 4.

7. Conclusion

In this study we linked plume characteristics to the crevasse properties, being the channel's length, width, throat size, throat location and the reservoir conditions. We present a purely isentropic model, a multi-phase model and a model that includes wall interactions. The multi-phase model considers nucleation and particle growth, resulting in a phase change caused by condensation of the saturated vapor. The model with wall interactions also considers accretion into the walls and sublimation from the walls. The plume characteristics computed from Cassini observations, can be reproduced by a plume model containing nucleation, particle growth and the wall interactions.
Here the links are presented between the plume characteristics and the crevasse properties, determined from the results of this study. Finally, we present the crevasse properties that produce the observed plume characteristics.

- **Length:** The length of the channel seems to have negligible effect on most of the flow parameters. However, the mean particle size behaves proportional to the length of the channel. Smaller particles that feed the E-ring ranging from $0.1 - 3\ \mu m$ can be produced with a channel length of approximately 150 m, but the larger particles that fall back on Enceladus ($75\mu m$) would require channel lengths up to a kilometre.

- **Throat size:** A change in throat size with a given exit diameter results in a change in the contraction and expansion rate. This increases the exit Mach number and solid fraction, but reduces the mass flow, mean particle size and exit temperature.

- **Throat location:** A throat located deeper in the channel causes condensation to occur earlier. Therefore, the particles have a longer distance to grow over, resulting in a larger mean size of the particles. Likewise, a throat closer to the surface produces smaller particles.

- **Irregularity:** The irregularity of the channel causes the flow parameters to fluctuate in the channel and causes the exit parameters to be damped. I.e., the solid fraction, mean particle size and Mach number at the exit are lower.

- **Reservoir conditions:** An increase in pressure and temperature causes the flow to be more dense, resulting in a higher solid fraction, larger particles, Mach number and exit temperature.

- **Wall interactions:** The wall interactions cause the flow to lose mass to the walls and therefore reduce the mass flow. This increases the initial velocity and decreases the initial temperature of the flow. Nucleation and particle growth occurs earlier in the channel, resulting in a larger solid fraction, particle size and Mach number and a lower exit temperature. Longer and narrower channels move the location of nucleation and particle growth more upstream and enhance the previously stated effects of wall interactions.

To match the observed plume characteristics by Cassini, the channel length ranges from $150 - 1000\ m$, to generate the wide range of particle sizes ($0.1 - 75\ \mu m$) and to be in agreement with the estimated shell thickness. The channel requires an expansion ratio close to $D_{throat}/D_{exit} = 4$, to generate the observed exit temperature $\leq 210\ K$ with velocities up to $950\ m/s$ and a solid fraction ranging from $0.07 - 0.2$. The minimum width of the channel needs to be in the order of meters to withhold the channel from freezing up within days and a liquid reservoir at a temperature near triple point is most probable to agree with the observed exit temperature and velocity.

References

[1] A. Howett, Anne J. Verbiscer, J.H.W., 2006. Enceladus and the icy moons of saturn, p. 478.

[2] Anderson, J.D., Wendt, J., 1995. Computational fluid dynamics. volume 206. Springer.

[3] Atkins, de Paula, 2007. Molecules in motion. Oxford Higher Education 272, 1–8.

[4] Bland, M.T., Singer, K.N., McKinnon, W.B., Schenk, P.M., 2012. Enceladus' extreme heat flux as revealed by its relaxed craters. Geophysical Research Letters 39.

[5] Buch, V., Zhang, Q., 1991. Sticking probability of h and d atoms on amorphous ice-a computational study. The Astrophysical Journal 379, 647–652.

[6] Burger, M., Sittler Jr, E., Johnson, R., Smith, H., Tucker, O., Shematovich, V., 2007. Understanding the escape of water from enceladus. Journal of Geophysical Research: Space Physics 112.

[7] Čadek, O., Tobie, G., Van Hoolst, T., Massé, M., Choblet, G., Lefèvre, A., Mitri, G., Baland, R.M., Běhounková, M., Bourgeois, O., et al., 2016. Enceladus's internal ocean and ice shell constrained from cassini gravity, shape, and libration data. Geophysical Research Letters 43, 5653–5660.

[8] Cazaux, S., Morisset, S., Spaans, M., Allouche, A., 2011. When sticking influences h2 formation. Astronomy & Astrophysics 535, A27.

[9] Crifo, J., 1989. Inferences concerning water vapour viscosity and mean free path at low temperatures. Astronomy and Astrophysics 223, 365.

[10] Cuppen, H., Kristensen, L., Gavardi, E., 2010. H2 reformation in post-shock regions. Monthly Notices of the Royal Astronomical Society: Letters 406, L11–L15.

[11] Dong, Y., Hill, T., Teolis, B., Magee, B., Waite, J., 2011. The water vapor plumes of enceladus. Journal of Geophysical Research: Space Physics 116.

[12] Gao, P., Kopparla, P., Zhang, X., Ingersoll, A.P., 2016. Aggregate particles in the plumes of enceladus. Icarus 264, 227–238.

[13] Goguen, J.D., Buratti, B.J., Brown, R.H., Clark, R.N., Nicholson, P.D., Hedman, M.M., Howell, R.R., Sotin, C., Cruikshank, D.P., Baines, K.H., et al., 2013. The temperature and width of an active fissure on enceladus measured with cassini vims during the 14 april 2012 south pole flyover. Icarus 226, 1128–1137.

[14] Guzman, M., Lorenz, R., Hurley, D., Farrell, W., Spencer, J., Hansen, C., Hurford, T., Ibea, J., Carlson, P., McKay, C.P., 2019. Collecting amino acids in the enceladus plume. International Journal of Astrobiology 18, 47–59.

[15] Hansen, C., Esposito, L., Stewart, A., Meinke, B., Wallis, B., Colwell, J., Hendrix, A., Larsen, K., Pryor, W., Tian, F., 2008. Water vapour jets inside the plume of gas leaving enceladus. Nature 456, 477–479.

[16] Hansen, C., Shemansky, D.E., Esposito, L.W., Stewart, A., Lewis, B., Colwell, J., Hendrix, A., West, R.A., Waite Jr, J., Teolis, B., et al., 2011. The composition and structure of the enceladus plume. Geophysical Research Letters 38.

[17] Hansen, C.J., Esposito, L., Stewart, A., Colwell, J., Hendrix, A., Pryor, W., Shemansky, D., West, R., 2006. Enceladus' water vapor plume. Science 311, 1422–1425.

[18] Hasegawa, T.I., Herbst, E., Leung, C.M., 1992. Models of gas-grain chemistry in dense interstellar clouds with complex organic molecules. The Astrophysical Journal Supplement Series 82, 167–195.

[19] Hedman, M., Nicholson, P., Showalter, M., Brown, R., Buratti, B., Clark, R., 2009. Spectral observations of the enceladus plume with cassini-vims. The Astrophysical Journal 693, 1749.

[20] Ingersoll, A.P., Ewald, S.P., 2011. Total particulate mass in enceladus plumes and mass of saturn's e ring inferred from cassini iss images. Icarus 216, 492–506.

[21] Ingersoll, A.P., Ewald, S.P., Trumbo, S.K., 2020. Time variability of the enceladus plumes: Orbital periods, decadal periods, and aperiodic change. Icarus 344, 113345.

[22] Ingersoll, A.P., Nakajima, M., 2016. Controlled boiling on enceladus. 2. model of the liquid-filled cracks. Icarus 272, 319–326.

[23] Ingersoll, A.P., Pankine, A.A., 2010. Subsurface heat transfer on enceladus: Conditions under which melting occurs. Icarus 206, 594–607.

[24] Jurac, S., Richardson, J., 2005. A self-consistent model of plasma and neutrals at saturn: Neutral cloud morphology. Journal of Geophysical Research: Space Physics 110.

[25] Kempf, S., Beckmann, U., Schmidt, J., 2010. How the enceladus dust plume feeds saturn's e ring. Icarus 206, 446–457.

[26] Kieffer, S.W., Lu, X., Bethke, C.M., Spencer, J.R., Marshak, S., Navrotsky, A., 2006. A clathrate reservoir hypothesis for enceladus' south polar plume. Science 314, 1764–1766.

[27] Kieffer, S.W., Lu, X., McFarquhar, G., Wohletz, K.H., 2009. A redetermination of the ice/vapor ratio of enceladus' plumes: Implications for sublimation and the lack of a liquid water reservoir. Icarus 203, 238–241.

[28] Lucchetti, A., Pozzobon, R., Mazzarini, F., Cremonese, G., Massironi, M., 2017. Brittle ice shell thickness of enceladus from fracture distribution analysis. Icarus 297, 252–264.

[29] M. Minissale, Y. Aikawa, E.B.M.B.W.A.B.S.C.S.C.A.C.H.M.C., 2021. Thermal desorption parameters of ices and their implications from snowlines to chemical complexity. The Journal of Chemical Physics 112, 55.

[30] Matson, D.L., Castillo-Rogez, J.C., Davies, A.G., Johnson, T.V., 2012. Enceladus: A hypothesis for bringing both heat and chemicals to the surface. Icarus 221, 53–62.

[31] McLennan, J., Grimmett, L., Read, J., 1935. Production of radioactivity by neutrons. Nature 135, 505–505.

[32] Mills, A.F., 1999. Basic heat and mass transfer. Pearson College Division.

[33] Nakajima, M., Ingersoll, A.P., 2016. Controlled boiling on enceladus. 1. model of the vapor-driven jets. Icarus 272, 309–318.

[34] Nimmo, F., Spencer, J., Pappalardo, R., Mullen, M., 2007. Shear heating as the origin of the plumes and heat flux on enceladus. Nature 447, 289–291.

[35] Peeters, P., Gielis, J., Van Dongen, M., 2002. The nucleation behavior of supercooled water vapor in helium. The Journal of chemical physics 117, 5647–5653.

[36] Porco, C., DiNino, D., Nimmo, F., 2014. How the geysers, tidal stresses, and thermal emission across the south polar terrain of enceladus are related. The Astronomical Journal 148, 45.

[37] Porco, C.C., Helfenstein, P., Thomas, P., Ingersoll, A., Wisdom, J., West, R., Neukum, G., Denk, T., Wagner, R., Roatsch, T., et al., 2006. Cassini observes the active south pole of enceladus. science 311, 1393–1401.

[38] Postberg, F., Kempf, S., Schmidt, J., Brilliantov, N., Beinsen, A., Abel, B., Buck, U., Srama, R., 2009. Sodium salts in e-ring ice grains from an ocean below the surface of enceladus. Nature 459, 1098–1101.

[39] Saur, J., Schilling, N., Neubauer, F.M., Strobel, D.F., Simon, S., Dougherty, M.K., Russell, C.T., Pappalardo, R.T., 2008. Evidence for temporal variability of enceladus' gas jets: Modeling of cassini observations. Geophysical research letters 35.

[40] Schmidt, J., Brilliantov, N., Spahn, F., Kempf, S., 2008. Slow dust in enceladus' plume from condensation and wall collisions in tiger stripe fractures. Nature 451, 685–688.

[41] Shevkunov, S., 2006. Clusterization of water molecules on crystalline β-agi surface. computer experiment. Colloid Journal 68, 632–643.

[42] Smith, H., Johnson, R., Perry, M., Mitchell, D., McNutt, R., Young, D., 2010. Enceladus plume variability and the neutral gas densities in saturn's magnetosphere. Journal of Geophysical Research: Space Physics 115.

[43] Smith, R.S., May, R.A., Kay, B.D., 2016. Desorption kinetics of ar, kr, xe, n2, o2, co, methane, ethane, and propane from graphene and amorphous solid water surfaces. The Journal of Physical Chemistry B 120, 1979–1987.

[44] Speedy, R.J., Debenedetti, P.G., Smith, R.S., Huang, C., Kay, B.D., 1996. The evaporation rate, free energy, and entropy of amorphous water at 150 k. The Journal of chemical physics 105, 240–244.

[45] Spencer, J. R., A.C.B.L.W.E.P.H.A.P.I.R.J.C.P.M.F.N., Waite, J.H., 2009. Enceladus: An active cryovolcanic satellite, in: Saturn From Cassini-Huygens, pp. 73–199.

[46] Spencer, J., Howett, C., Verbiscer, A., Hurford, T., Segura, M., Spencer, D., 2013. Enceladus heat flow from high spatial resolution thermal emission observations. EPSC Abstracts 8, 840–1.

[47] Spencer, J., Nimmo, F., Ingersoll, A.P., Hurford, T., Kite, E., Rhoden, A., Schmidt, J., Howett, C., 2018. Plume origins and plumbing: from ocean to surface. Enceladus and the icy moons of Saturn , 163–174.

[48] Spitale, J.N., Porco, C.C., 2007. Association of the jets of enceladus with the warmest regions on its south-polar fractures. Nature 449, 695–697.

[49] Tenishev, V., Öztürk, D.C.S., Combi, M.R., Rubin, M., Waite, J.H., Perry, M., 2014. Effect of the tiger stripes on the water vapor distribution in enceladus' exosphere. Journal of Geophysical Research: Planets 119, 2658–2667.

[50] Teolis, B.D., Perry, M.E., Hansen, C.J., Waite, J.H., Porco, C.C., Spencer, J.R., Howett, C.J., 2017. Enceladus plume structure and time variability: comparison of cassini observations. Astrobiology 17, 926–940.

[51] Tian, F., Stewart, A., Toon, O.B., Larsen, K.W., Esposito, L.W., 2007. Monte carlo simulations of the water vapor plumes on enceladus. Icarus 188, 154–161.

[52] Veeraghattam, V.K., Manrodt, K., Lewis, S.P., Stancil, P., 2014. The sticking of atomic hydrogen on amorphous water ice. The Astrophysical Journal 790, 4.

[53] Viisanen, Y., Strey, R., Reiss, H., 1993. Homogeneous nucleation rates for water. The Journal of chemical physics 99, 4680–4692.

[54] Viisanen, Y., Strey, R., Reiss, H., 2000. Erratum:"homogeneous nu-

cleation rates for water"[j. chem. phys. 99, 4680 (1993)]. The Journal of Chemical Physics 112, 8205–8206.
[55] Wölk, J., Strey, R., 2001. Homogeneous nucleation of h2o and d2o in comparison: the isotope effect. The Journal of Physical Chemistry B 105, 11683–11701.
[56] Wölk, J., Strey, R., Heath, C.H., Wyslouzil, B.E., 2002. Empirical function for homogeneous water nucleation rates. The Journal of chemical physics 117, 4954–4960.
[57] Zierep, J., 1980. Theory of flows in compressible media with heat addition. Fluid Dynamics Transactions 10, 213–240.
[58] Zolotov, M.Y., 2007. An oceanic composition on early and today's enceladus. Geophysical Research Letters 34.

A. Validation and Verification

In this section all the different parts of validation and verification are presented. The verification and validation of the multi-phase model, nucleation method and wall mass flux are presented in Appendix A.1 and Appendix A.2 and Appendix A.3, respectively.

A.1. Multi-phase model

The multi-phase model has been validated using the numerical data of Schmidt et al. [40]. The validation data consist of profiles for V, T, ρ, p, S, γ_{nuc}, R and f for two given channels. The output of the multi-phase model (dashed-coloured lines) is compared to the validation data (solid blue lines), in Fig. 34 and Fig. 35. The channel is illustrated in Fig. 33. The results are in satisfying agreement, showing

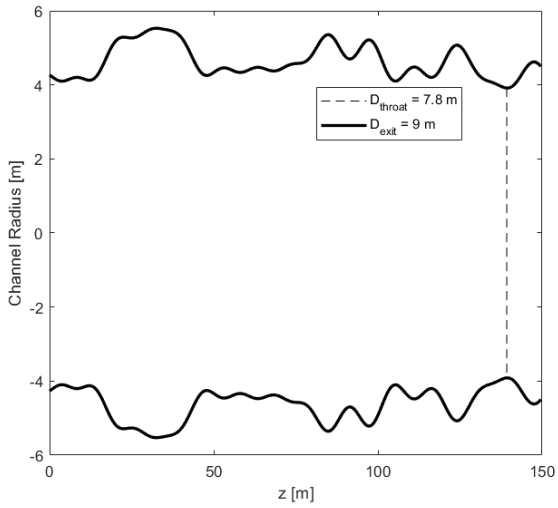

Figure 33: Channel used for the validation of the multi-phase model.

the verification of the multi-phase model.

A.2. Nucleation

The nucleation method employed in the work of Schmidt et al. [40] follows from a direct fit to experimental data of water nucleation (Viisanen et al. [53]):

$$\gamma_{\mathrm{nuc}} = B\left(T_{\mathrm{gas}}\right)(S-1)^{n\left(T_{\mathrm{gas}}\right)} \tag{43}$$

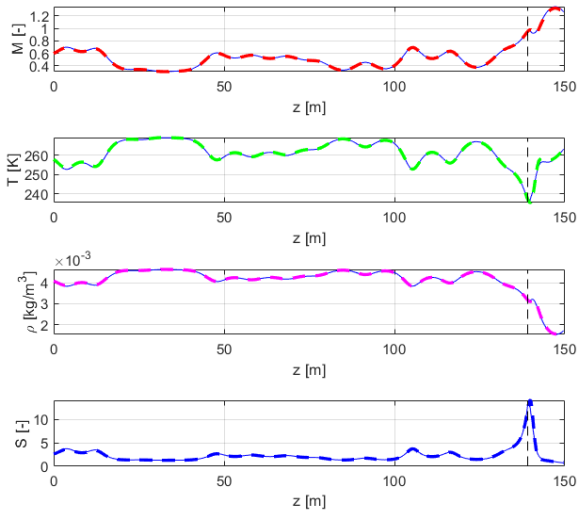

Figure 34: Verification of the multi-phase model with the data set from Schmidt et al. [40], flow parameters M, T, ρ and S.

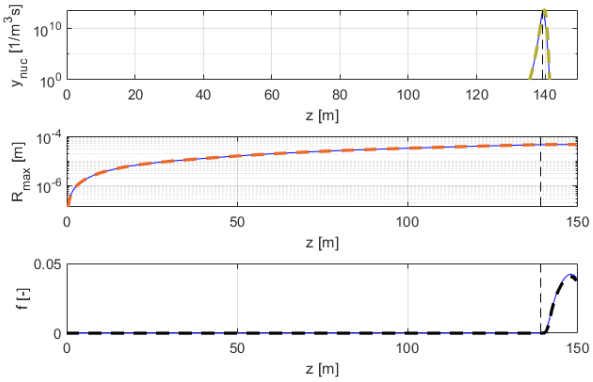

Figure 35: Verification of the multi-phase model with the data set from Schmidt et al. [40], flow parameters γ_{nuc}, the maximum particle size (generated from the reservoir) R and f.

Where the super-saturation S is computed by dividing the gas density ρ_{gas} by its corresponding saturated value $\rho_{eq}^{(l.g.)}$:

$$S = \frac{\rho_{\mathrm{gas}}}{\rho_{\mathrm{eq}}^{(l.g.)}\left(T_{\mathrm{gas}}\right)} \tag{44}$$

The temperature dependent coefficients are fitted to the data, resulting in:

$$\log_{10}\left[B\left(T_{\mathrm{gas}}\right)\right] = -32.025880 - 0.070074889T_{\mathrm{gas}} + 0.00040240774T_{\mathrm{gas}}^2 \tag{45}$$

$$n\left(T_{\mathrm{gas}}\right) = 1.1743362 + 0.011626596T_{\mathrm{gas}} + 0.00047597152T_{\mathrm{gas}}^2 \tag{46}$$

These equations are fitted to the nucleation data from experiments, illustrated in Fig. 37. However, in Viisanen et al. [54]

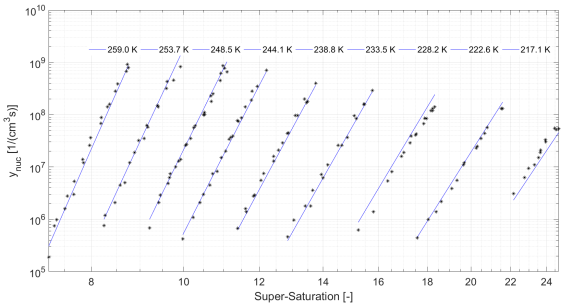

Figure 36: The nucleation rate γ_{nuc} and the dependency on super-saturation S, from experiments (Viisanen et al. [53]). At fixed temperatures the output follows from the relation of Eq. (45). The coefficients B and n are generated from a linear fit of $log(\gamma_{nuc})$ to $log(S-1)$. $B(T)$ and $n(T)$ are generated from quadratic fits to these coefficients (Schmidt et al. [40]). The blue lines are the outcome of the nucleation function and the stars are the data points, the associated temperatures are given at the top of the blue lines.

the nucleation data has be reanalysed and a different method of transformation was used. In Wölk and Strey [55] the nucleation rate experiments for H_2O have been redone with identical conditions, for comparison. In these experiments the in- and outlet-valves of the reaction chamber have been modified and enhanced compared to prior experiments. An empirical function has been presented, based on the generated data. This function originates from the Böring-Decker equation (Eq. (10)), but is corrected for tmeperature (Eq. (11)). For the purpose of verification, we present the output of Eq. (10) and Eq. (11) compared to the nucleation data of Wölk and Strey [55]. A satisfying correlation is observed for the nucleation data and Eq. (11).

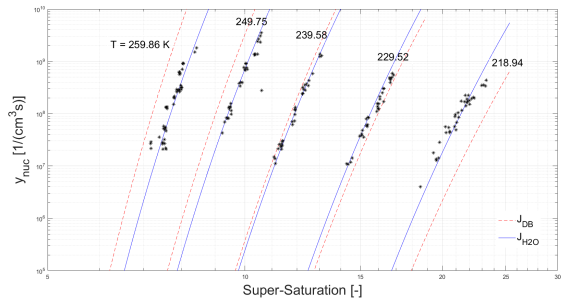

Figure 37: The nucleation rate γ_{nuc} and the dependency on super-saturation S, from experiments (Wölk and Strey [55]). The nucleation data points are given by the black stars, the red-dashed lines represent the output of Eq. (10) and the blue lines are the output of Eq. (11). Clearly, the latter is in best agreement with the nucleation data.

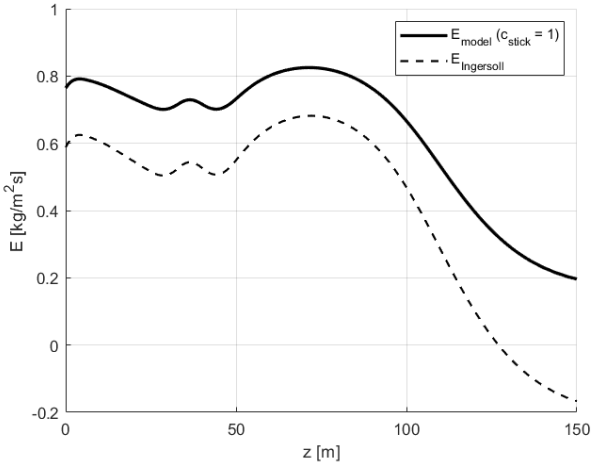

Figure 38: Comparison of wall mass flux per unit area E. The behaviour of E is similar in both cases, only the magnitude differs $\sim 30\%$. The outcome serves as a method of validation for the new accretion model of this paper.

A.3. Wall mass flux

Validation of the wall mass flux, consisting of accretion and sublimation, is performed by comparison with Eq. (47) (Nakajima and Ingersoll [33]). E is the wall mass flux into the walls per unit area. We compute E for the baseline channel using the multi-phase model with wall interactions, where we compare the outcome to Eq. (47).

$$E = 2\left(\frac{p}{\sqrt{2\pi RT/M}} - \frac{p_w}{\sqrt{2\pi RT_w/M}}\right) \tag{47}$$

Where E is the wall mass flux per unit area $[kg/m^2s]$, R is the gas constant, M is the molar mass T_w is the temperature of the wall $[K]$ and p_w is the saturation vapor pressure at the temperature of the wall, written as:

$$p_w = 3.63 \cdot 10^{12} e^{(-6147/T_w)} \tag{48}$$

The results of this comparison are given in Fig. 38. The results are very similar, although this is only true for a sticking coefficient of 1. The difference between the results is therefore partially explained by the sticking coefficient. The method in both cases is also different, this paper uses a more physical approach, considering individual collisions with the wall. Whereas, in the validation data an empirical relation is used that neglects the redistribution of the flow after collisions and the fact that not the whole flow interacts with the walls. After each collision the flow is assumed to redistribute, the layer of particles near the wall will be in equilibrium with the wall (Ingersoll and Pankine [23]). But, the particles that do not interact with the wall, will not necessarily be in equilibrium with the walls.

3

Conclusions and recommendations

3.1. Conclusions

The research questions from Section 1.1 are repeated here, and with the findings from Chapter 2 a series of conclusions have been drawn and research questions are answered.

1. **Can different plume models reproduce the characteristics of the plumes observed by Cassini?**

   (a) **An isentropic model:** By isentropically computing the flow, one assumes that the flow is adiabatic and reversible. I.e., no energy transformations occur due to friction or dissipative effects and no heat is added to the flow. From the results it became evident that a phase change is present in the flow. During this phase change, vapor condensates and release latent heat. This latent heat is a form of heat that is added to the flow, which violates the assumptions of isentropic flow. The necessity of a phase change indicates that an isentropic model does not physically represent the characteristics of the plume.

   (b) **A multi-phase model:** In the multi-phase model, we consider multiple phases in the flow, it accounts for nucleation, particle growth and the generated solid fraction. The flow has a velocity upwards in longitudinal direction, but also a random motion, generated by the thermal velocity. Since the thermal velocity is larger than the longitudinal velocity in the majority of the channel, we must consider its effect on the flow. The random motion causes the vapor to collide with the walls and causes a fraction of that vapor to stick to the walls, called accretion. Accretion reduces the mass flow and the vent temperature and increases the solid fraction and particle size. Also, the velocity near the walls approaches zero, whereas the flow velocity can be several hundreds of meters per second. This causes friction near the walls, which slows the flow down by reducing its momentum. The multi-phase model does not account for these effects and can therefore not realistically represent the characteristics of the plume.

   (c) **A model that accounts for wall interactions:** In this model the effects of accretion on the walls, sublimation from the walls, heat convection through the walls and friction with the walls are accounted for. Combined with the phase change, this provides a rather complete set of equations to solve for the plume characteristics. With the stated aspects of the model and a crevasse that has a length of $150 - 1000\ m$, an expansion ratio D_{exit}/D_{throat} close to 4 and a reservoir near triple point, we find the characteristics of the plume as they where measured by Cassini and stated in literature.

2. **How does the geometry of the crevasse change the plumes' characteristics?**

   (a) **Length:** The length of the channel seems to have negligible effect on the flow parameters itself. I.e. the solid fraction, vent temperature and velocity are unaltered, however the mean particle size behaves proportional to the length of the channel. Particle sizes of $3\ \mu m$ require a channel length of approximately $150\ m$, but the larger particles that fall back on Enceladus ($75 \mu m$) would require channel lengths up to a kilometre.

(b) **Width:** For the multi-phase model the plume parameters are invariant to the width of the channel when the wall interactions are not included, since the equations for channel flow and condensation are not dependent on any transformation of $D \rightarrow \alpha D$. However, the total mass flow is proportional to the width of the channel, since it determines the venting area of the crevasse, being the length of the crack multiplied with the width of the crack at the exit.

(c) **Throat size:** A change in throat size with a given exit diameter results in a change in the expansion rate. With a higher expansion rate, the flow accelerates faster. As a result the flow is further from it thermodynamics equilibrium, causing the temperature in the throat to be lower and the super-saturation to be higher. As a result more particles are generated by a higher nucleation rate, and the solid fraction increases. The density of the flow decreases faster in expansion and causes the mean particle size to reduce with expansion. Therefore, expansion rate is proportional to the solid fraction and the velocity of the plumes and inversely proportional to the temperature, and mean particle radius.

(d) **Throat location:** The throat locations causes condensation to occur earlier in the channel. Therefore, the particles have a longer distance to grow over. Since the flow continues to accelerate, the temperature decreases and the flow remains super-saturated, as a result the particles continue to grow. Since the particles have a longer distance to grow, they are larger in size at the vent.

(e) **Irregularity:** The irregularity of the channel causes the flow parameters to fluctuate in the channel and causes the exit parameters to be damped. I.e., the solid fraction, mean particle size and Mach number at the exit are lower.

(f) **Reservoir conditions:** An increase in pressure and temperature causes the flow to be more dense, resulting in a higher solid fraction, larger particles, Mach number and exit temperature.

3. **How do wall interactions change the characteristics of the plume?** The wall interactions cause the flow to lose mass to the walls and therefore reduce the mass flow. This increases the initial velocity and decreases the initial temperature of the flow. Nucleation and particle growth occurs earlier in the channel, resulting in a larger solid fraction, particle size and Mach number and a lower exit temperature. Longer and narrower channels increase the amount of collisions with the walls and move the location of nucleation and particle growth more upstream. This further decreases the mass flow and causes the initial temperature to be lower, as an effect the flow is more super-saturated and the phase change starts at lower depths in the channel. Therefore, the solid fraction and mean particle radius increase, since there is a longer distance over which the particles grow. The increased solid fraction results in more heat release as latent heat to the flow, generating an higher exit velocity.

4. **Do plume characteristics provide constrains on the crevasse geometry, ocean properties or other processes?** To match the observed plume characteristics by Cassini, the channel length ranges from $150 - 1000\ m$, to generate the wide range of particle sizes ($0.1 - 75\ \mu m$) and to be in agreement with the estimated shell thickness. The channel requires an expansion ratio close to $D_{throat}/D_{exit} = 4$, to generate the observed exit temperature $\leq 210\ K$ with velocities up to $950\ m/s$ and a solid fraction ranging from $0.07 - 0.2$. The minimum width of the channel needs to be in the order of meters to withhold the channel from freezing up within days and a liquid reservoir at a temperature near triple point is most probable to agree with the observed exit temperature and velocity.

3.2. Recommendations

This thesis has been conducted with the intention of submitting a scientific paper and since the studies on the plumes of Enceladus are far from completed, recommendations for future steps are provided.

1. Introduce a mixture of volatile compounds to the flow, in order to better represent the actual composition of the flow. The salinity can have an effect on the flow temperature, solid fraction, particle sizes and other plume characteristics.

2. Extend the model to compute the flow above the surface of Enceladus. The measurements of Cassini where made kilometres above the surface, by computing the flow at the same altitude as where the measurements were taken improves the comparability.

3. Compute the flow in three dimensions using a Monte Carlo simulation instead of quasi one-dimensional. Individual particles can be tracked and the non-steady aspect of the flow can be better studied.

4. Finally, a recommendation for future missions that will perform in-situ measurements of the plume. To better constrain numerical models it would be extremely helpful to have measurements of the flow parameters (V, T, p, ρ) near the vent, but also below the surface. Also, measurements of the reservoir conditions would reduce the ambiguity of the results and allow for more reliable studies.

4

Appendix B

4.1. Nucleation pulse experiment

In this study the nucleation rate γ_{nuc} is an important parameter of the flow, since it instigates the phase change. For that reason it is important to understand how the phenomenon of nucleation works. For that purpose we summarise the experiment conducted by Viisanen et al. [34] in this section.
Homogeneous nucleation of water droplets in the vapor phase is investigated in the study of Viisanen et al. [34]. A pulse technique was used to determine the nucleation rates J versus supersaturation S in the range of 10^5 to $10^9\ cm^{-3}s^{-1}$. The nucleation rates are a function of supersaturation and of temperature T, in this study the temperature range is set to $217.1\ K$ to $259\ K$.
The measurements were performed with an expansion chamber with two valves that connect the chamber to two additional volumes. This is done to precisely regulate the volume, pressure and temperature. The carrier gas and water vapor are mixed prior to the start of the experiment at the desired pressure. With the filling procedure it is exactly known what the vapor pressure p_v is, i.e., it is

$$p_v = \omega_v p_0 \tag{4.1}$$

where ω_v is the vapor fraction in the mixture and p_0 is the total pressure. By varying the total pressure p_0, the vapor pressure p_v is regulated, which in turn makes it possible to conduct the experiment at a desired constant temperature [34]. The cross section of the experimental setup is displayed in The pressures are set such that the expansion always leads to the same, desired, temperature. Which is calculated from Poission's law,

$$T = T_0\,(p/p_0)^{(\kappa-1)/\kappa} \tag{4.2}$$

in this equation κ is determined by the Richarz formula [30]:

$$\kappa = 1 + \left\{\omega_v/\,(\kappa_v - 1) + (1-\omega_v)\,/\,(\kappa_g - 1)\right\}^{-1} \tag{4.3}$$

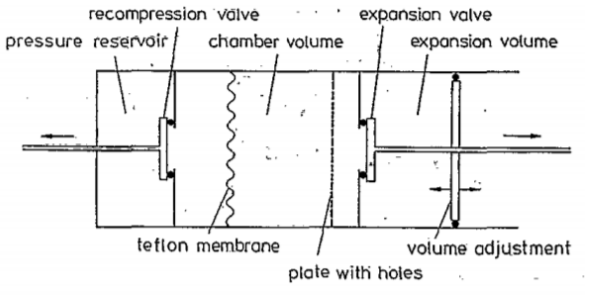

h

Figure 4.1: Schematic overview of the cross section of the expansion pulse chamber. The chamber volume is connected to an adjustable additional volume by the expansion valve. The plate with narrow holes damps the gas flow. At the end of the nucleation phase, the recompression valve is opened to recompress the flow. All pressures in the chamber, pressure reservoir and expansion volume are separately selectable and regulate the pressure pulse. The inner diameter of the chamber is 3 cm and the black circles are O rings, which seal the various parts. The figure is from the study of Viisanen et al. [34].

In this equation, κ_g and κ_v are the ratio of specific heats for the carrier gas and the vapor, respectively. The expansion is performed within a few milliseconds, in this process the expansion and recompression valves are released in a well-defined sequence [34]. The experiment starts with a pressure pulse. First there is an expanded, supersaturated state, in which nucleation occurs, which is maintained for Δt_{expt}. Second, the flow is recompressed, which causes the nucleation process to quench. Third, well after the recompression, scattered light intensity is measured at $\theta = 15^o$. This process is illustrated in Figure 4.2. From this scattered light, the number of nucleated particles is determined, which relates the nucleation rate γ_{nuc} to temperature and pressure.

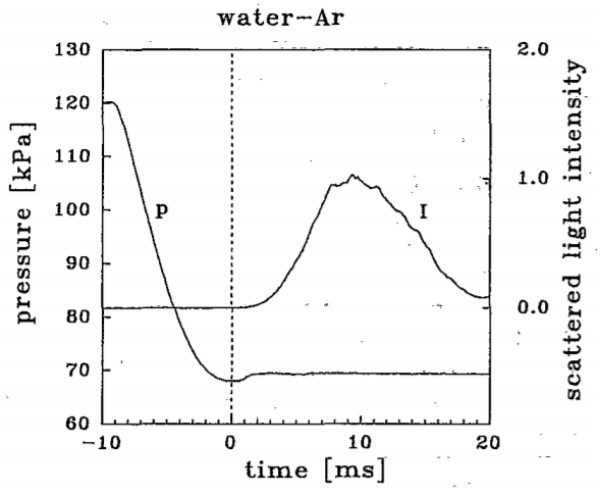

Figure 4.2: Pressure pulse and scattered light intensity versus time of the nucleation process of water vapor in the carrier gas Ar, from the study of Viisanen et al. [34].

4.2. Wall mass flux

Validation of the wall mass flux, consisting of accretion and sublimation, is performed by comparison with Eq. (4.18)(Nakajima and Ingersoll [20]). For the sake of comparison we rewrite the equations for accretion and sublimation into one equations for mass flow into the walls per unit area E $[kg/sm^2]$. The mass flow into the walls due to accretion is written as:

$$\dot{m}_a = \sum_0^n x(1-x)^{n-1} \cdot \rho A V \tag{4.4}$$

By introducing all the parameters for accretion, using the ideal gas law $p = \rho R T$, where $R = 461.5$, we can write n as:

$$\begin{aligned} n &= \frac{t}{\Delta t} = \frac{V_{th}}{V} \cdot \frac{p}{T} \cdot \frac{\sigma}{k} \Delta x = \frac{V_{th}}{V} \cdot \rho \cdot \frac{\sigma R}{k} \Delta x \\ &\approx 3 \cdot 10^6 \frac{V_{th}}{V} \cdot \rho \Delta x \end{aligned} \tag{4.5}$$

and x as:

$$\begin{aligned} x &= p_\lambda \frac{\lambda c_{stick}}{r} = p_\lambda \frac{k T c_{stick}}{r} = \frac{T c_{stick}}{r} \cdot \frac{p_\lambda k}{\sigma} \\ &\approx 3 \cdot 10^{-5} \frac{T c_{stick}}{r} \end{aligned} \tag{4.6}$$

The mass flow into the walls per unit area due to accretion E_a, is computed with n from Eq. (4.5) and Eq. (4.6), which is then divided by the surface area of the walls S.

Eq. (4.14) is generated by knowing that x is the fraction of mass flow that is lost by accretion into the walls after one collision sequence. The time for this is Δt. Before any collsions we have:

$$\dot{m}_{flow} = \rho AV \tag{4.7}$$

During the first collision sequence we lose $\dot{m}_{walls,dt1}$:

$$\dot{m}_{a,dt1} = x \cdot \rho AV \tag{4.8}$$

What remains in the flow is:

$$\dot{m}_{flow,dt2} = (1-x) \cdot \rho AV \tag{4.9}$$

In the second collision sequence we lose x multiplied with the mass flow that is left in the cell:

$$\dot{m}_{a,dt2} = x(1-x) \cdot \rho AV \tag{4.10}$$

What remains is then:

$$\dot{m}_{flow,dt3} = (1-x) \cdot \rho AV - x(1-x) \cdot \rho AV = (1-x)^2 \cdot \rho AV \tag{4.11}$$

In the third sequence we thus lose:

$$\dot{m}_{a,dt3} = x(1-x)^2 \cdot \rho AV \tag{4.12}$$

We can thus write that the accretion mass flow into the walls is:

$$\dot{m}_{a,dtn} = x(1-x)^{n-1} \cdot \rho AV \tag{4.13}$$

By taking the sum of this, we find the total mass that accretes onto the walls per cell:

$$\dot{m}_a = \sum_{0}^{n} x(1-x)^{n-1} \cdot \rho AV \tag{4.14}$$

$$E_a = \sum_{i=1}^{n} \left(3 \cdot 10^{-5} \frac{Tc_{stick}}{r}\right) \left[1 - \left(3 \cdot 10^{-5} \frac{Tc_{stick}}{r}\right)\right]^{n-1} \cdot \dot{m}_{flow}/S \tag{4.15}$$

For the mass flow per unit area of sublimation we find the following function by filling in all the known variables and dividing by the surface area of the walls S:

$$E_s = ve^{\left(-\frac{E}{T}\right)} \frac{nSm_{H_2O}}{N_A} \approx 8 \cdot 10^5 e^{\left(-\frac{5600}{T}\right)} \tag{4.16}$$

We write the total mass flow per unit area into the walls as:

$$E = E_s - E_a \tag{4.17}$$

We compute E for the baseline channel using the multi-phase model with wall interactions, where we compare the outcome of Eq. (4.17) and Eq. (4.18).

$$E = 2\left(\frac{p}{\sqrt{2\pi RT/M}} - \frac{p_w}{\sqrt{2\pi RT_w/M}}\right) \tag{4.18}$$

Where E is the wall mass flux per unit area [$kg/m^2 s$], R is the gas constant, M is the molar mass T_w is the temperature of the wall [K] and p_w is the saturation vapor pressure at the temperature of the wall, written as:

$$p_w = 3.63 \cdot 10^{12} e^{(-6147/T_w)} \tag{4.19}$$

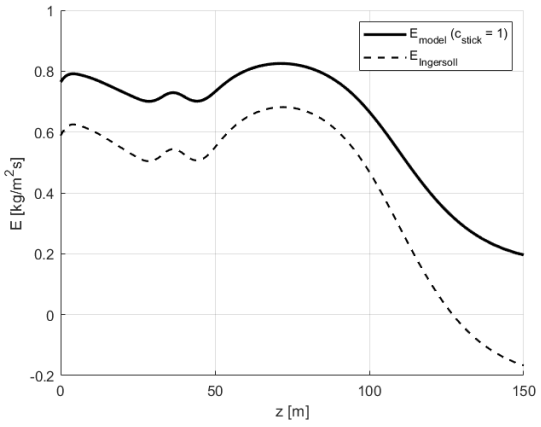

Figure 4.3: Comparison of wall mass flux per unit area E. The behaviour of E is similar in both cases, only the magnitude differs $\sim 30\%$. The outcome serves as a method of validation for the new accretion model of this paper.

The results of this comparison are given in Fig. 4.3. The results are very similar, although this is only true for a sticking coefficient of 1. The difference between the results is therefore partially explained by the sticking coefficient, that in this paper is always smaller than 1. The method in both cases is also different, this paper uses a more physical approach, considering individual collisions with the wall. Whereas, in the validation data an empirical relation is used that neglects the redistribution of the flow after collisions and the fact that not the whole flow 'sees' the walls. I.e., the mean free path λ multiplied with the number of collisions in one cell, is the maximum distance a particle can travel within that cell. If this distance is smaller than the distance to the wall, this particle will never hit the wall in that cell. After each collision the flow is assumed to redistribute, the layer of particles near the wall will be in equilibrium with the wall (Ingersoll and Pankine [13]). But, the particles that do not interact with the wall, will not necessarily be in equilibrium with the walls.

4.3. MacCormack solver

The numerical model of this study is set up using the MacCormack theory, discussed in Anderson and Wendt [2]. The MacCormack method simulates a steady, quasi-1D nozzle flow, according to the isentropic relations, with a time-marching, finite-difference solution. The method uses a predictor-corrector scheme based on forward and rearward differences. In every iteration the flow field is updated according to these differences. To this model we add shock-capturing features to cope with the non-continuous flow field in the case of a normal shock wave. This section explains how the program is generated and the verification with the data given by Anderson and Wendt [2].

4.3.1. Governing equations

The governing equations are similar as in the paper, but without the additional terms for the wall interactions and the phase change. They also contain a time dependent term, which dictates the change in solution vectors per iteration. The conservation equations for mass, momentum and energy are stated in Eq. (4.20), Eq. (4.21) and Eq. (4.22).

$$\frac{\partial(\rho A)}{\partial t} + \frac{\partial(\rho A V)}{\partial x} = 0 \tag{4.20}$$

$$\frac{\partial(\rho V A)}{\partial t} + \frac{\partial\left(\rho V^2 A\right)}{\partial x} = -A\frac{\partial p}{\partial x} \tag{4.21}$$

$$\frac{\partial\left[\rho\left(e + V^2/2\right)A\right]}{\partial t} + \frac{\partial\left[\rho\left(e + V^2/2\right)VA\right]}{\partial x} = -\frac{\partial(pAV)}{\partial x} \tag{4.22}$$

In the case of the plumes, it is reasonable to assume that the plume material behaves like a perfect gas, neglecting intermolecular forces. This results in Equation 4.23, the equation of state.

$$p = \rho R T \tag{4.23}$$

Non-dimensional form
The equations are made non-dimensional for the sake of data interpretation. With the following relations:

- $T' = \frac{T}{T_0}$
- $\rho' = \frac{\rho}{\rho_0}$
- $x' = \frac{x}{L}$
- $a_0 = \sqrt{\gamma R T_0}$
- $V' = \frac{V}{a_0}$
- $t' = \frac{t}{L/a_0}$
- $A' = \frac{A}{A*}$
- $e_0 = C_v T_0 = \frac{RT_0}{\gamma - 1}$
- $e' = \frac{e}{e_0}$

To simplify, the following relations are used: $\frac{R}{C_v} = \frac{R}{R/(\gamma-1)} = \gamma - 1$, $e = C_v T$. The non-dimensional form of the continuity and momentum equation are given in Eq. (4.26) and Eq. (4.27), respectively. This is done with the aid of the following equations:

$$\frac{\partial (pA)}{\partial x} = p\frac{\partial A}{\partial x} + A\frac{\partial p}{\partial x} \tag{4.24}$$

$$\frac{p_0}{\rho_0 a_0^2} = \frac{\rho_0 R T_0}{\rho_o a_0^2} = \frac{\rho_0 R T_0}{\rho_0 \gamma R T_0} = \frac{1}{\gamma} \tag{4.25}$$

Resulting in:

$$\frac{\partial (\rho' A')}{\partial t'} + \frac{\partial (\rho' A' V')}{\partial x'} = 0 \tag{4.26}$$

$$\frac{\partial (\rho' A' V')}{\partial t'} + \frac{\partial \left[\rho' A' V'^2 + (1/\gamma) p' A'\right]}{\partial x'} = \frac{1}{\gamma} p' \frac{\partial A'}{\partial x'} \tag{4.27}$$

The non-dimensional form of the energy equation is determined by first combing the x derivatives of Eq. (4.22), which gives:

$$\frac{\partial \left[\rho \left(e + V^2/2\right) A\right]}{\partial t} + \frac{\partial \left[\rho \left(e + V^2/2\right) AV + pAV\right]}{\partial x} = 0 \tag{4.28}$$

Non-dimensionalized with the previously mentioned relations:

$$\frac{\partial \left\{ \frac{\rho}{\rho_0} \left[\frac{e}{e_0}(e_0) + \frac{V^2}{2a_0^2}(a_0^2) \right] \frac{A}{A^*} \right\}}{\partial \left(\frac{t}{L/a_0} \right)} \left(\frac{\rho_0 A^* a_0}{L} \right) + \frac{\partial \left\{ \frac{\rho}{\rho_0} \left[\frac{e}{e_0}(e_0) + \frac{V^2}{2a_0^2}(a_0^2) \right] \frac{V}{a_0} \frac{A}{A^*}(\rho_0 a_0 A^*) + \left(\frac{p}{p_0} \frac{A}{A^*} \frac{V}{a_0} \right)(p_0 A^* a_0) \right\}}{\partial \left(\frac{x}{L} \right) L} = 0 \tag{4.29}$$

With $e_0 = RT_0/(\gamma - 1)$ and $a_0 = \sqrt{\gamma RT}$:

$$\frac{\partial \left[\rho' \left(\frac{e'}{\gamma - 1} + \frac{\gamma}{2} V'^2\right) A'\right]}{\partial t'} \left(\frac{\rho_0 A^* a_0 R T_0}{L} \right) + \frac{\partial \left[\rho' \left(\frac{e'}{\gamma - 1} + \frac{\gamma}{2} V'^2\right) V' A' \left(\frac{\rho_0 a_0 A^* R T_0}{L} \right) + (p' A' V') \left(\frac{p_0 A^* a_0}{L} \right)\right]}{\partial x'} = 0 \tag{4.30}$$

Divide the equation by $\rho_0 A^* a_0 R T_0 / L$:

$$\frac{\partial \left[\rho' \left(\frac{e'}{\gamma - 1} + \frac{\gamma}{2} V'^2\right) A'\right]}{\partial t'} + \frac{\partial \left[\rho' \left(\frac{e'}{\gamma - 1} + \frac{\gamma}{2} V'^2\right) V' A' + p' A' V' \left(\frac{p_0}{\rho_0 R T_0} \right)\right]}{\partial x'} = 0 \tag{4.31}$$

4.3.2. Conservative vs. Non-Conservative

In the MacCormack method there are two methods, both derived from the same three fundamental physical statements. Namely the governing equations in the conservative and the non-conservative form. The conservation form can be rewritten in to the non-conservation form and vice-versa by means of the Anderson and Wendt [2]. The main difference between the two approaches is the ability of shock capturing. This and other differences will be discussed in this section.
Also the flow case that is described in the book of Anderson and Wendt [2] is performed in both the conservation and non-conservation form. This case used the nozzle displayed in Figure 4.4. With this nozzle and no exit pressure set, the flow is completely isentropic without the present of a shock. The

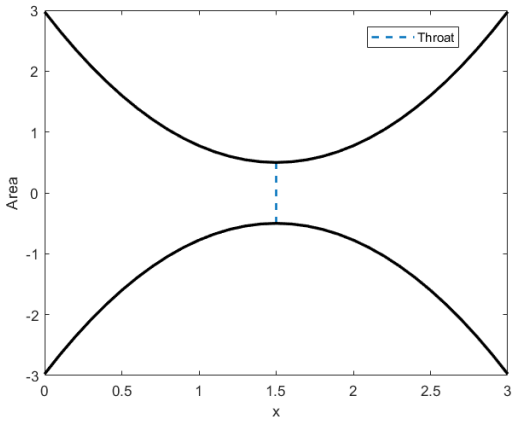

Figure 4.4: Nozzle geometry for the verification of the MacCormack method.

program is set to run for a number of iterations and the goal is to converge to an accurate steady-state solution. This is for both cases accomplished, each form generates the same solution. This is as it should be, since both use the same equations Anderson and Wendt [2], the final results are shown in Figure 4.5. These results are identical to those of Anderson and Wendt [2], which verifies the solver used in this study. The conditions in the throat of the nozzle for all iterations is displayed in Figure 4.6.

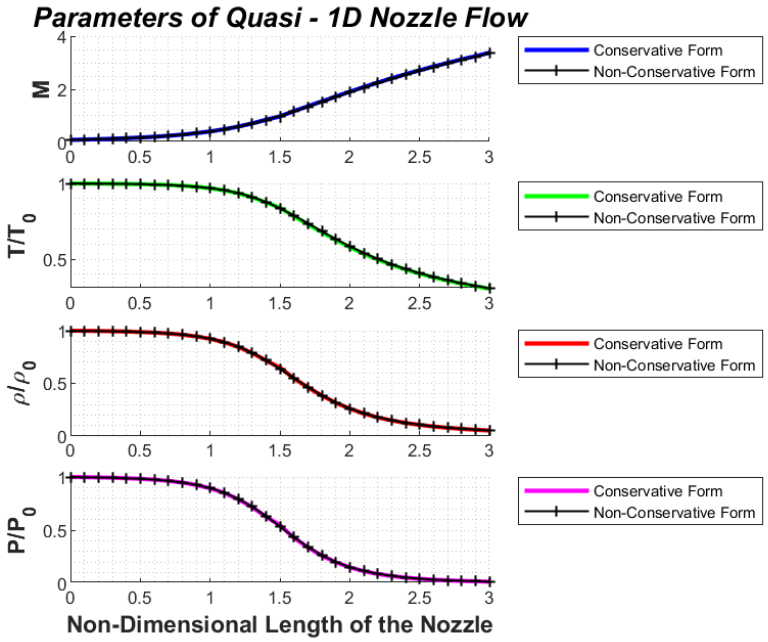

Figure 4.5: Flow parameters for the conservation and non-conservation form.

Both forms converge to a steady-state solution after approximately 700 iterations. After 700 iterations, the state variables do not change significantly anymore. There is a slight difference in the results for conservation and non-conservation form ($\approx 1\%$). The reasons for these differences are discussed in subsection 4.3.3 and subsection 4.3.4.

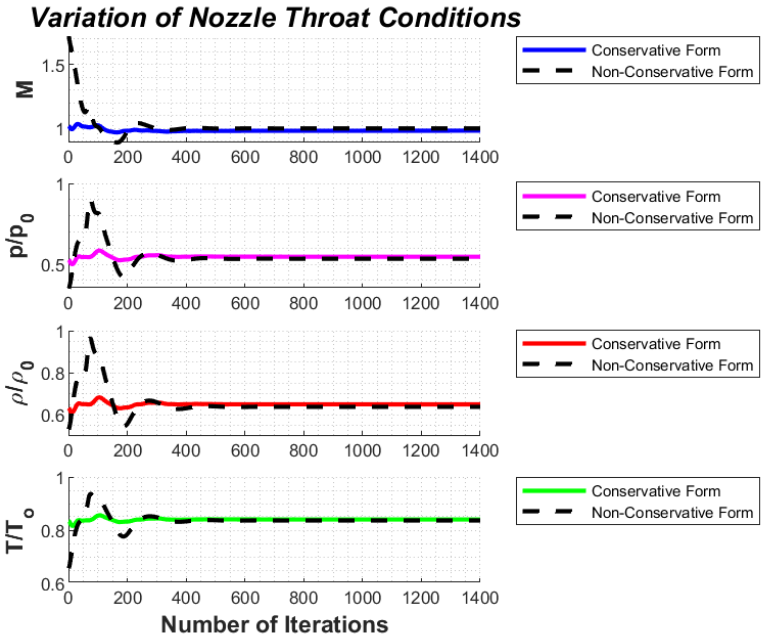

Figure 4.6: Nozzle throat conditions for conservation and non-conservation form.

4.3.3. Conservation Form

In the conservation form, all equations have the divergence term on the left-hand side. These terms involve the *flux* of physical quantities. These are mass flux, x-component of momentum flux and internal and total energy flux, respectively.

$$\rho \mathbf{V} \tag{4.32}$$

$$\rho u \mathbf{V} \tag{4.33}$$

$$\rho e \mathbf{V} \tag{4.34}$$

$$\rho(e + \frac{V^2}{2})\mathbf{V} \tag{4.35}$$

Since the conservation form is directly obtained from the control volume which was fixed in space, the *fluxes* of mass, momentum and energy in and out of the volume are of importance. In the non-conservative form, the equations are obtained from the control volume moving with the fluid, where the primitive variables are of importance.
To deal with shocks in flows there are two distinct options, the *shock-capturing* and *shock-fitting* method. The shock capturing method treats shocks as nature would have it, but the shock is smeared out over several grid points. Therefore, the shock location and thickness is not exactly known. The shock-fitting method treats the shock as a discontinuity and deals with the shock separately, but one has to know beforehand where the shock is located Anderson and Wendt [2]. Each method has it advantages and disadvantages, a combination of the two is also a possibility.
For the *shock-capturing* method the *conservation form* should be used, this generates stable and smooth results. The non-conservation form is not fit for the shock-capturing method, oscillations occur near the shock, the shock may appear in the wrong location and the solution might become unstable. For the shock-fitting method, either form can be used Anderson and Wendt [2].
The need for the conservation form can be seen in Figure 4.7. There are clear discontinuities for ρ and

p over the normal shock wave. For the non-conservation form the calculation of ρ and p would generate large errors, related to the time-derivatives. On the other hand, when the conservation form is used, the mass-flux ρu is constant across the shock wave. This term ρu is used as dependent variable in the conservation form, therefore there is no discontinuity in this form. The same goes for the momentum equation, where the dependent variable $p + \rho u^2$ also remains constant. Changes in flux variables are zero or small over shock, which makes the conservation form very applicable for the shock-capturing method Anderson and Wendt [2].

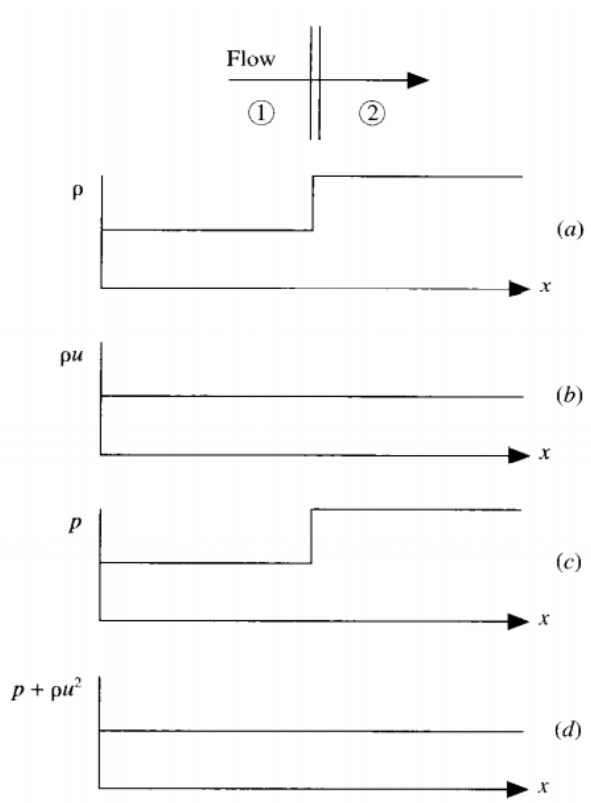

Figure 4.7: Flow properties over a normal shock wave, (Anderson and Wendt [2]).

The mass flow is better estimated by the conservation form, since it is one of the dependent variables. The mass flow can be directly obtained from the solution vector and is therefore more accurate Anderson and Wendt [2]. This is illustrated in Figure 4.8, where the mass flow of the conservation form is closer to the analytical solution.

4.3.4. Non-Conservation Form

Non-Conservative uses primitive variables such as ρ, p, T and e. In a shock wave there are discontinuities present, these are shown in Figure 4.7. There it is illustrated that across a normal shock wave:

$$\rho_1 \neq \rho_2 \tag{4.36}$$

$$p_1 \neq p_2 \tag{4.37}$$

Where subscript 1 is before the shock and 2 is for after the shock. The non-conservative form of the governing equations can not cope with the discontinuities in the shock wave, since this imposes a large increase or decrease over a small time step dt. Oscillations start to occur which generates invalid solutions. The accuracy of the primitive variables for a flow without a shock wave is higher than for the conservation form, this is since the primitive variables can be directly obtained from the equations Anderson and Wendt [2].

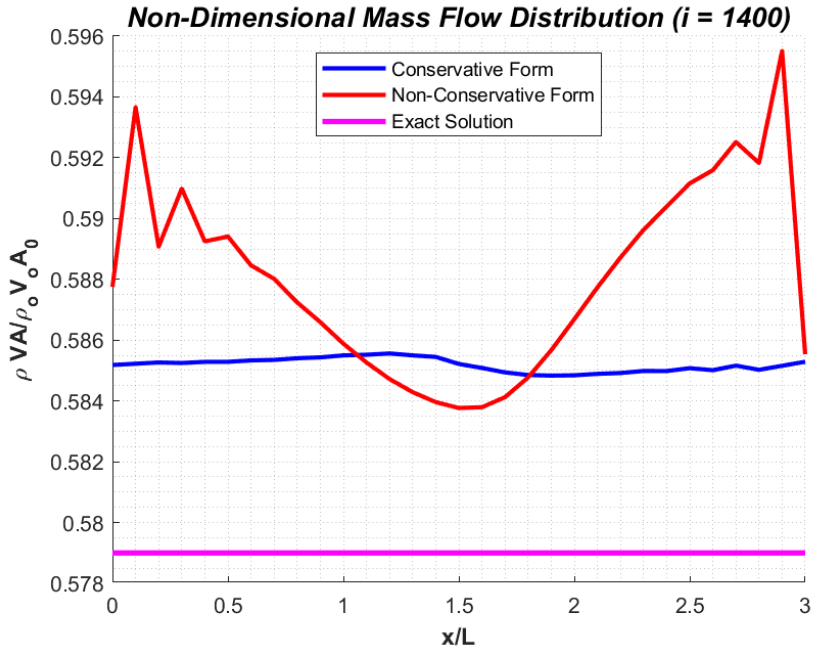

Figure 4.8: Mass flow distribution along the nozzle; conservative, non-conservative and analytical solution.

4.3.5. Artificial Viscosity

In this model the MacCormack approach is used to numerically solve the governing flow equations. Numerical solutions for the Euler or Navier-Stokes equations are obtained with accuracy's determined by round-off and truncation errors. The specific differential equations are numerically solved but come with an error. The MacCormack method is the most popular explicit finite-difference method for solving fluid flows. The method is based on Taylor's series expansion in time. In Equation 4.38, the density at grid i is considered. This is a truncated Taylor's series that looks first-order accurate. $(\partial\rho/\partial t)_{ave}$ is an *average* time derivative between t and $t + \Delta t$. The derivative in Equation 4.38 is evaluated in such a manner that the calculation of $\rho_i^{t+\Delta t}$ becomes second-order accurate $O(\Delta t^2)$ Anderson and Wendt [2]. This means that the error is in the order of Δt^2. This average time derivative is evaluated from a predictor-corrector philosophy.

$$\rho_i^{t+\Delta t} = \rho_i^t + \left(\frac{\partial \rho}{\partial t}\right)_{ave} \Delta t \tag{4.38}$$

Since the numerical solutions contain errors, numerical dissipation is added. In the modified equation of the partial differential equations for fluid dynamics, terms like $\partial^2 u/\partial x^2$ are present. Such terms are also present in the complete Navier-Stokes equations, in conservation form, multiplied by the viscosity coefficient, μ (Anderson and Wendt [2]). These terms represent the dissipative aspect of viscosity in the flow. However, in this model this term has a pure numerical origin, numerical discretization embodied in the difference equation Anderson and Wendt [2]. Therefore $\partial^2 u/\partial x^2$, is added as numerical dissipation. The terms numerical dissipation and artificial viscosity are used interchangeably. The case that a discontinuous wave starts at time zero is sketched in Figure 4.9. The effect of artificial viscosity is to spread out the wave similar to how physical viscosity would spread out the wave. Intentionally adding artificial viscosity makes the solution more inaccurate. However, it does contribute to converge to a stable solution. A stable solution that in many cases otherwise is not able to obtain. Such cases are flow problems with very strong gradients, such as shock waves. For this reason, artificial viscosity is added, since there is a possibility for a shock wave in the plumes of Enceladus. The shock is captured with this *shock-capturing approach*.
Equation 4.39 represents the governing flow equation for unsteady, 1D flow.

$$\frac{\partial U}{\partial t} = -\frac{\partial F}{\partial x} + J \tag{4.39}$$

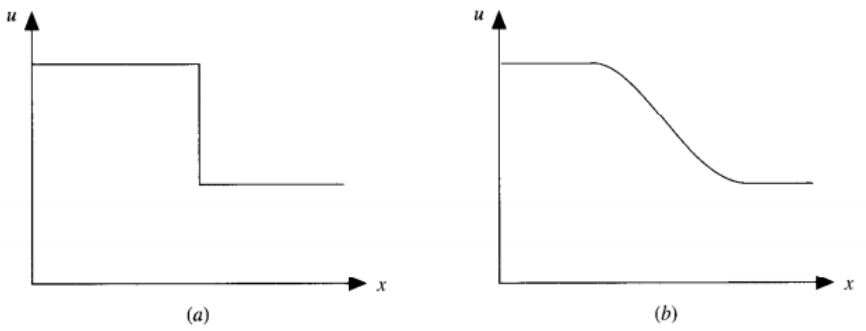

Figure 4.9: Effect of artificial viscosity (numerical dissipation). (a) Initial wave at first iteration. (b) Shape of the wave after several iterations, as affected by artificial viscosity. From the book of Anderson and Wendt [2].

U is the solution vector, $U = [\rho, \rho u, \rho v, \rho\left(e + V^2/2\right)]$, F is the flux vector and J is the source vector. Artificial viscosity can be added in each time step by:

$$S_i^{t'} = \frac{C_x \left|(p')_{i+1}^{t'} - 2\,(p')_i^{t'} + (p')_{i-1}^{t'}\right|}{(p')_{i+1}^{'} + 2\,(p')_i^{t'} + (p')_{i-1}^{t'}} \left(U_{i+1}^{t'} - 2U_i^{t'} + U_{i-1}^{t'}\right) \tag{4.40}$$

Equation 4.40 is a fourth-order numerical dissipation expression Anderson and Wendt [2]. It 'tweaks' the calculations like a fourth-order term in the truncation error would, with equivalent magnitude. In the numerators the fourth-order nature is seen, the products of two second-order central difference expressions for second derivatives. The C-expressions are arbitrarily set parameters that usually are in the range of 0.01 to 0.3. $S_{i,j}^t$ on the predictor step is evaluated based on the known quantities at time t. The corrector step is determined with the same equation, but then with the predicted values for U and p. These are written with a bar, in the form of $\bar{S}_{i,j}^t$, shown in Equation 4.41.

$$\bar{S}_i' + \Delta t' = \frac{C_x \left|(\bar{p}')_{i+1}^{t'+\Delta t'} - 2\,(\bar{p}')_i^{t'+\Delta t'} + (\bar{p}')_{i-1}^{t'+\Delta t'}\right|}{(\bar{p}')_{i+1}^{t'} + 2\,(\bar{p}')_i^{t'} + (\bar{p}')_{i-1}^{t'}} \times \left[(\bar{U})_{i+1}^{t'+\Delta t'} - 2(\bar{U})_i^{t'+\Delta t'} + (\bar{U})_{i-1}^{t'+\Delta t'}\right] \tag{4.41}$$

The values of $S_{i,j}^t$ and $\bar{S}_{i,j}^{t+\Delta t}$ are added at every grid point in the calculation. This is done in the following fashion, with an example of the U_n calculation (for $n = 1, 2, 3$).

$$\bar{U}_{n\,i,j}^{\,t+\Delta t} = U_{n\,i,j}^{\,t} + \left(\frac{\partial U_n}{\partial t}\right)_{i,j}^{t} \Delta t + S_{l,j}^t \tag{4.42}$$

On the corrector step, the corrected value for U_n at time $t + \Delta t$, with the artificial viscosity, becomes:

$$U_{n\,i,j}^{\,t+\Delta t} = U_{n\,i,j}^{\,l} + \left(\frac{\partial U_n}{\partial t}\right)_{\text{av}} \Delta t + \bar{S}_{i,j}^{t+\Delta t} \tag{4.43}$$

The effect of the addition of artificial viscosity is illustrated in Figure 4.10. As illustrated, it smooths out the solution and minimalizes oscillations, resulting in a stable solution. It has the greatest effect where the pressure gradient is largest. One wants to minimize the amount of artificial viscosity to maintain the accuracy of the program. The artificial viscosity addition to the numerical solution function as a source term. The values for S_i^t and $S_i^{t+\Delta t}$ are largest where the change in pressure is largest, according to Equation 4.40 and Equation 4.41. The most artificial viscosity is added in the regions where the pressure gradients are changing rapidly. It is added to the solution vectors, of which $U_2 = \rho AV$. The conservation of mass is slightly violated and in the region of the shock the mass flow seems to increase. This is illustrated in Figure 4.11. This is however required, since otherwise the oscillations in the solution would generate unacceptable results. The results obtained with the addition of artificial viscosity are still acceptable Anderson and Wendt [2].

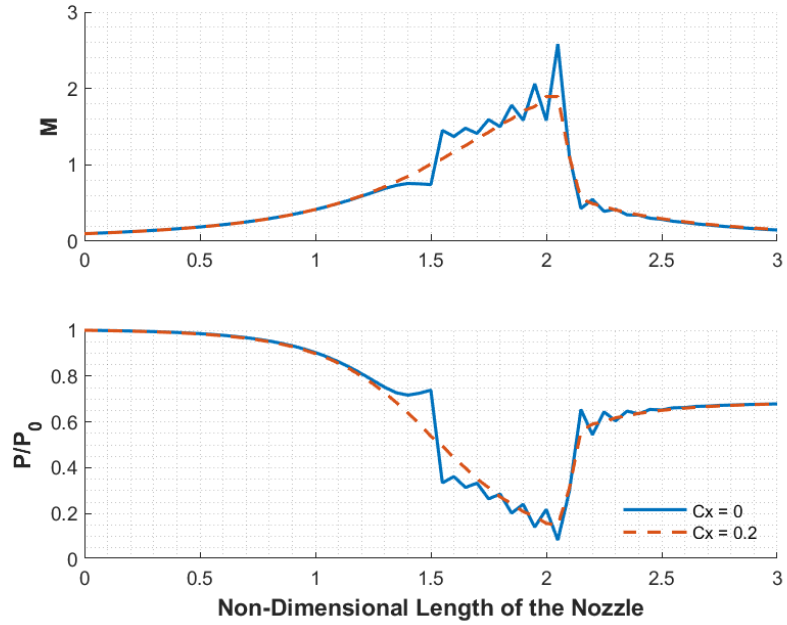

Figure 4.10: The effect of artificial viscosity.

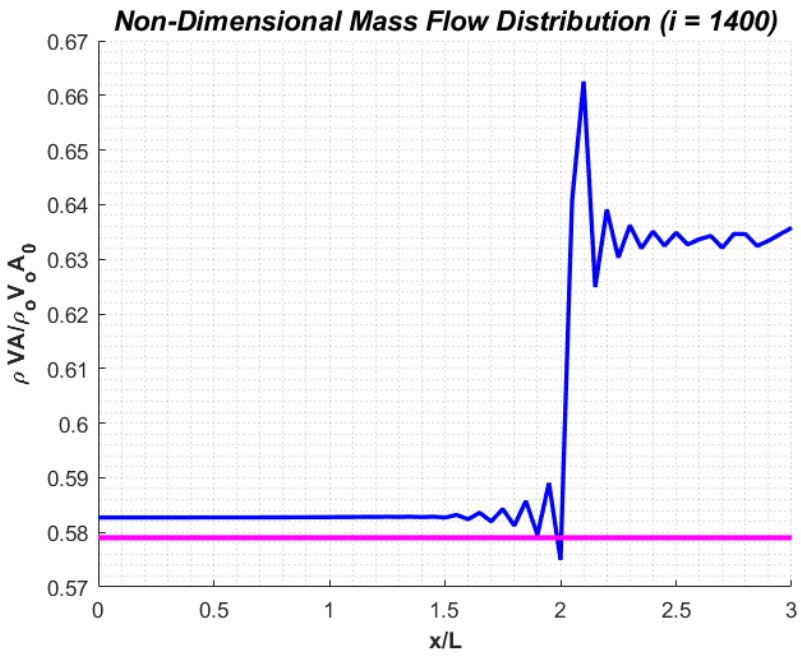

Figure 4.11: Mass flow along the nozzle.

4.4. Governing equations

The magnitude of friction and convection in the momentum and energy equation has been examined. In the momentum equation the viscous effect of friction is left out, since the effect is very small compared to the loss of momentum due to accretion and the total momentum of the flow (Fig. 4.12). The effect of friction is left out, since its contribution to the momentum equation is significantly smaller than that of accretion and sublimation ($< 20\%$). This allows for better interpretation of the effect of accretion and sublimation on the plume characteristics.
In the energy equation the convection of heat through the wall is left out of the equation, since the

effect is insignificant compared to the loss of energy due to accretion and the total energy of the flow (Fig. 4.12). This allows for better interpretation of the effect of accretion and sublimation on the plume characteristics.

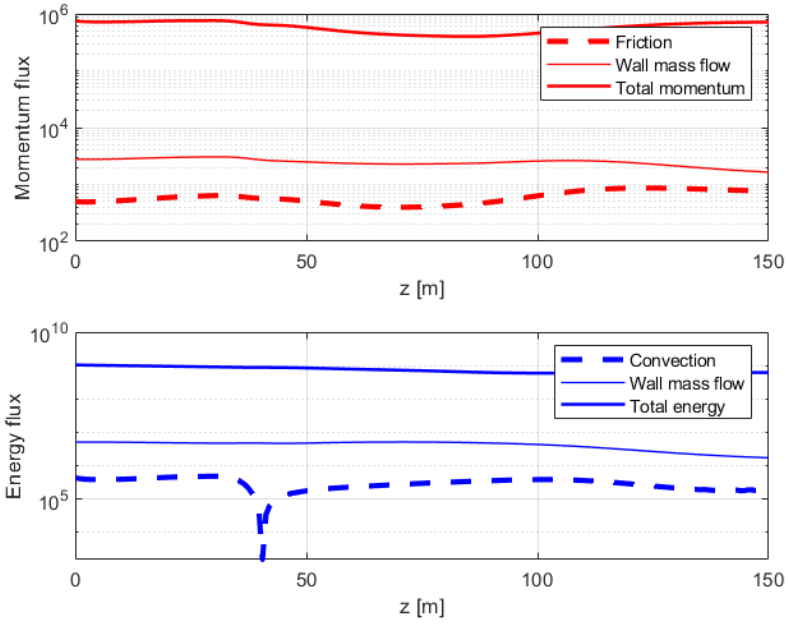

Figure 4.12: In the top panel the effect of friction and the mass flow into the walls is compared to the total momentum of the flow. In the bottom panel the effects of convection and the mass flow into the walls is compared to the total energy flow. In both cases the effect of mass flow into the walls is significantly larger.

4.4.1. Governing equations derivations

The governing equations are derived from the integral form of the continuity, momentum and energy equation, adapted to account for a phase change and wall interactions. In this section, these equations contain a time-dependent term, which is used to solve the governing equations in a time-marching way.

Continuity Equation

The energy equation is given by Equation 4.44, which contains a term that accounts for the change is mass flux due to accretion/sublimation on/from the walls.

$$\frac{\partial}{\partial t}\iiint \rho d\mathcal{V} + \iint_S \rho \mathbf{V}\cdot\mathbf{dS} = \iint_S E\mathbf{dS} \tag{4.44}$$

This is integrated, divided by dx and then the limit when dx approaches zero is taken, where c is the circumference of the channel:

$$\frac{\partial(\rho A)}{\partial t} + \frac{\partial(\rho A V)}{\partial x} = -\frac{E c dx}{dx} \tag{4.45}$$

Momentum Equation

We take the integral form of the momentum equation for inviscid flow from Anderson. To this equation terms are added that account for the loss of momentum due to friction and the momentum change due to condensation/evaporation to/from the walls.

$$\frac{\partial}{\partial t}\iiint_{\mathcal{V}} (\rho u) d\mathcal{V} + \iint_S (\rho u \mathbf{V})\cdot\mathbf{dS} = -\iint_S (pdS)_x + \iint_S \bar{\bar{\tau}}\mathrm{d}\mathbf{S} + \iint_S EVd\mathbf{S} \tag{4.46}$$

By integration, dividing by dx, and taking the limit as dx goes to zero, Equation 4.46 becomes:

$$\frac{\partial(\rho V A)}{\partial t} + \frac{\partial\left(\rho V^2 A\right)}{\partial x} = -A\frac{\partial p}{\partial x} - \frac{\tau c dx}{dx} + \frac{E c dx V}{dx} \tag{4.47}$$

The friction term: $\iint_{\partial V} \bar{\bar{\tau}} \mathrm{d}\bar{s}$. Where the tangential stress equals:

$$\tau = \frac{1}{2} f \rho v^2 \tag{4.48}$$

And is written as:

$$\oint_{\partial V} \bar{\bar{\tau}} \mathrm{d}\bar{s} = -\int_1^2 \tau c \, \mathrm{d}x \tag{4.49}$$

By taking stations 1 and 2 a distance dx apart the friction term becomes:

$$-\tau c dx \tag{4.50}$$

Energy Equation

The energy equation in integral form with terms accounting for the latent heat of vapor deposition, wall condensation/evaporation and a heat flux from or to the walls is written as:

$$\begin{aligned} \frac{\partial}{\partial t} \iiint_{\mathcal{V}} \rho \left(e + \frac{V^2}{2} \right) d\mathcal{V} + \iint_S \rho \left(e + \frac{V^2}{2} \right) \mathbf{V} \cdot \mathbf{dS} = -\iint_S (p\mathbf{V}) \cdot \mathbf{dS} - \iint_S E \left(e + \frac{V^2}{2} + \frac{p}{\rho} \right) d\mathbf{S} \\ + \iint f \rho V L_h d\mathbf{S} + \iint_S q(T - T_w) d\mathbf{S} \end{aligned} \tag{4.51}$$

Integration of $\iint E dS = E c dx = \dot{m}_{walls}$, from now on called $\dot{m}_w$. Then the equation is divided by dx and then taking the limit where dx goes to zero yields:

$$\frac{\partial \left[\rho \left(e + V^2/2 \right) A \right]}{\partial t} + \frac{\partial \left[\rho \left(e + V^2/2 \right) AV + pAV \right]}{\partial x} = \frac{E c dx \left(e + \frac{V^2}{2} + \frac{p}{\rho} \right)}{dx} \frac{\partial \left(\rho V f A \right)}{\partial x} L_h + q(T - T_w) S \tag{4.52}$$

Bibliography

[1] J. Hunter Waite A. Howett, Anne J. Verbiscer. Enceladus and the icy moons of saturn. page 478, 2006.

[2] John David Anderson and J Wendt. *Computational fluid dynamics*, volume 206. Springer, 1995.

[3] Michael T Bland, Kelsi N Singer, William B McKinnon, and Paul M Schenk. Enceladus' extreme heat flux as revealed by its relaxed craters. *Geophysical Research Letters*, 39(17), 2012.

[4] MH Burger, EC Sittler Jr, RE Johnson, HT Smith, OJ Tucker, and VI Shematovich. Understanding the escape of water from enceladus. *Journal of Geophysical Research: Space Physics*, 112(A6), 2007.

[5] Y Dong, TW Hill, BD Teolis, BA Magee, and JH Waite. The water vapor plumes of enceladus. *Journal of Geophysical Research: Space Physics*, 116(A10), 2011.

[6] Peter Gao, Pushkar Kopparla, Xi Zhang, and Andrew P Ingersoll. Aggregate particles in the plumes of enceladus. *Icarus*, 264:227–238, 2016.

[7] Melissa Guzman, Ralph Lorenz, Dana Hurley, William Farrell, John Spencer, Candice Hansen, Terry Hurford, Jassmine Ibea, Patrick Carlson, and Christopher P McKay. Collecting amino acids in the enceladus plume. *International Journal of Astrobiology*, 18(1):47–59, 2019.

[8] Candice J Hansen, L Esposito, AIF Stewart, J Colwell, A Hendrix, W Pryor, D Shemansky, and R West. Enceladus' water vapor plume. *Science*, 311(5766):1422–1425, 2006.

[9] CJ Hansen, LW Esposito, AIF Stewart, B Meinke, B Wallis, JE Colwell, AR Hendrix, K Larsen, W Pryor, and F Tian. Water vapour jets inside the plume of gas leaving enceladus. *Nature*, 456 (7221):477–479, 2008.

[10] CJ Hansen, Donald E Shemansky, Larry W Esposito, AIF Stewart, BR Lewis, JE Colwell, AR Hendrix, Robert A West, JH Waite Jr, B Teolis, et al. The composition and structure of the enceladus plume. *Geophysical Research Letters*, 38(11), 2011.

[11] MM Hedman, PD Nicholson, MR Showalter, RH Brown, BJ Buratti, and RN Clark. Spectral observations of the enceladus plume with cassini-vims. *The Astrophysical Journal*, 693(2):1749, 2009.

[12] Andrew P Ingersoll and Shawn P Ewald. Total particulate mass in enceladus plumes and mass of saturn's e ring inferred from cassini iss images. *Icarus*, 216(2):492–506, 2011.

[13] Andrew P Ingersoll and Alexey A Pankine. Subsurface heat transfer on enceladus: Conditions under which melting occurs. *Icarus*, 206(2):594–607, 2010.

[14] Andrew P Ingersoll, Shawn P Ewald, and Samantha K Trumbo. Time variability of the enceladus plumes: Orbital periods, decadal periods, and aperiodic change. *Icarus*, 344:113345, 2020.

[15] S Jurac and JD Richardson. A self-consistent model of plasma and neutrals at saturn: Neutral cloud morphology. *Journal of Geophysical Research: Space Physics*, 110(A9), 2005.

[16] Sascha Kempf, Uwe Beckmann, and Jürgen Schmidt. How the enceladus dust plume feeds saturn's e ring. *Icarus*, 206(2):446–457, 2010.

[17] Susan W Kieffer, Xinli Lu, Craig M Bethke, John R Spencer, Stephen Marshak, and Alexandra Navrotsky. A clathrate reservoir hypothesis for enceladus' south polar plume. *Science*, 314(5806): 1764–1766, 2006.

[18] Susan W Kieffer, Xinli Lu, Greg McFarquhar, and Kenneth H Wohletz. A redetermination of the ice/vapor ratio of enceladus' plumes: Implications for sublimation and the lack of a liquid water reservoir. *Icarus*, 203(1):238–241, 2009.

[19] Dennis L Matson, Julie C Castillo-Rogez, Ashley Gerard Davies, and Torrence V Johnson. Enceladus: A hypothesis for bringing both heat and chemicals to the surface. *Icarus*, 221(1):53–62, 2012.

[20] Miki Nakajima and Andrew P Ingersoll. Controlled boiling on enceladus. 1. model of the vapor-driven jets. *Icarus*, 272:309–318, 2016.

[21] Francis Nimmo, JR Spencer, RT Pappalardo, and ME Mullen. Shear heating as the origin of the plumes and heat flux on enceladus. *Nature*, 447(7142):289–291, 2007.

[22] Carolyn Porco, Daiana DiNino, and Francis Nimmo. How the geysers, tidal stresses, and thermal emission across the south polar terrain of enceladus are related. *The Astronomical Journal*, 148 (3):45, 2014.

[23] Carolyn C Porco, Paul Helfenstein, PC Thomas, AP Ingersoll, J Wisdom, Robert West, Gerhard Neukum, Tilmann Denk, Roland Wagner, Thomas Roatsch, et al. Cassini observes the active south pole of enceladus. *science*, 311(5766):1393–1401, 2006.

[24] Frank Postberg, Sascha Kempf, Jürgen Schmidt, N Brilliantov, Alexander Beinsen, Bernd Abel, Udo Buck, and Ralf Srama. Sodium salts in e-ring ice grains from an ocean below the surface of enceladus. *Nature*, 459(7250):1098–1101, 2009.

[25] Joachim Saur, Nico Schilling, Fritz M Neubauer, Darrell F Strobel, Sven Simon, Michele K Dougherty, Christopher T Russell, and Robert T Pappalardo. Evidence for temporal variability of enceladus' gas jets: Modeling of cassini observations. *Geophysical research letters*, 35(20), 2008.

[26] Jürgen Schmidt, Nikolai Brilliantov, Frank Spahn, and Sascha Kempf. Slow dust in enceladus' plume from condensation and wall collisions in tiger stripe fractures. *Nature*, 451(7179):685–688, 2008.

[27] HT Smith, RE Johnson, ME Perry, DG Mitchell, RL McNutt, and DT Young. Enceladus plume variability and the neutral gas densities in saturn's magnetosphere. *Journal of Geophysical Research: Space Physics*, 115(A10), 2010.

[28] JR Spencer, CJA Howett, A Verbiscer, TA Hurford, M Segura, and DC Spencer. Enceladus heat flow from high spatial resolution thermal emission observations. *EPSC Abstracts*, 8:840–1, 2013.

[29] Joseph N Spitale and Carolyn C Porco. Association of the jets of enceladus with the warmest regions on its south-polar fractures. *Nature*, 449(7163):695–697, 2007.

[30] R Strey and PE Wagner. Homogeneous nucleation of 1-pentanol in a two-piston expansion chamber for different carrier gases. *The Journal of Physical Chemistry*, 86(6):1013–1015, 1982.

[31] Valeriy Tenishev, Doğa Can Su Öztürk, Michael R Combi, Martin Rubin, Jack Hunter Waite, and Mark Perry. Effect of the tiger stripes on the water vapor distribution in enceladus' exosphere. *Journal of Geophysical Research: Planets*, 119(12):2658–2667, 2014.

[32] Ben D Teolis, Mark E Perry, Candice J Hansen, J Hunter Waite, Carolyn C Porco, John R Spencer, and Carly JA Howett. Enceladus plume structure and time variability: comparison of cassini observations. *Astrobiology*, 17(9):926–940, 2017.

[33] Feng Tian, AIF Stewart, Owen B Toon, Kristopher W Larsen, and Larry W Esposito. Monte carlo simulations of the water vapor plumes on enceladus. *Icarus*, 188(1):154–161, 2007.

[34] Y Viisanen, R Strey, and H Reiss. Homogeneous nucleation rates for water. *The Journal of chemical physics*, 99(6):4680–4692, 1993.

[35] Mikhail Y Zolotov. An oceanic composition on early and today's enceladus. *Geophysical Research Letters*, 34(23), 2007.